Electromagnetic Modelling of Barium Strontium Titanate and Magnesium Borate Bulk Composite Varactors

Tunability and Acoustic Resonances Suppression

Dem Fachbereich Elektrotechnik und Informationstechnik
der Technischen Universität Darmstadt
zur Erlangung des akademischen Grades eines
Doktor-Ingenieurs (Dr.-Ing.)
genehmigte

Dissertation

von

Master of Science

Prannoy Agrawal

geboren am 07.01.1991
in Neu-Delhi, Indien

Referent:	Prof. Dr.-Ing. Rolf Jakoby
Co-Referent:	Prof. Dr. rer. nat. Markus Meinert

Tag der Einreichung:	20. June 2023
Tag der mündlichen Prüfung:	2. November 2023

Darmstadt 2023

Agrawal, Prannoy: Electromagnetic Modelling of Barium Strontium Titanate and Magnesium Borate Bulk Composite Varactors - Tunability and Acoustic Resonances Suppression.
Darmstadt, Technische Universität Darmstadt
Jahr der Veröffentlichung der Dissertation auf TUprints: 2024
URN: urn:nbn:de:tuda-tuprints-269712
Tag der mündlichen Prüfung: 02.11.2023
Veröffentlicht unter CC BY 4.0 International
https://creativecommons.org/licenses/

Erklärungen laut Promotionsordnung

§ 8 Abs. 1 lit. c PromO

Ich versichere hiermit, dass die elektronische Version meiner Dissertation mit der schriftlichen Version übereinstimmt.

§ 8 Abs. 1 lit. d PromO

Ich versichere hiermit, dass zu einem vorherigen Zeitpunkt noch keine Promotion versucht wurde. In diesem Fall sind nähere Angaben über Zeitpunkt, Hochschule, Dissertationsthema und Ergebnis dieses Versuchs mitzuteilen.

§ 9 Abs. 1 PromO

Ich versichere hiermit, dass die vorliegende Dissertation selbstständig und nur unter Verwendung der angegebenen Quellen verfasst wurde.

§ 9 Abs. 2 PromO

Die Arbeit hat bisher noch nicht zu Prüfungszwecken gedient.

Darmstadt, 20. Juni 2023

Preface

From losing hope of doing a master's degree to reaching the end of a doctorate degree, life was full of ups and downs. Despite this, the learning curve keeps on improving. Being a research assistant at Institute for Microwave Technology and Photonics (IMP), this dissertation is written. It consists of findings obtained in close interdisciplinary cooperation with COMET AG, Switzerland, and the Karlsruhe Institute of Technology (KIT). I would like to extend my sincere thanks for their contribution towards the successful completion of this work.

Principally, I would like to extend my gratitude to Prof. Dr.-Ing. Rolf Jakoby for this doctoral work opportunity. His confidence, constructive discussions, motivation for an independent way of working and support in critical situations have been influential in solving critical problems in this work. Additionally, I want to thank Prof. Dr. rer. nat. Michael. J. Hoffmann, Karlsruhe Institute of Technology, for accepting to co-refer this thesis and for his illuminating discussion regarding the work done.

From Comet AG, Switzerland, I would like to thank Dr. Thomas Fink, Dr. Mike Abrecht, and Walter Bigler for their committed cooperation in the past. The valuable technical discussions have been a beneficial motivation in realizing the industry outlook of the work and generating new ideas for continuous product development. In the same cooperation, I would like to appreciate the support from my colleagues at KIT, Dr. Joachim R. Binder, Nicole Bohn and Kevin Häuser from the Institute for Applied Materials (Ceramic Materials and Technologies) for excellent cooperation. They have been influential in continuous material processing with constructive technical discussions.

At the IMP, I would like to extend a special thanks to my former colleague Dr.-Ing. Daniel Kienemund, for mentoring my work in the initial years of my doctorate, which formed the basis for the completion of this work. Among other former colleagues, I would like to thank Dr.-Ing. Holger Maune, Dr.-Ing. Dominik Walk, Matthias Nickel, Dr.-Ing. Christian Schuster, Dr.-Ing. Henning Tesmer and Dr.-Ing. Ersin Polat for enlightening me with the numerous technical discussions. A special thanks goes to my present colleague Dr.-Ing. Martin Schuessler, Stipo Matic, Dr.-Ing. Alejandro Jiménez Sáez, Dongwei Wang, Jesús Sánchez, Robin Neuder, Marc Späth and Markus Paravicini. Additionally, a special thanks goes to the technical staff, Andreas Semrad and Peter Kießlich, for helping me realize setup ideas.

Most importantly, I would like to thank my family, especially my mother Meenakshi,

the only person believing in my most important decision in life, my father Lalit for making me realize my boundaries, and my brother Nikunj for being a special friend throughout the journey. Additionally, I would like to thank my grandmother for bringing eternal positivity into my life and my grandfather for endless wisdom throughout. Finally, I would like to thank all the non-mentioned characters for motivating and supporting me throughout the doctorate journey.

Freiburg in Breisgau, June 2023

Prannoy Agrawal

Abstract

Barium strontium titanate (BST) composite ceramic varactors find their application in high-power impedance matching circuits in low-frequency ISM bands, particularly around 13.56 MHz. In this work, the modeling and in-house development of such varactors are presented, with emphasis on capacitance tunability and acoustic resonance behavior. These matching circuits are critical for plasma processes in the semiconductor industry, as they increase integrability and reduce the size of integrated circuits (ICs). Currently, mechanically-tuned varactors dominate implementation in these matching circuits because they are extremely low-loss and exhibit high linearity. However, they suffer from a limited tuning time of more than 1 ms, which opens up the possibility of implementing fast-tunable and comparatively compact tunable ferroelectrics such as pure BST-based varactors. In comparison, these varactors usually have higher losses. Consequently, to match the low-loss standards of mechanically tuned varactors, this work aims for BST-based composite varactors, where a low-loss and linear elastic dielectric such as magnesium borate (MBO) is added to the BST to reduce the material loss. BST losses are composed of two major components: dielectric loss and acoustic resonance loss. While dielectric loss has been extensively studied in the past, acoustic resonances due to electrostrictively induced piezoelectricity are less studied so far. Hence, they are one of the main focuses of modeling in this work. Another aspect of BST composites, tunability, has also been extensively researched, as previous models were either not sufficiently accurate or the tunability deviated significantly from experiments. Therefore, modeling of tunability becomes another focus area. A first distinct model is proposed that accurately and precisely predicts the tunable behavior of the BST composite varactor for arbitrary volume compositions of BST and MBO. Subsequently, the models are validated with the extracted measurements from the in-house electrical and Curie temperature T_C characterization setup. The tunability calculated from the electromagnetic simulations shows massive differences compared to the measured tunability. As a result, an in-house solution is formulated for incorporating Curie temperature shifts into the model due to the material changes during mixing, which helps to mitigate the massive deviations in tunability. For the 80 vol-% BST varactor, the tunability deviation between simulations and measurements decreases from 32% to about 2%, indicating the importance of integrating Curie temperature shifts. Moreover, in modeling acoustic resonances, a multiphysics approach consisting of RF and structural mechanics domains is implemented to mimic the effects of induced piezoelectricity under the influence of bias electric fields, which is responsible for such resonances. The model confirms the presence of acoustic resonances

at the same frequencies as in the measurements. A quasi-complete suppression of acoustic resonances is achieved in the BST composite varactor. A decrease of the equivalent series resistance from about 60 Ω to 10 Ω in the simulations and an increase of the Q-factor Q_ε from about 5 to 300 at 10 MHz under electric fields of 1.1 kV/mm, showing the crucial advantage of adding MBO to the BST material.

Kurzfassung

Barium-Strontium-Titanat (BST)-Komposit-Keramikvaraktoren finden ihre Anwendung in Hochleistungsimpedanzanpassungsschaltungen in niederfrequenten ISM Bändern, insbesondere um 13,56 MHz. In dieser Arbeit wird die Modellierung und hausinterne Entwicklung solcher Varaktoren vorgestellt, wobei der Schwerpunkt auf der Kapazitätsabstimmbarkeit und dem akustischen Resonanzverhalten liegt. Diese Abstimmungskreise sind für Plasmaprozesse in der Halbleiterindustrie von entscheidender Bedeutung, da sie die Integrierbarkeit erhöhen und die Größe integrierter Schaltungen (ICs) verringern. Derzeit werden in diesen Anpassungsschaltungen überwiegend mechanisch abgestimmte Varaktoren eingesetzt, da sie extrem verlustarm sind und eine hohe Linearität aufweisen. Sie leiden jedoch unter einer begrenzten Abstimmzeit von 1 ms, was die Möglichkeit eröffnet, schnell abstimmbare und vergleichsweise kompakte abstimmbare Ferroelektrika wie Varaktoren auf BST-Basis zu implementieren. Im Vergleich dazu haben diese Varaktoren höhere Verluste, und um die verlustarmen Standards von mechanisch abgestimmten Varaktoren zu erreichen, werden BST-basierte Verbundvaraktoren verwendet. In solchen Verbundvaraktoren wird dem BST ein verlustarmes und linear-elastisches Dielektrikum wie Magnesiumborat (MBO) hinzugefügt, um den Materialverlust zu verringern. Die BST-Verluste setzen sich aus zwei Hauptkomponenten zusammen: dielektrische Verluste und akustische Resonanzverluste. Während der dielektrische Verlust in der Vergangenheit ausgiebig untersucht wurde, sind akustische Resonanzen, die auf elektrostriktiv induzierte Piezoelektrizität zurückzuführen sind, noch weniger untersucht. Sie sind einer der Hauptschwerpunkte der Modellierung in dieser Arbeit. Ein weiterer Aspekt von BST-Verbundwerkstoffen, die Durchstimmbarkeit, wurde ebenfalls umfassend erforscht, da frühere Modelle entweder nicht genau genug waren oder die Durchstimmbarkeit erheblich von Experimenten abwich. Daher wird die Modellierung der Abstimmbarkeit zu einem weiteren Schwerpunktbereich. Es wird ein erstes eindeutiges Modell vorgeschlagen, das das abstimmbare Verhalten des BST-Verbundvaraktors für beliebige Volumenzusammensetzungen von BST und MBO genau und präzise vorhersagt. Die aus den elektromagnetischen Simulationen berechnete Abstimmbarkeit zeigt massive Unterschiede im Vergleich zur gemessenen Abstimmbarkeit. Infolgedessen wird eine hausinterne Lösung entwickelt, um Verschiebungen der Curie-Temperatur T_C in das Modell einzubeziehen, die auf die Materialveränderungen während des Mischens zurückzuführen sind, was dazu beiträgt, die massiven Abweichungen in der Abstimmbarkeit zu mildern. Für den 80 Vol-% BST-Varaktor sinkt die Abweichung der Abstimmbarkeit zwischen Simulationen und Messungen von 32% auf etwa 2%, was auf die Bedeutung der Integration von T_C Verschiebungen

hinweist. Darüber hinaus wird bei der Modellierung akustischer Resonanzen ein multiphysikalischer Ansatz, bestehend aus HF- und strukturmechanischen Domänen, implementiert, um die Auswirkungen der induzierten Piezoelektrizität unter dem Einfluss elektrischer Vorspannungsfelder nachzuahmen, die für solche Resonanzen verantwortlich sind. Das Modell bestätigt das Vorhandensein von akustischen Resonanzen bei denselben Frequenzen wie bei den Messungen. Die akustischen Resonanzen werden im BST-Verbundvaraktor nahezu vollständig unterdrückt. Ein Rückgang des äquivalenten Serienwiderstands von etwa 60 Ω auf 10 Ω in den Simulationen und ein Anstieg des Q-Faktors Q_ε von etwa 5 auf 300 bei 10 MHz unter elektrischen Feldern von 1,1 kV/mm zeigen den entscheidenden Vorteil des Zusatzes von MBO zum BST-Material.

Contents

Preface **iii**

Abstract **v**

1. Introduction and Motivation **1**

2. Fundamentals of Ferroelectrics **7**
2.1. Polarization 7
2.2. Dielectric Properties in Paraelectric Phase 11
2.3. Tunability Model Equations 20
2.4. Piezoelectricity and Electrostriction 24
2.5. Ferroelectric Composites and Loss Characteristics 29

3. Bulk-Ceramic Composite Varactors **33**
3.1. Design and Optimization 34
3.2. Fabrication and Processing 37
3.3. Small-Signal RF Characterization 40
3.4. Thermal Characterization of Capacitance and Shift in Curie Temperature 42

4. Modeling Tunability for Composite Varactors **47**
4.1. Existing Models and their Limitations 47
4.1.1. Analytical Models 48
4.1.2. CAD Modeling 52
4.2. Novel 3D-CAD Simulation Modeling 54
4.3. Structural Analysis of Substitution Effect 65
4.3.1. Thermal Analysis of Curie Temperature Shifts 66
4.3.2. Substitution Effect Modification 68

5. Modeling Acoustic Resonances and its Suppression **71**
5.1. Analytical Principle 71
5.2. 2D-CAD Acoustic Simulation Model 72
5.3. Evaluation and Prediction of Acoustic Resonances 86

6. Conclusion **91**

A. Appendix **97**
A.1. Graphical Abstract - Electromagnetic Tunability Model 98
A.2. Graphical Abstract - Modeling of Acoustic Resonances 99
A.3. Tertiary Modelling with MBO and Metallic Additives 100

B. Symbols and Abbreviations **103**

Bibliography **105**

Own Publications **115**

Co-author Publications **117**

Patent Contribution **119**

1. Introduction and Motivation

Moore's law has characterized the semiconductor industry since the 1980s, which observed that the number of transistors in a microprocessor expands by two times every 18 to 24 months, depending on the complexity of the semiconductors [BA21; LLP22]. Hence, over the last 30 years, a tremendous increase in wireless devices in modern communications systems, in the frequency range of up to 15 GHz, is witnessed. Moreover, the industry is predicted to grow even faster during the next 5–10 years to accommodate the increasing demand for semiconductor materials in emerging technologies, such as artificial intelligence (AI), autonomous driving, the Internet of Things (IoT), and 5G. This brings heavy competition among key players such as Intel Corporation, Nvidia Corporation, Kyocera Corporation, Qualcomm Technologies Inc., and STMicroelectronics NV, towards consistent research and development efforts [BA21; LLP22]. At the support end for these devices, analog or RFICs (Radio Frequency Integrated Circuits) are used in a wide range of applications, including fifth-generation (5G) radio base stations and portable device batteries. Due to constant development over the years, the RFICs market in this segment is expected to multiply. Parallel to communication and broadcast services, better safety standards and advanced driver assistance systems (ADAS) in the automotive industry have accelerated the demand for semiconductors-based sensors. In this segment, several smart applications, such as backup cameras, adaptive cruise control, blind-spot detection, etc., came into existence. In observation, the communication, broadcast devices, and sensors are getting smaller with time. They are becoming space-constrained, leading to the integration of many radio frequency (RF) components in a small area. It is evident from the fact that between 1989 and 2013, the density of transistors in a CPU arose from around 7500 per mm^2 to $5{\cdot}10^6$ per mm^2 [BA21].

As an increasing number of devices leads to congestion in the already overwhelmed RF frequency bands, the researchers are finding solutions by moving towards higher frequencies to get larger bandwidths. Various steps are required to fabricate the implemented RFIC's material, and their critical dimensions are expected to reach atomic boundaries (≈100 Å) in the future [BA21]. Additionally, the space constraint due to increasing package efficiency is equally responsible for such dimensions. Thus, the imperfections or roughness of the surface atomic layer contribute to these RF device's performance significantly [KTG18].

Generally, the manufacturing process of semiconductor material layers involves plasma etching and plasma deposition. Due to sub-nm thicknesses of the material

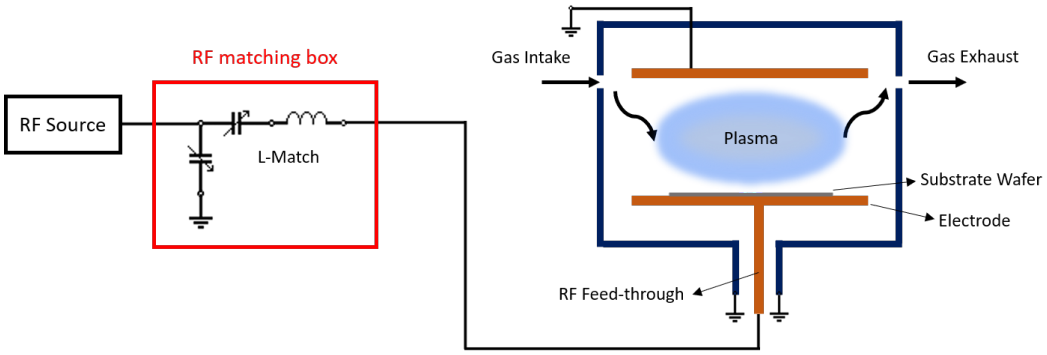

Figure 1.1.: Basic illustration of capacitively coupled plasma process schematics. The plasma in a vacuumed chamber with a parallel-plate assembly is generated by applying RF power. A capacitive tunable matching network ensures impedance matching between the RF power source and the plasma chamber.

layer in the present times, the precision of these plasma processes has become critical. In fact, in a decade, the thickness is expected to reach 3-4 times the Silicon atom size, making the precision of plasma-processed layers even more critical. The improved plasma processes focus on process stability, reproducibility, control, and integrating new features such as pulsed operation with cycling frequencies ranging from 0.1 to 1000 kHz [KTG18; Kan+15]. The key technique discussed throughout past decades is atomic layer etching (ALE). A simple capacitively coupled plasma (CCP) process schematic is shown in Figure 1.1, where capacitively driven RF discharges are used. The plasma is ignited between a parallel-plate electrode assembly, with feedstock gases injected throughout the vacuum chamber. The RF signal ionizes the gases to generate the plasma, and effluent gases are removed using a vacuum pump [LL05]. The DC excited plasmas are avoided, as the gas ions are trapped on the insulator. This generates an electric field opposing the DC excitation field, which does not let plasma survive. Over time, this has been succeeded by numerous generations of plasma etching or deposition devices, such as the inductively coupled plasma (ICP) from Panasonic [Pan08], depicted in Figure 1.2. The RF frequencies used for plasma excitation are located in the ISM frequency band, ranging from 13.56 MHz to 40.68 MHz.

The plasma system is characterized by three intervals, namely – the ignition phase, the working cycle, and the extinction phase. During the plasma ignition phase, a drastic impedance change occurs to generate plasma. To ensure maximum or requisite power transfer to the plasma chamber, a tunable impedance matching circuit is used, as shown in Figure 1.1 and 1.2. Here, the RF power levels reach around 10 kW, which requires high power matching circuits. Traditionally, these circuits consist of mechanically tunable varactors based on the parallel-plate topology with vacuum as the dielectric. The vacuum ensures high linearity and minimizes losses due to the

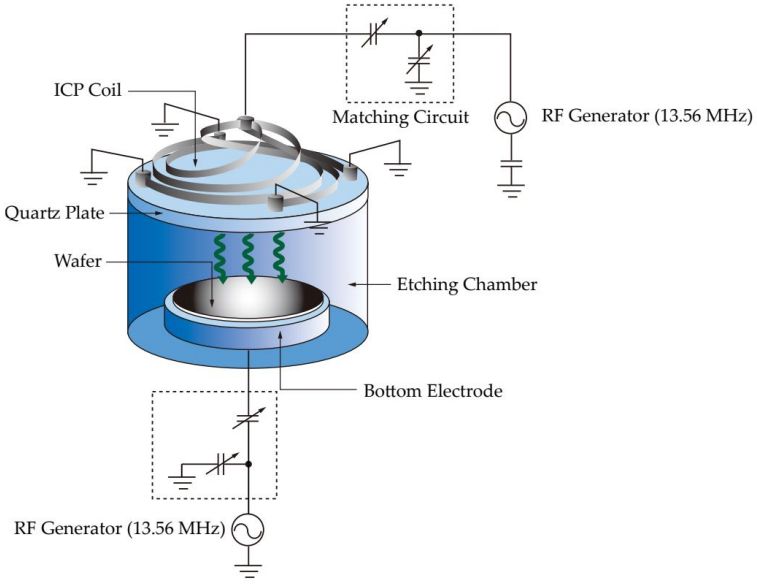

Figure 1.2.: Schematic Design of a Panasonic ICP dry etching system. The plasma is ignited inside an aluminum vacuum chamber at the ICP source on a quartz plate, using two impedance-matched RF sources at 13.56 MHz [Pan08].

metallic electrodes and the housing nearby. The capacitance of these varactors is changed by altering the surface of the electrodes or the gap between the electrodes using mechanical stepper motors. The stepper motors introduce a significant disadvantage of limited response times of around 1 s for a relative maximum change in capacitance. However, as the process times are the most critical parameter for establishing ALE-capable plasma processes, numerous efforts in research and development are made to reduce the duration of each interval. This challenges replacing these comparatively sluggish mechanically tuned varactors with much-accelerated tuning alternatives without compromising on other benefits such as low loss, high linearity, large tunability, and high power-handling capabilities.

Potentially, there are various candidates to replace mechanically tunable vacuum varactors such as semiconductor varactor diodes, PIN-diode switched capacitor banks, microelectromechanical systems (MEMS) based solutions, and varactors based on functional materials such as ferroelectrics. They account for their advantages and disadvantages regarding their use in plasma applications. The semiconductor varactor diode deals with a high dielectric loss, low linearity, and poor power handling, which makes them unsuitable despite high tunability [Che17; And+11]. Whereas the PIN-diode switched, capacitor banks deliver discrete capacitance values, which makes continuous tuning operation complex [Che17]. Although MEMS-based solutions are a promising alternative, their power handling capabilities and mechanical reliability under hot switching conditions make them inappropriate for

plasma applications [Che17; Cav20]. The ferroelectric-based solution provides excellent power-handling capabilities, and extremely fast and large tunability [Kie19; Wal21; Mau11], which makes them the best candidate among all to replace mechanically tuned varactors. The ferroelectrics deal with a high dielectric loss, which can be balanced to the desired levels using a ferroelectric and low-loss dielectric mixture.

Among ferroelectrics, barium strontium titanate (BST) is well known and is suitable for plasma applications due to its high power handling capabilities and large tunable properties. BST has been extensively used in various applications in three forms – thin-films [Wal21], thick-films [Mau11; Kie+18a] and bulk ceramics [Zha+10; Kie19]. Typically, the thin film finds applications in the GHz range, thick films in the MHz to GHz range, and bulk ceramics in the DC to lower MHz range. Due to the features and frequency range of the plasma applications, thick-film and bulk ceramic are the most suitable. However, bulk ceramic, exhibiting remarkably higher permittivity and tunability, becomes the desired choice for the plasma application environment. Additionally, the tuning is realized through an external DC biasing source, which is advantageous in maintaining continuous and fast tunability [Kie+18a]. Although BST has lower dielectric loss among ferroelectrics [Gev09], the overall losses (including metallic and housing losses) are still high for the plasma applications, which poses performance issues. Moreover, the induced piezoelectricity due to electrostriction possessed by the BST in the non-polar or paraelectric phase excites acoustic activity, which interferes with the electrical domain [GVL06; Gev09]. This interference further increases the loss in BST-based varactors. In this work, a composite BST material approach is adopted to reduce both dielectric loss and acoustic resonances. This approach adds a linear elastic and low-loss dielectric to BST while maintaining an optimum trade-off between reduction in tunability and overall losses. After generations of additives, few contenders qualify for consideration, such as Magnesium Oxide (MgO) [Zha+09; Hua+15], Magnesium Silicate (Mg_2SiO_4) [Tan+14], Magnesium Titanate (Mg_2TiO_4) [CZY07; Tan+14] and Magnesium Borate MBO ($Mg_3B_2O_6$) [ZZY11]. The MBO is chosen for its extremely low dielectric loss (i.e., high Q-factor $Q_\varepsilon \geq 2000$). Additionally, effectiveness in reducing sinter temperatures from around 1300 °C to around 1100 °C of the BST composites, further, strengthens their feasibility [ZZY11].

Since the 2000s, various literature has explored the reduction in the dielectric loss of BST-like ferroelectric such as [Mer+17; ZZY11]. These works have successfully demonstrated the reduction in dielectric loss of BST when used in composite form. Additionally, precise modeling efforts for reduced dielectric loss have been showcased in this area [She+06; JS08b; Wie+17; Lei15]. However, the acoustic and its suppression have not been studied much, apart from its detection and mitigation in BST-based varactors [Kie19; Kie+18a]. A proper understanding of acoustic activity and its suppression is still missing and poses one of the significant challenges for the reliability of the bulk ceramic varactors aimed in this work. In this direction, the developed model employs multiple physics – RF and structural mechanics to demon-

strate the suppression of acoustic activity by adding MBO into BST. The reduction of equivalent series resistance (ESR) from around 60 Ω to 10 Ω in the simulations highlights the significance of the model. Apart from losses, another major facet of the aimed varactors is the tunability of the composites, which is unexpectedly lower than the reduction in losses in relative comparison [ZZY11]. Hence, rigorous modeling efforts predicting accurate tunability are also needed for better varactor design. Since the early 2000s, numerous analytical and basic numerical models have been suggested, which showed proximity to the experiments for very short of the vol-% composition of dielectrics in ferroelectrics [She+06; JS08b]. Generally, these models focused on homogenizing the whole composites rather than focusing on the distribution of electric fields, which is a key to understanding their tunable behavior in depth. With the advancements in the emerging 3D electromagnetic modeling, the distribution of electric field in the composites is studied in detail [Wie+17; Lei15]. Although, precise and accurate modeling is still a challenge compared to experiments. The tunability model tunes the BST material by deepening the mesh environment and extracting the precise values. Additionally, this is the first model to consider the Curie temperature T_C shifts, ensuring the model's accuracy compared to the measurements. This is highlighted from the deviation reduction of tunability between simulation and measurements from around 32% to 2%, for 80 vol-% BST varactor. These two challenges regarding the modeling of tunability and acoustic resonance suppression of BST-based bulk ceramic composite varactors motivate this work's entire concept. The upcoming chapters will discuss these models in detail.

Outline

Initially, Chapter 2 discusses the fundamentals of non-linear dielectrics, i.e., ferroelectrics. It starts with the concept of dielectric polarization and its behavior in non-polar ferroelectrics, considering different model equations for tunability. This chapter concluded by discussing the ferroelectric material's electrostriction-induced piezoelectricity and ferroelectric composites. Further, Chapter 3 explores the design and fabrication of the bulk ceramic varactor, with the aspect of its thermal and electrical experimental characterization. Chapter 4 and 5 represent the essential part of this work, with the former demonstrating accurate and precise modeling of tunability of the BST composite bulk ceramic varactor and the latter presenting detailed modeling of detection and suppression of acoustic activity. Ultimately, the work is concluded, and a probable outlook in other application areas is summarized.

2. Fundamentals of Ferroelectrics

This chapter discusses the fundamental properties of non-linear dielectric material, i.e., ferroelectric, and their composites. The main focus is on reflecting the composite's importance and suitability for high-power RF applications. The associated piezoelectricity and induced electrostriction with the resulting acoustic behavior of the material are explained. In this regard, different ferroelectric-dielectric composite's advantages are also discussed. In addition, the various physical equations defining the behavior of ferroelectrics with their advantages and disadvantages are analyzed according to the model in consideration in this work.

2.1. Polarization

Electrical insulators that an externally applied electric field can polarize are known as dielectrics. Upon exposure to electric fields, the charges, instead of flowing from one electrode to the other as it happens in conductors, shift slightly from their average equilibrium position giving rise to dielectric polarization $\vec{p}$. This $\vec{p}$ defines the separation of electrical negative and positive charges and is represented as follows:

$$\vec{p} = q\vec{r}, \tag{2.1}$$

with $\vec{q}$ being the bounded stationary charge and r being the distance of the charges. Considering the macroscopic material as the arithmetic accumulation of these small microscopic charge elements, the total resultant polarization $\vec{P}$ is given by:

$$\vec{P} = \sum_j \vec{p_j}/V. \tag{2.2}$$

Moreover, in a compensatory reaction, the resultant shift in the stationary bound charges is opposite to the applied external electric fields. The displacement field of such polarizable materials is written as following [JS08a; New05; Poz04; Mar13]:

$$\vec{D} = \varepsilon_0(1 + \chi_e)\vec{E}, \tag{2.3}$$

$$\varepsilon_r = 1 + \chi_e, \tag{2.4}$$

$$\vec{D} = \varepsilon_0 \varepsilon_r \vec{E}, \tag{2.5}$$

where ε_0 is the vacuum permittivity, the relative permittivity ε_r, the susceptibility χ_e and the externally applied electric field E. Consequently, for a linear, isotropic dielectric, the polarization in this term is [JS08a; New05; Mar13]:

$$\vec{P} = \varepsilon_0 \chi_e \vec{E}. \tag{2.6}$$

Global polarization is summed up by four different mechanisms, namely - electronic, atomic, dipolar, and ionic polarization. Each mechanism is characterized by relaxation frequency. With the increasing frequency, the faster mechanisms become dominant and slower mechanisms drop off [Poz04]. These faster mechanisms contribute to the dielectric storage ($k' = \varepsilon'/\varepsilon_0$). The dielectric loss factor($k'' = \varepsilon''/\varepsilon_0$), though, will peak at each critical frequency, marking the change of dielectric mechanisms. This is depicted in Figure 2.1. When a dielectric is exposed to the external electric fields, the nearby bounded but oscillating molecules, ions, and electrons are polarized. These collide with the surrounding material's stationary particles, contributing to dielectric losses. Additionally, ohmic or conduction losses are negligible due to colliding with the surroundings' stationary conductive material.

Electronic polarization occurs in neutral atoms when the applied electric field displaces the nucleus concerning the surrounding electrons. In atomic polarization, the close pair of positive and negative ions move away from each other under the influence of an applied electric field. Due to the polarizability of the atoms and molecules,

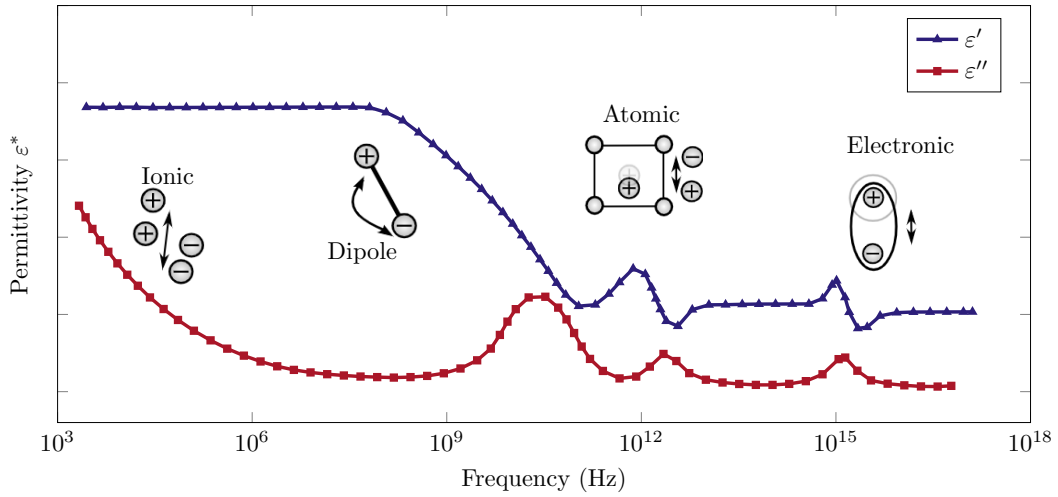

Figure 2.1.: Complex permittivity variations for dielectrics concerning the frequency. Additionally, the respective dominant polarization mechanisms are mentioned near their frequency range.

both electronic and atomic polarization generates induced dipole moments. Moreover, a permanent dipole moment is sometimes generated due to the unbalanced sharing of electrons. When the external electric field is absent, these dipole moments orient in such a random order that the resultant polarization and the shifts of atoms or nucleus are zero. However, under an external electric field, when the dipoles rotate to align with the electric field instead of shifting, causes dipole polarization to occur. Lastly, ionic polarization results from ionic conduction and interfacial or space charge polarization. This dielectric mechanism is most prevalent with dominant ionic conduction at low frequencies. Additionally, the losses are higher due to ionic conduction. Space charge polarization arises due to the accumulation of mobile charges at structural surfaces and interfaces due to incompatible chemical sequences or trapped charge carriers at the interfaces of these heterogeneous systems. These accumulated charges cause electric field distortion, increasing the material's overall capacitance. This increase is analogous to the rise in k'. For the initial frequencies, all the mechanisms contribute to global polarization. As the frequency increases, the slower mechanism drops off, and hence, the dielectric storage reduces, depicted with the reduction in ε' in Figure 2.1.

Moreover, some time is needed to move charges or rotate dipoles under external alternating electric fields. This non-instantaneous behavior of polarization change creates a phase difference between the excitation field and polarization. This makes the permittivity frequency dependent when an RF electric field is applied [JS08a; New05; Mar13]. This permittivity is represented as follows:

$$\varepsilon^*(\omega) = \varepsilon(\omega)' - j \cdot \varepsilon(\omega)'', \tag{2.7}$$

where ω is the frequency of the applied external RF signal. The ionic and electronic polarization mechanisms are the most important for microwave frequencies in this work. These mechanisms can be compared to a mechanically-driven damped harmonic oscillator (like a mass on a spring), and resonance phenomena characterize the frequency dependence. Consequently, peaks in a plot of dielectric storage ε' versus frequency are observed at the resonance frequencies of the ionic and electronic polarization mechanisms. A dip follows this peak at frequencies just above each resonance peak, which is a general form of a damped resonance reaction, corresponding to the out-of-phase response of the system with the driving force, i.e., the externally applied RF signal [JS08a; TM12]. Mathematically, such a system is expressed as:

$$\frac{q}{m_q}\vec{E}(t) - \frac{\partial^2 \vec{r}(t)}{\partial t^2} - \Gamma \frac{\partial \vec{r}(t)}{\partial t} - {\omega_0}^2 \vec{r}(t) = 0, \tag{2.8}$$

where m_q is the mass of the charge q, Γ is the damping coefficient of the motion in charge, ω_0 is the resonance frequency of this motion and $E(t)$ is the excitation signal. In the frequency domain, this is represented as:

$$\frac{q}{m_q}\vec{E}(\omega) + \omega^2\vec{r}(\omega) - \omega\Gamma\vec{r}(\omega) - {\omega_0}^2\vec{r}(\omega) = 0, \tag{2.9}$$

where ω is the frequency of the excitation signal $E(\omega)$. Solving this equation for $r(\omega)$, the following is obtained:

$$\vec{r}(\omega) = \frac{q\vec{E}(\omega)}{m_q({\omega_0}^2 - \omega^2 + j\omega\Gamma)}. \tag{2.10}$$

Consequently, according to the Equation (2.1), the polarization of this charged particle is given by:

$$p(\omega) = \frac{q^2\vec{E}(\omega)}{m_q({\omega_0}^2 - \omega^2 + j\omega\Gamma)}. \tag{2.11}$$

As displacement field's relation with polarization is given by:

$$\vec{D} = \varepsilon^*\vec{E} = \varepsilon_0\vec{E} + p, \tag{2.12}$$

the resultant complex dielectric response ε^* is as follows:

$$\varepsilon^* = \varepsilon_0\left[1 + \frac{q^2}{\varepsilon_0 m_q({\omega_0}^2 - \omega^2 + j\omega\Gamma)}\right] = \varepsilon' - j\varepsilon'', \tag{2.13}$$

which represents the same form as in Equation (2.12). Here the real part denotes the dielectric storage depicting energy retained by the material, and the imaginary part denotes the reflected or dissipated energy in the form of losses. As a result,

$$\tan\delta = \frac{\varepsilon''}{\varepsilon'} = \frac{1}{Q}, \tag{2.14}$$

denotes the dielectric losses or characterizes the dissipation loss of the material. The resultant global polarization $\vec{P}$ of the dielectric material, though, is zero without an external electric field. This is due to random dipole moments of each polarized charge summing up to zero. If this summed polarization is not zero, it gives rise to a new set of dielectric materials known as ferroelectrics, which are the focus of the upcoming section.

2.2. Dielectric Properties in Paraelectric Phase

Dielectric, crystalline, and electroacoustic properties of perovskite ferroelectrics have been extensively studied. These materials have been broadly employed in microwave devices due to such properties. The complex metal oxide ferroelectrics such as titanates ($CaTiO_3$, $BaTiO_3$, $Ba_xSr_{1-x}TiO_3$, etc.), tantalates ($KTaO_3$, etc.), niobates ($KNbO_3$, etc.), which are characterized by general chemical composition, ABO_3, constitutes these perovskite ferroelectrics. This work focuses on the ferroelectric $Ba_xSr_{1-x}TiO_3$, as shown in Figure 2.2. This figure depicts the general temperature characteristics, where below and above Curie temperature T_C region denotes the polar and non-polar phase, respectively. The polar phase is characterized by the remnant polarization P_R, which is present without any external electric field and possesses a non-centrosymmetric arrangement. The non-polar phase, though, possesses a centrosymmetric and cubic structure with no P_R [Pau06]. Apart from temperature, the permittivity depends on the electric field and electromechanical strain, which is discussed extensively in upcoming sections.

The non-polar phase, also known as the paraelectric phase, is essential for tunable electrical applications due to less ferroelectric loss and no hysteresis. Therefore, the considered tunable varactor application desires the ferroelectric to be in the paraelectric phase to reduce the effects of ferroelectricity. Although, in the paraelectric phase, piezoelectricity phenomena reappear when the material is exposed to an externally applied electric field. This is a result of the electrostriction in the material. Moreover, the critical aspect of the voltage-dependent permittivity of the ferroelectric in the paraelectric phase enables the use of such functional materials in tunable

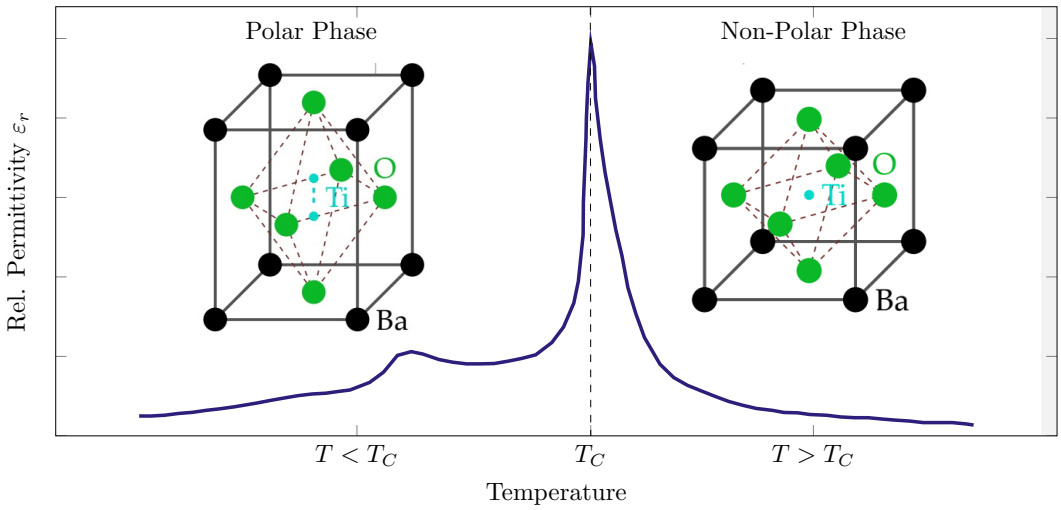

Figure 2.2.: Basic illustration of permittivity dependence on temperature of perovskite ferroelectrics with ABO_3 crystal structure. Here $BaTiO_3$ is considered as the perovskite crystal, which depicts centrosymmetry in the non-polar phase.

radio frequency (RF) applications. However, it is essential to note that few tunable electrical applications in the non-polar phase utilize piezoelectric phenomena for generating surface or bulk acoustic waves.

According to Equation (2.6), the susceptibility χ_e for the non-linear dielectrics is field dependent in the form as:

$$\chi_e(E) = \frac{1}{\varepsilon_0} \cdot \frac{\partial P(E)}{\partial E}, \tag{2.15}$$

and according to Equation (2.4), a permittivity depending on the electric field is obtained. This forms the basis for various tunable RF applications. In observation, higher permittivity leads to larger tunability. Hence, these applications must be placed just above the T_C for maximizing tunable behavior. Figure 2.3 illustrates the electric field-dependent polarization curve of the general ferroelectrics, with P_S depicting the spontaneous polarization. When an external field is applied, a small amount of coercive electric field E_C is needed to compensate for a considerable remnant polarization P_R associated with the ferroelectric material. To regain this associated P_R, an opposite directed coercive field strength of E_C is applied. This effect creates a hysteresis loop, which leads to increased losses in a ferroelectric material under an alternating electric field. These losses are due to the rearrangement of domains at the same polarization magnitude and direction, whereas the electric

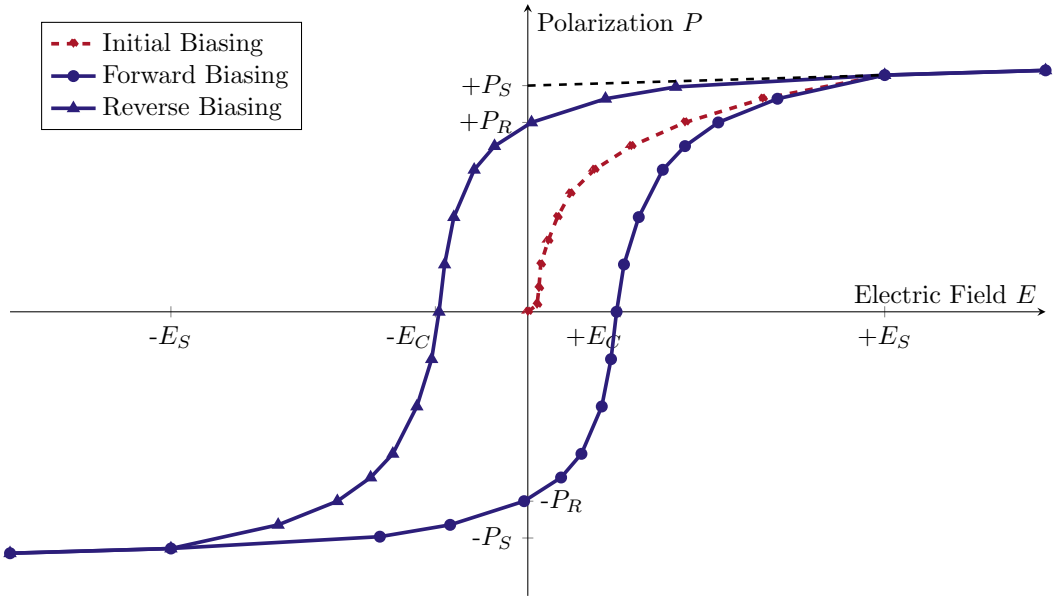

Figure 2.3.: The electric field-dependent polarization curve (hysteresis) of the general ferroelectric. Spontaneous Polarization P_S characterizes such materials, representing the stored polarization effects.

field varies. Each region with uniform polarization represents a ferroelectric domain, and the interface boundary between two adjacent coherent domains with the same polarization is called a domain wall. Such characteristics of a ferroelectric crystal with discrete orientations agree with the strain compatibility relation. Both polarization rotations or elongations and domain wall motions are the influential factors in controlling the macroscopic properties of ferroelectrics [JS08a; SB01; Su03; Zho+12].

Frequent developments in electromechanical devices continuously force the evolution of new ferroelectric materials in the context of an understanding of external electric field-induced behavior, including piezoelectric response and energy loss (or dissipation) behavior. The total loss is generally separated into three parts – elastic, dielectric, and piezoelectric losses [Tic+08; Zen+12; Jaf58]. Nowadays, conscious efforts are made towards reducing such energy loss of ferroelectrics, leading to a better understanding of anelasticity, dielectric relaxation, and piezoelectric hysteresis [JS04; Koh+15; Koh+13]. In the application environment, energy loss causes enormous heat dissipation in tunable electrical devices under a robust electromagnetic field environment, leading to device failure, especially in high-power applications [Jaf58; Zha+09; HJB10; AM11]. Each component's dimensions reach the micrometer range for high-frequency electrical applications, making thermal sensitivity crucial. Hence, high attenuation significantly affects the performance [Sla07]. Most commercial ceramic-based capacitors employ ferroelectrics as tunable dielectric, where high capacitance values and high electrical breakdown field strength are required in the low to medium frequency range. Due to their thermal and voltage dependence, they have been classified as class 2 dielectrics according to industrial standards. Generally, class 1 dielectrics include thermally and electrically stable ceramics [Vis15; LLC14].

Based on a simplified version of Equation (2.9), a 1D model of a perovskite crystal in paraelectric (non-polar) and ferroelectric (polar) phase is illustrated in Figure 2.4. In Figure 2.4b, a paraelectric centrosymmetric phase is depicted, where the central ion, which is Ti^{4+} ion in BST, oscillates around the equilibrium position of ($y = 0$) and the free energy response is distinguished by a parabolic response ($\approx ky^2$). When an external electric field is applied, the central ion shifts along the y-axis depending on the polarization direction, forming an electric dipole. The magnitude of the applied electric field decides the new equilibrium position at which the central ion shifts. Consequently, the stored dipole moment and the intensity of oscillations reduces, which leads to reduced permittivity. After removing the external electric field, the central ion returns to its original equilibrium position. This is the primary tunability mechanism used in the tunable electric application environment [Koh+13; Koh+15; Zha+09]. Moreover, for the polar or ferroelectric phase in Figure 2.4a, there exist two equilibrium phases with the central ion being shifted towards either one based on the direction of remnant polarization P_R. In these equilibrium positions, the free energy of the crystal is minimum. When an electric field is applied, the center ion may switch from left to right equilibrium position or vice versa, depending on the

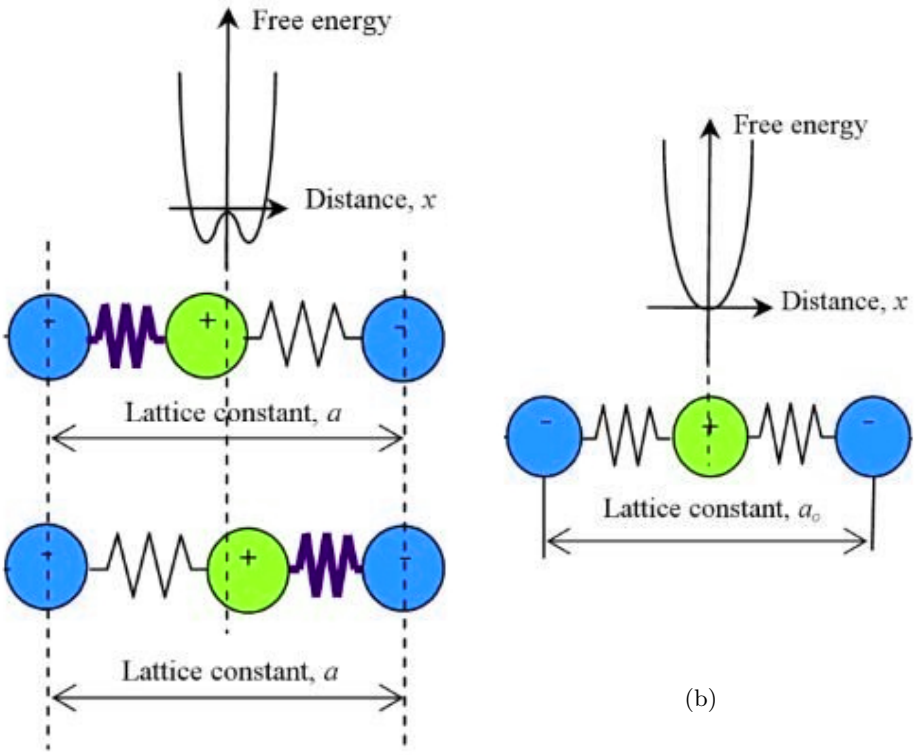

Figure 2.4.: Free energy behavioral comparison between polar (a) and non-polar phase (b). A clear distinction in the form of stored polarization is witnessed, represented by Spontaneous Polarization P_S in the non-polar phase. Consequently, the central ion is shifted towards one of the adjacent ions to compensate for the P_S.

direction of the polarization. After reversing the electric field's direction, the center ion returns to its original equilibrium position, restoring the previous polarization. This switching mechanism is employed in various memory applications [Li+19].

Moreover, when a tunable material is used in the form of a parallel plate capacitor, the capacitance C is denoted by the following relation:

$$C = \varepsilon_0 \varepsilon_r(E) \frac{A}{l}, \tag{2.16}$$

where A is the cross-section area and l is the thickness of the dielectric layer between the metal electrodes. The parallel plate topology permits adequate electric field penetration inside the dielectric material. Hence, a close correlation between relative permittivity ε_r and capacitance C is drawn, resulting in the tunability of the capacitor and the tunability of the dielectric material comparable to each other [Mau11], and this relation is expressed as:

$$\tau_\varepsilon = \frac{\varepsilon_r(E=0) - \varepsilon_r(E=E_{bias})}{\varepsilon_r(E=0)} = \frac{C(V=0) - C(V=V_{bias})}{C(V=0)} = \tau_C, \tag{2.17}$$

where E_{bias} is the generated bias electric field at input voltage V_{bias}. However, the capacitor's performance is characterized by the material quality factor and is stated as follows:

$$\eta = \frac{\tau_\varepsilon}{\tan(\delta)} = \tau_\varepsilon \cdot Q_\varepsilon, \tag{2.18}$$

where $\tan(\delta)$ and Q_ε are the loss tangent and Q-factor, respectively, defining the dielectric loss of the tunable dielectric material. This work employs Barium Strontium Titanate $Ba_xSr_{1-x}TiO_3$ (BST) as the ferroelectric material for its high and fast voltage-responsive tunability. Next, this material's characteristics are discussed in detail.

Barium Strontium Titanate as Mixed-Crystal Ferroelectric

The ferroelectric material's permittivity is dependent heavily on temperature. The permittivity is maximum at the Curie Temperature T_C for the bulk ceramic-based ferroelectric varactors. Consequently, the dielectric tunability τ_ε is highest at the T_C. Hence, it is desired for the varactor to operate near the T_C. Further, the associated dielectric loss is extremely high near T_C. Therefore, an appropriate difference between T_C and operating temperature is maintained to obtain an advantageous dielectric loss and dielectric tunability trade-off. This trade-off is concluded by evaluating the material quality factor η mentioned in Equation (2.18). Most applications generally demand room temperature as the operating temperature to avoid extra equipment for maintaining different temperatures. As there are no recognized naturally-occurring perovskite ferroelectrics around room temperature, mixed crystal solutions are synthesized to optimize the T_C of the resultant perovskite. An example of such a mixed crystal perovskite is synthesized using Barium Titanate $BaTiO_3$ and Strontium Titanate $SrTiO_3$, whereas their T_C stands at $393K$ and $42K$, respectively. By choosing an adequate stoichiometric ratio of these two perovskites, the T_C of the resultant solid solution is set [KP59; Lau+05; Kim+13]. If the stoichiometric ratio x is taken for $BaTiO_3$ and the rest for $SrTiO_3$, then the resulting solid solution is as $Ba_xSr_{1-x}TiO_3$. Figure 2.5 illustrates the relative permittivity ε_r variations concerning temperature for different stoichiometric ratios, extracted from the impedance measurement at 1 kHz [Jeo04]. However, the T_C is evaluated as a function of x, and the relation is given as [Tag+03]:

$$T_C(x) = (42 + 439.37x - 95.95x^2)K. \tag{2.19}$$

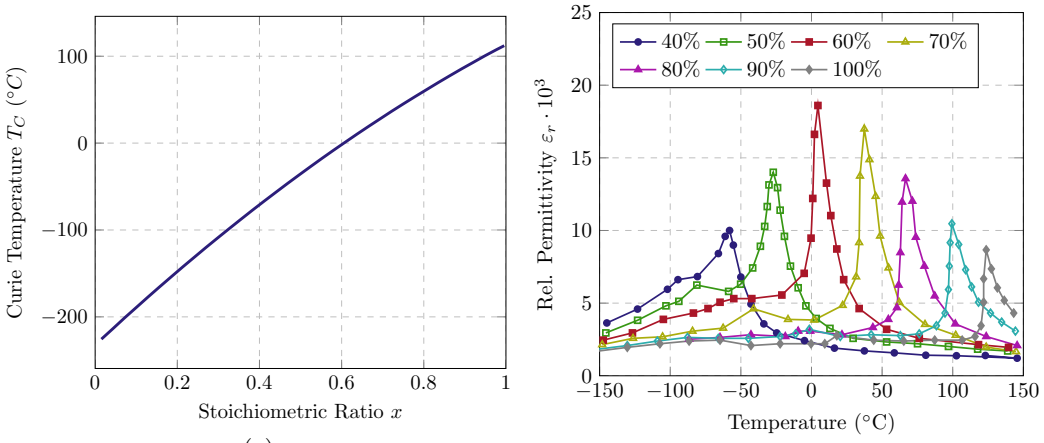

Figure 2.5.: The variation of Curie Temperature T_C concerning stoichiometric ratio x of BST is depicted in (a), whereas (b) illustrates the permittivity distribution concerning temperature for different x.

The increasing x increases T_C and is noticed in Figure 2.5. For x = 60% and 70%, the T_C = 2°C and 29°C, respectively. This work utilizes these BST stoichiometric ratios, which depict suitable loss and tunability trade-offs for room temperature and 50°C operating temperature, respectively. However, if other operating temperatures are required, the solid solution system is adjusted to the changed environment by altering the stoichiometric ratio x. However, the high-temperature sensitivity of the permittivity of BST perovskite ferroelectric makes technical use for tunable components in the microwave range difficult. The difference between T_C and operating temperature also partially compensates to reduce permittivity temperature sensitivity. Additionally, a high relative permittivity of BST perovskite ferroelectric requires extreme miniaturization of transmission line structures, which makes the impedance matching to existing RF equipment easier. Generally, devices are matched to 50Ω system impedance, which leads to fabrication-wise complex miniaturization of the BST layer thickness, posing complications in exciting resonating phenomenon [SN66; Ven+08]. These limitations are partially compensated with the introduction of BST thick films and bulk-ceramic technology. Figure 2.6 demonstrates the permittivity curve, modeled according to [VVK00], for the BST perovskite ferroelectric in bulk-ceramic and thick film technology for two different stoichiometric ratios x = 60% and 80%. A strong difference in permittivity values is witnessed for two different technologies, verified with the permittivity values at T_C and the temperature coefficient of each technology. Next, a mathematical description of the permittivity due to free energy associated with the perovskite ferroelectrics forms the basis for permittivity variations with respect to the electric field, temperature, and other physical parameters.

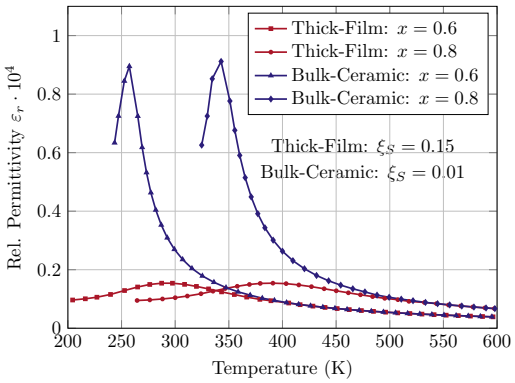

Figure 2.6.: The permittivity variations with respect to temperature of the BST with stoichiometric ratio x. The variations are based on the model by Vendik et al. [VVK00]. The BST layer's density difference due to thick-film and bulk-ceramic is witnessed by a difference in temperature at maximum permittivity and temperature coefficient ζ_S.

Thermodynamic Theory

The theory is built upon expanding the free energy of a ferroelectric crystal as a function of polarization P and temperature T [Tag05]. The relation is given as follows:

$$F(P,T) = \frac{1}{2}\alpha P^2 + \frac{1}{4}\beta P^4 + ..., \tag{2.20}$$

where higher-order terms are ignored. The variables α and β are dielectric-dependent and coefficients of Taylor series expansion in temperature T. The presence of even terms only indicates that the free energy does not depend on the direction of polarization. This relation holds true for both the phases –paraelectric (non-polar) and ferroelectric (polar). The equivalent electric field is given by:

$$\frac{\partial F(P,T)}{\partial P} = E = \alpha P + \beta P^3 + ... \tag{2.21}$$

Furthermore, the variable α is given by:

$$\alpha = \frac{1}{\varepsilon} = \frac{1}{\varepsilon_r \varepsilon_0}, \tag{2.22}$$

where ε is the dielectric permittivity of the ferroelectric. If $E = 0$ i.e. no external field is applied, the Equation (2.21) gives two solutions of spontaneous polarization P_S possessed by perovskite crystal, and are as follows:

$$P_S = 0, \tag{2.23}$$

which represents the paraelectric phase and

$$P_S = \sqrt{\frac{-\alpha}{\beta}}, \tag{2.24}$$

representing the ferroelectric phase. According to Curie-Weiss law [Tag05], which is stated as:

$$\varepsilon_r = \frac{C_r}{T - T_C}, \tag{2.25}$$

the α modifies to:

$$\alpha = \frac{T - T_C}{\varepsilon_0 C}. \tag{2.26}$$

The T_C is the Curie temperature, and C_r is the Curie-Weiss constant depending on the material. According to the Equation (2.21), the dielectric permittivity is given by:

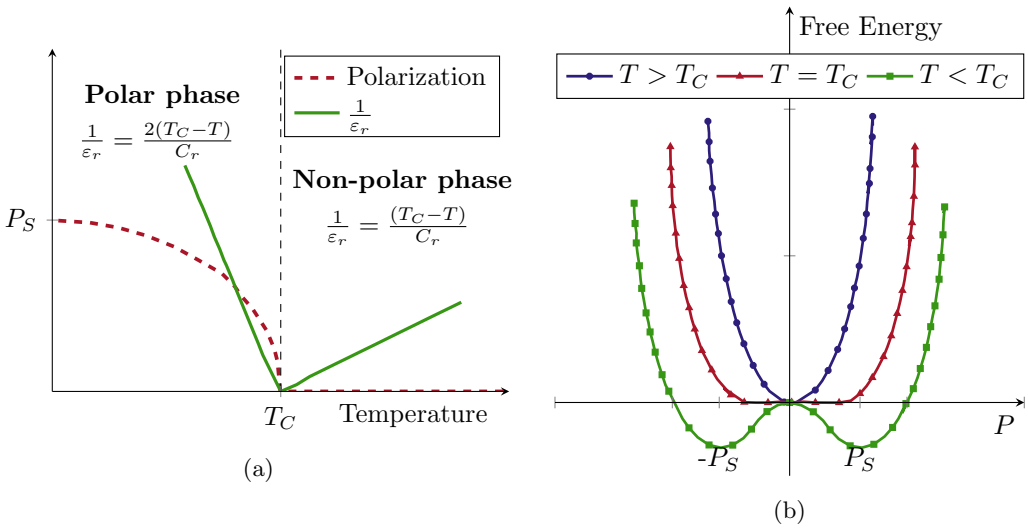

Figure 2.7.: The spontaneous polarization P_S and inverse-permittivity $1/\varepsilon_r$ are illustrated in (a), which briefly demonstrates the comparison between the polar and the non-polar phase, and the transition at Curie Temperature T_C. Moreover, (b) depicts the free energy transition with the polarization P for different temperature regions. The P_S is present only for the temperatures $T < T_C$, representing the polar phase, whereas $T > T_C$ represents the non-polar phase.

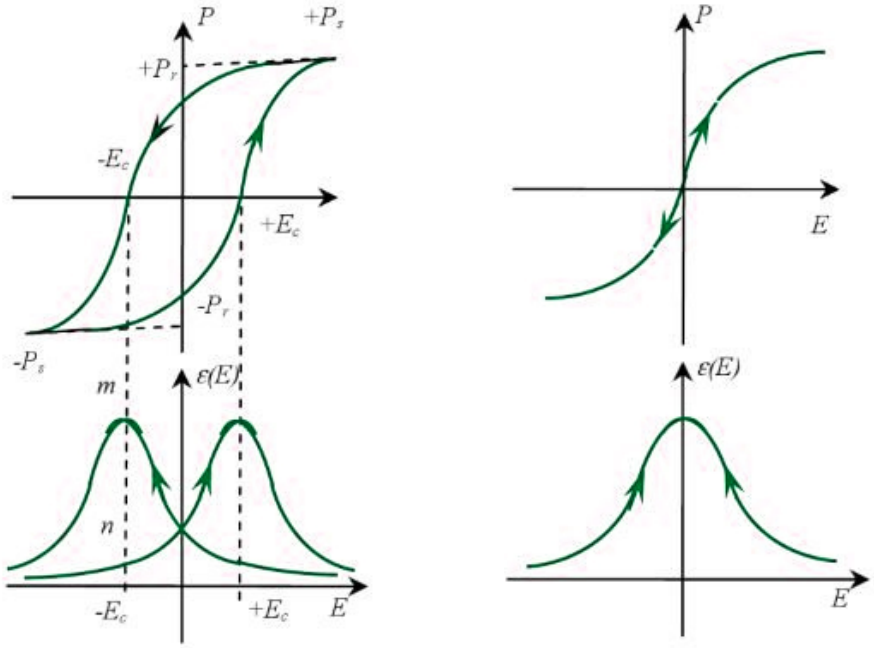

Figure 2.8.: The polarization P and permittivity ε variation comparison with respect to electric field E. (a,b) illustrating for polar and non-polar phase, respectively. The hysteresis loop completely vanishes in the ideal non-polar phase [Tag+03; Tag05].

$$\varepsilon_r = \frac{1}{\varepsilon_0} \cdot \frac{\partial E}{\partial P} = \frac{1}{\varepsilon_0(\alpha + 3\beta P^2)}. \tag{2.27}$$

Therefore, after considering Equations (2.23) and (2.26) for the paraelectric phase, the dielectric permittivity is the same as Curie-Weiss law:

$$\varepsilon_r = \frac{C_r}{T - T_C}. \tag{2.28}$$

Similarly, after considering Equations (2.24) and (2.26) for the ferroelectric phase, the dielectric permittivity is as:

$$\varepsilon_r = \frac{C_r}{2(T - T_C)}. \tag{2.29}$$

Figure 2.7 illustrates the variation of P_S and $1/\varepsilon$ with respect to temperature for both phases – paraelectric (non-polar) and ferroelectric (polar). As the temperature increases, the P_S reduces to zero at $T = T_C$ and remains zero, which is in accordance

with Equations (2.24) and (2.23) for polar and non-polar phase, respectively. Similarly, $1/\varepsilon_r$ is depicted in both phases, according to the Equations (2.29) and (2.28). Additionally, the figure demonstrates the transition of free energy characteristics with polarization P. If $T < T_C$, effects of stored polarization or energy are overcome by an oppositely directed spontaneous polarization P_S, and a further increase in this polarization leads to a rise in free energy. Whereas, for $T \geq T_C$, due to the absence of stored polarization or energy, the free energy increase with polarization from $P > 0$. Figure 2.8 summarizes the relation of polarization P and permittivity ε dependence on electric field E in both polar and non-polar phase. In conclusion, this figure presents the feasibility of electrical application in the non-polar phase, as each electric field magnitude leads to the same permittivity maintaining consistent tunable behavior. As tunable electric applications with electric bias are the focus of this work, the next section discusses the various forms of the Equation (2.27), which are dependent on bias electric fields, temperature, and other physical parameters.

2.3. Tunability Model Equations

Various model equations of the permittivity of non-ideal crystals have been developed based on the Ginzburg-Landau theory. In this regard, the models by Vendik et al. [VTZ98; VVK00], and Chase et al. [CLY05] are more popular. However, both models are primarily suited for describing the properties of BST thin films. However, they can also be applied, with acceptable minor errors, to BST thick films or bulk ceramics. Moreover, the model equation according to Weil [Wei03] is a simplified model equation, which is developed especially for BST thick films and bulk-ceramics approach and is focused on and applied extensively in this work. In this section, these three models are presented and compared in brief.

Vendik Model Equation

The model by Vendik et al. [VTZ98; VVK00] is the most versatile, complete, and complex model equation of all the three models considered in this work. This model equation depends on three broad parameters – electric field, temperature, and material quality. After modifications to the Ginzburg-Landau theory, the relative permittivity in the paraelectric phase is given by:

$$\varepsilon_r(E,T) = \frac{\varepsilon_{00}}{\left(\sqrt{\zeta^2+\nu^3}+\zeta\right)^{\frac{2}{3}} + \left(\sqrt{\zeta^2+\nu^3}-\zeta\right)^{\frac{2}{3}} - \nu + \Upsilon}, \tag{2.30}$$

where ν and ζ is as:

$$\nu(T) = \sqrt{\left(\frac{\Theta_F}{4T_C}\right)^2 + \left(\frac{T}{T_C}\right)^2} - 1, \tag{2.31}$$

and

$$\zeta(E, \xi_S) = \sqrt{\left(\frac{E}{E_N}\right)^2 + \xi_S^2}. \tag{2.32}$$

Apart from electric field strength and temperature, the ν and ζ are dependent on the crystal structure as well, which is indicated by the presence of the effective Debye temperature Θ_F, the Curie temperature T_C of the material and the ξ_S representing the statistical dispersion of the electric fields. Additionally, $\varepsilon_{00}(= C_r/T_C)$ is the Curie constant, E_N is the normalizing electric field, and Υ is the dielectric loss factor depending on temperature, electric field strength, and frequency. Considering a simplified case for an ideal BST crystal, the $\xi_S = 0$ and $\Theta_F = 0$, which gives:

$$\zeta(E) = |E| \frac{1}{2} \sqrt{27\beta[\varepsilon_0 \nu(T) \varepsilon_r(T)]^3}. \tag{2.33}$$

This is in acceptance with [Tag+03; Tag05; Gie09] and leads to accurate results. In practice, the model becomes extremely complex in the electromagnetic simulation environment due to the involvement of various physical parameters apart from the electric field.

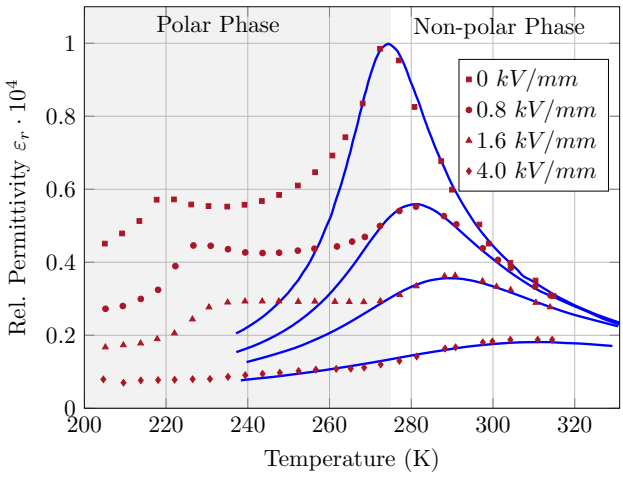

Figure 2.9.: Relative Permittivity ε_r variations with the temperature at various bias fields according to Vendik et al., with $\xi_S = 0$, are depicted here with blue line [Men+11]. The red markers depict the extracted relative permittivities from the measurements.

Chase Model Equation

Another model equation based on the Ginzburg-Landau theory is developed especially for the thin films ferroelectric. This equation is presented in [CLY05] for $Ba_{0.5}Sr_{0.5}TiO_3$ thin films. This model is based on two parameters, namely – maximum permittivity $\varepsilon_{r,max}$ and the field strength E_2, at which the permittivity is tuned to 50%. The resulting equation from the model is stated as follows:

$$\varepsilon_{\mathrm{r}}(\mathrm{E}) = \frac{\varepsilon_{\mathrm{r,max}}}{2\cosh\left[\frac{2}{3}\sinh^{-1}\left(\frac{2\mathrm{E}}{\mathrm{E}_2}\right)\right] - 1}. \tag{2.34}$$

Here E is the applied electric field and is the only variable the model depends on, making this equation one of the viable and less complex options for the electromagnetic environment [Sch07]. The model equation is dependent only on E, and other parameters such as temperature and material properties are not considered. Thus, its integration with an electromagnetic simulation environment like CST Studio Suite is fairly straightforward.

Weil Model Equation

Similar to the Chase model equation, the Weil model equation is dependent on an input electric field with an extension of two fitting parameters – a_1 and a_2, and one support parameter, associated with two different measurement points at different input electric field. The resulting equation for relative permittivity is given by:

$$\varepsilon_{\mathrm{r}}(\mathrm{E}) = \varepsilon_{\mathrm{r,max}}\left[1 - \tau_{\mathrm{E_A}}\frac{(1 + \mathrm{a_1} + \mathrm{a_2})|\mathrm{E}/\mathrm{E_A}|^2}{1 + \mathrm{a_1}|\mathrm{E}/\mathrm{E_A}| + \mathrm{a_2}|\mathrm{E}/\mathrm{E_A}|^2}\right], \tag{2.35}$$

and the resultant tunability is stated by:

$$\tau_{\varepsilon}(\mathrm{E}) = \tau_{\mathrm{E_A}}\left[\frac{(1 + \mathrm{a_1} + \mathrm{a_2})|\mathrm{E}/\mathrm{E_A}|^2}{1 + \mathrm{a_1}|\mathrm{E}/\mathrm{E_A}| + \mathrm{a_2}|\mathrm{E}/\mathrm{E_A}|^2}\right], \tag{2.36}$$

Here E is the electric field, acting as the primary variable, and the two different measurements are at $E = 0$ and $E = E_A$. Additionally, $\varepsilon_{r,max}$ is the relative permittivity at E_0, and τ_{E_A} is the tunability between the two measured points. It is observed that more accurate results are expected when $E = E_A$ is chosen such that the τ_{E_A} is around half of the maximum tunability achieved.

Model Equation Comparison and Choice

The basic Ginzburg-Landau theory forms the basis of all the individual model equations. These equations are differentiated by their assumptions and simplifications but are used for describing all ferroelectric materials in the paraelectric phase equivalently. Figure 2.10 illustrates the ideal $Ba_{0.6}Sr_{0.4}TiO_3$ solid bulk-ceramic with $\varepsilon_r \approx 2500$ at room temperature, i.e., 295 K and zero bias field. The parameter values for different models are mentioned in Table 2.1. The model of Vendik et al. is the most complex and versatile of all the above-mentioned models as it strongly depends on physical material parameters, apart from variables – environmental temperature and electric field strength [Men+11]. Whereas the models of Chase et al. and Weil et al. depend on variable electric field strength and basic related fitting parameters. Among these two, Chase et al. is the easiest to extract parameters from the measured data. However, Weil et al. offer a better adaptation to the measured observations due to the presence of two fit parameters and one support parameter.

Due to the electromagnetic simulation environment used in this work, the model equations depending on electric field strength are the most feasible solution for implementing the tunable behavior of the ferroelectrics in the paraelectric phase. Moreover, the model equation by Weil et al. is located between the other two model equations, as it allows an improved adaptation to real measured data by using three parameters [Mau11]. Therefore, Weil's model equation is the optimum choice for this work for modeling tunability, and its implementation is discussed in Chapter 4.

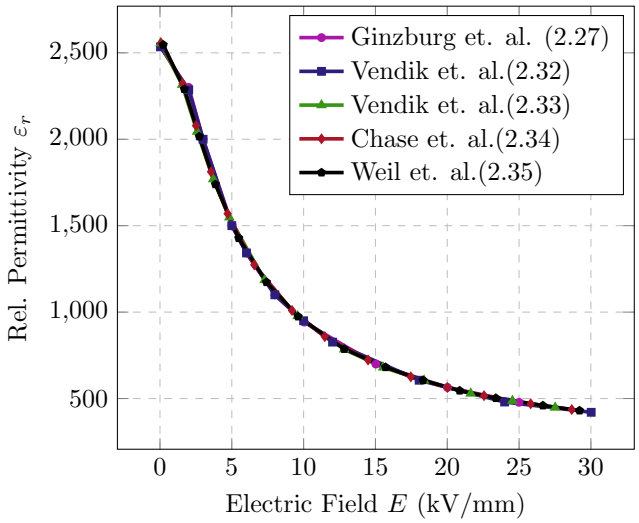

Figure 2.10.: Comparison between different tunability equation models discussed in this work for a BST perovskite in the non-polar phase.

Table 2.1.: Parameter details of various tunability equation models discussed in this work.

Model	Parameters
Ginzburg-Landau	$T_0 = 242.75\,\mathrm{K}$; $\mathrm{C} = 13.4{\cdot}10^4$ K; $\beta = 1.224{\cdot}10^9 \mathrm{Jm}^5/\mathrm{C}^4$
Vendik et al. (2.32)	$\varepsilon_{00} = 609.97$; $\Theta_F = 175\,\mathrm{K}$; $E_N = 27.72\,\mathrm{kV/mm}$; $\xi_S = 0$
Vendik et al. (2.33)	$\varepsilon_r(T) = 2564.6$
Chase et al. (2.34)	$\varepsilon_{r,max} = 2564.6$; $E_2 = 6.43\,\mathrm{kV/mm}$
Weil et al. (2.36)	$a_1 = 3.155$; $a_2 = 14.877$; $E_a = 15\,\mathrm{kV/mm}$; $\tau_{E_a} = 72.9\%$

2.4. Piezoelectricity and Electrostriction

Principally, all crystals suffer through structural changes or strain when exposed to external stress, and this change is depicted in the form of a change of lattice constant or length. The stress is of different types [Gev09]:

- Temperature, which leads to thermal expansion of materials;
- Mechanical, which is responsible for elastic deformation of the crystal structure;
- External bias fields lead to piezoelectric and electrostrictive electromechanical effects that degrade or enhance the overall electric behavior, depending on the application environment.

Due to the nature of the electrical application of this work, the focus is on gaining insights into piezoelectric and electrostrictive effects. Although, these effects are interdependent on temperature and elastic impact as well.

In general, electrostriction is possessed by all crystals, irrespective of being ferroelectric or non-ferroelectrics. This effect is characterized by the crystal's ions changing their sizes or positions under the influence of an external electric field. In one dimensional case, the electric field induced relative change in crystal length or strain S is related to the electric field quadratically [Gev09]:

$$S = \frac{l(E) - l(0)}{l(0)} = gE^2, \tag{2.37}$$

where g is the electrostrictive coefficient, $l(0)$ and $l(E)$ are the lattice constants at electric field being zero and E, respectively. The quadratic nature leads to the strain being independent of the polarity of the electric fields applied, which makes the magnitude a sole deciding factor. Similarly, the piezoelectric effects are observed with a certain class of ferroelectrics. This effect is witnessed prominently in the polar phase and in small amounts in the paraelectric phase as well. The strain associated with the piezoelectric effect is given by [Gev09]:

$$S = \frac{l(E) - l(0)}{l(0)} = dE, \tag{2.38}$$

where d is the piezoelectric coefficient, and this strain S depends on the polarity of the applied electric field, i.e., the strain changes sign (negative or positive) depending upon the direction of the applied electric field. Additionally, this effect is generated by applying mechanical pressure on the opposite surface of the crystal. This loss of electrical energy to mechanical energy makes the design of low-loss varactors important to improve the loss performance.

These electrostrictive and piezoelectric effects are advantageous in various electromechanical devices such as transducers [Sza+21], bulk-acoustic wave resonators or filters [Cha+19]. However, this work focuses on reducing their effects on electrical loss characteristics due to the low-loss application demands.

Mathematical Analysis of Electrical and Mechanical Coupling

The aforementioned properties of the ferroelectric, such as permittivity, polarization, the elastic coefficients g, d, etc., are interdependent on the stresses mentioned above, i.e., temperature, external electric fields, and mechanical strain. This leads to strong coupling of these strains and is represented in a simple mathematical form as follows:

$$S = sT + (d + gE)E, \tag{2.39}$$

$$D = \varepsilon_0 \varepsilon_r E + dT, \tag{2.40}$$

where S is the strain, $T(N/m^2)$ is the stress, $D(C/m^2)$ is the electrical displacement, $E(V/m)$ is the electric field. Whereas, $s(m^2/N)$, $g(m^2/V^2)$ and $d(m/V)$ are the elastic (or acoustic) compliance, electrostrictive and piezoelectric coefficients, respectively, at constant electric field and temperature.

In a real scenario of this work, a metal-insulator-metal (MIM) approach is employed to explore the properties of low-loss varactors. The strong bias electric fields are in the longitudinal direction. Due to this, the prominent electromechanical coupling happens along the out-of-plane axis, i.e., along the 33-axis. The corresponding axis notations are portrayed in Figure 2.11. Hence, the updated electromechanical equations are given by [New05; Gev09]:

$$D_3 = \varepsilon_{33}^T E_3 + d_{33} T_3, \tag{2.41}$$

$$S_3 = d_{33} E_3 + s_{33}^E T_3, \tag{2.42}$$

where D_3 is the out-of-plane electric field displacement and strain S_3 due to applied electric field E_3 and stress T_3. The ε_{33}^T is the dielectric permittivity at a constant temperature, s_{33}^E is the elastic or acoustic compliance under a constant electric field, and d_{33} is the piezoelectric coefficient along 33-axes. In the other representation, the relation is stated as follows:

$$S_3 = s_{33}^D E_3 + g_{33} D_3, \tag{2.43}$$

$$E_3 = -g_{33} T_3 + \beta_{33}^T D_3, \tag{2.44}$$

with $g_{33} = d_{33}/\varepsilon_{33}$, and $\beta_{33} = 1/\varepsilon_{33}$ is the stiffness or inverse dielectric permittivity. The resultant longitudinal coupling coefficient is stated as follows:

$$k_{33}^2 = \frac{d_{33}^2}{s_{33}^T \varepsilon_{33}^E} = 1 - \frac{s_{33}^D}{s_{33}^E}. \tag{2.45}$$

The k_{33}^2 depicts the fraction of electromechanical energy interchangeable between electrical and mechanical energy.

Acoustic Resonance Analysis of Electrical Devices

As discussed previously, in a piezoelectric material, the coupling between electrical and mechanical parameters leads to the origin of the acoustic activity. The applied electrical field induces mechanical strain in the material due to the piezoelectric effect (ferroelectric phase) or electrostrictive effect (paraelectric phase). This excited acoustic activity induces an electromagnetic wave that superimposes the electric field

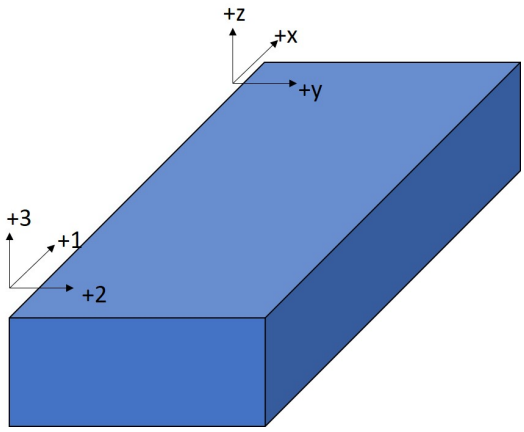

Figure 2.11.: Ferroelectric material and its directional axis notations.

response. In a paraelectric phase of a ferroelectric solid, the acoustic wave equation is derived from Newton's second law, which is given as [NSS17; New05; Kie19]:

$$\rho \frac{\partial^2 r}{\partial t^2} = c^{(m)} \Delta \varepsilon^{(m)} - g \Delta E, \tag{2.46}$$

where r is the displacement of a particle in direction x, y, z or 1, 2, 3, as displayed in Figure 2.11, whereas ρ, g and $c^{(m)}$ are the density, piezoelectric coefficient and Young's modulus of the ferroelectric material, respectively. Neglecting the detailed explanation, the propagation or phase velocity depending on the mechanical properties of the ferroelectric material, which is described as [New05; Kie19; TM12]:

$$\nu_p = \sqrt{\frac{c^{(m)}}{\rho}} = \frac{\omega}{k}, \tag{2.47}$$

where ω and k are the angular frequency and wave number of the acoustic resonance phenomena, respectively. Concerning layered structures such as parallel plate capacitors, each boundary between different material layers causes acoustic wave scattering. Therefore, multiple resonances and their harmonics are obtained for these layered structures.

As discussed earlier, the acoustic excitation in a ferroelectric material results in interference in the electromagnetic region. This interference is witnessed in the frequency spectrum of the loss tangent as the periodic occurrence of spikes [Kie19]. These spikes are characterized by a standing bulk acoustic wave excited between the electrodes of the parallel plate capacitor. In simple terms, the input electric energy is dissipated in the form of mechanical energy and heat in the ferroelectric layer. The mechanical energy is coupled to adjacent layers, and a significant part is lost due to absorption and radiation into the air. Apart from dielectric loss, these are the leading causes responsible for additional losses in the ferroelectric material, reducing the reliability of the ferroelectric-based devices.

Electric-field Induced Piezoelectricity and Effects on Permittivity

The above discussions have already established that the main acoustic activity is inside the ferroelectric layer in a ferroelectric varactor. The electrostrictive strain mainly contributes to acoustic activity in the paraelectric phase. A parallel-plate varactor with a bulk ferroelectric layer between two thick electrodes is assumed to understand the theory behind the presence of acoustic activity. Besides, due to the consideration of the application in an electric environment, the ferroelectric is in a paraelectric or non-polar phase. Consequently, an electrostrictive strain is induced across the layer with the application of an electric field. According to [Li+14;

New05] and Equation (2.37), this approximate electrostrictive strain is represented as follows:

$$S = GP^2(E), \tag{2.48}$$

where G is the voltage electrostrictive coefficient and $P(E)$ is the polarization due to the electric-field E across the layer. The G is proportional to the g, mentioned in Equation (2.37). For tunable ferroelectrics, the polarization is divided into three components and is illustrated as follows:

$$P(E) = P(E_{DC}) + P(E_{AC}) + P_S, \tag{2.49}$$

where $P(E_{DC})$ and $P(E_{AC})$ are the polarization components due to large bias electric field and RF electric field, respectively, whereas P_S is the spontaneous polarization. To characterize the functional materials, such as BST, a small-signal analysis is performed with a large bias signal E_{DC}, which is a high-voltage DC signal, to tune the ferroelectric layer. The small RF signal ensures the varactor's linear performance by minimizing harmonic effects. Additionally, the ferroelectrics in the non-polar phase have zero spontaneous polarization, theoretically and negligible, practically. Hence, a strong DC bias signal is the main contributor to the polarization $P(E)$, which leads to the following:

$$S = GP^2(E_{DC}). \tag{2.50}$$

Considering polarization $P(E)$, which is represented as:

$$P(E) \propto \varepsilon E_{DC}, \tag{2.51}$$

the strain is expressed as:

$$S \propto G\varepsilon^2 E_{DC}^2. \tag{2.52}$$

Here ε is the permittivity of the ferroelectric layer, and according to [Li+14], the G is related to permittivity as follows:

$$G \propto \frac{1}{\varepsilon}. \tag{2.53}$$

Therefore, the strain S in Equation (2.52) modifies to:

$$S \propto \varepsilon E_{DC}^2, \tag{2.54}$$

which depicts that the strain S is directly dependent on the permittivity of the material, apart from the DC bias fields. Consequently, the lower the permittivity, the more electrostrictive strain is minimized. Simultaneously, this strain S induces the piezoelectric effect, and the associated piezoelectric voltage coefficient D is expressed as:

$$D = \frac{\partial S}{\partial P(E)}, \tag{2.55}$$

and using Equation (2.50) and (2.51), this coefficient modifies to:

$$\begin{aligned} D &= 2GP(E_{DC}), \\ D &\propto 2G\varepsilon E_{DC}. \end{aligned} \tag{2.56}$$

This piezoelectric effect is responsible for an acoustic impact on the small RF signal. This effect, though, is independent of the electric field's polarity due to its quadratic dependence on the electrostrictive strain S.

Physically, the displacement of the Ti^{4+} ions in the BST crystal leads to the above-mentioned strain S upon applying large bias fields. This ionic displacement is proportional to generated mechanical energy. Consequently, the generated mechanical energy generates acoustic waves. A fraction of this energy is reflected back to the ferroelectric layer at interfaces to adjacent layers, creating standing waves or acoustic resonances. Concurrently, due to energy conservation, the acoustic waves decrease the varactor's Q-factor Q_ε or an increase in equivalent series resistance ESR [GVL06]. The created acoustic resonances are spread over a frequency range with harmonic characteristics. In observation, these resonances lead to the equivalent harmonic drops of the Q_ε or spikes in ESR in this frequency range. According to Equation (2.54) and (2.56), a solution is devised, where a small amount of low-dielectric-constant (LDK) material is introduced to the ferroelectric layer to reduce the relative permittivity of the BST layer, with an expected minor decrease in tunability. Hence, this eventually reduces electrostrictive strain and the associated effects of induced piezoelectricity. Consequently, the impact of standing acoustic waves is minimized, resulting in Q_ε and low-loss characteristics elevation of the ferroelectric-based varactors.

2.5. Ferroelectric Composites and Loss Characteristics

Due to tunable behavior, ferroelectric materials have been crucial for reconfigurable microwave devices such as frequency-agile antennas based on tunable phase shifters, adaptive filters, voltage-controlled oscillators, and matching networks [Kie+18a;

Wan+15; Ann+19; Mer+17]. Generally, these frequency-agile devices are based on three types of technology, namely – bulk ceramics, thick-films, and thin-films [Wal21; Kie19]. The main reason for employing ferroelectric materials is the substantial and fast variations of their permittivity ε under the influence of an applied electric field in the non-polar or paraelectric phase. Microwave applications are characterized by high tunability and low losses. These characteristics are correlated, and a trade-off is necessary among these for optimal device performance. Additionally, these material's high permittivity values at microwave frequencies lead to a device design issue in the simulation environment. Thus, mixing tunable ferroelectric materials with low permittivity and low-loss non-tunable dielectric materials has been considered to reduce both, permittivity values and losses. Another approach is to implement engineered porous ceramics achieving a similar objective without unwanted chemical reactions at the ferroelectric-dielectric boundaries. However, the additive approach seems promising due to the complex fabrication processes of reliably controlling structural properties regarding pore configuration and geometry. This forms the basis for selecting an additive method in this work.

Losses in Ferroelectric-based Varactors

The loss in ferroelectric-based varactors is broadly influenced by two major factors, i.e., the dielectric loss due to tunable ferroelectric and the conductor loss of the electrodes. According to [VTZ98], the dielectric loss for BST varactors is described by a superposition of different loss mechanisms. Depending on the fundamental physical parameters such as temperature (T), the operating frequency ($f = \omega/2\pi$), and the relative permittivity of the material (ε_r), lattice vibrations are caused. The loss due to these vibrations is defined as the intrinsic loss, $\tan(\delta_I)$, and is stated as follows:

$$\tan(\delta_I) \propto \omega T^2 \sqrt{\varepsilon_r^3}. \tag{2.57}$$

Furthermore, the influence of a bias voltage shifts the material's symmetry, leading to a loss fraction that is a few orders of magnitude larger than the basic loss [Tag+03]. This loss mechanism is called the electric field strength-dependent Quasi-Debye mechanism (QD). This loss relation is stated as follows:

$$\tan(\delta_D) \propto \omega \tau_\varepsilon(E), \tag{2.58}$$

where $\tau_\varepsilon(E)$ is the dielectric tunability at electric field strength E. Additionally, in the real scenario or for non-ideal materials, extrinsic loss due to material defects must be considered. Mainly, the loss in this category is governed by charge defects of the ferroelectric materials considered in this work. In contrast to the field strength-dependent Quasi-Debye loss, their contribution decreases with increasing electric

field strength. The concentration of the charge defects depends on their accumulated charge Q_D and the defect's concentration n_d as well as the frequency. The relation is stated as follows:

$$\tan(\delta_L) \propto n_d Q_D \varepsilon_r [1 - \tau_\varepsilon(E)] fct(\omega). \tag{2.59}$$

All the loss mechanisms mentioned above collectively contribute to the dielectric loss of the ferroelectric material. Thus, these loss fractions are additively superimposed, with the fractions being equal due to the symmetric shift (QD), and the charge defects exhibit opposite behavior concerning the field strength. The total dielectric loss is represented as follows:

$$\begin{aligned} \tan(\delta_\Sigma) &= \tan(\delta_I) + \tan(\delta_D) + \tan(\delta_L) \\ &= a_I \cdot \omega T^2 \sqrt{\varepsilon_r^3} + a_D \cdot \omega \tau_\varepsilon(E) + a_L \cdot n_d Q_D \varepsilon_r [1 - \tau_\varepsilon(E)] fct(\omega), \end{aligned} \tag{2.60}$$

Where a_I, a_D, and a_L represent the proportionality constants of the individual loss fraction components. Figure 2.12 illustrates the dielectric loss of a BST thick-film varactor compared to the intrinsic loss. Due to the dielectric loss caused by charge and other crystal defects [Men+11], the extrinsic loss in thick films reaches magnitudes more prominent than in an ideal crystal. However, the conductor loss is based on its conductivity and can be avoided using better-conducting materials and more suitable designs to overcome excessive metal usage. Apart from these dielectric

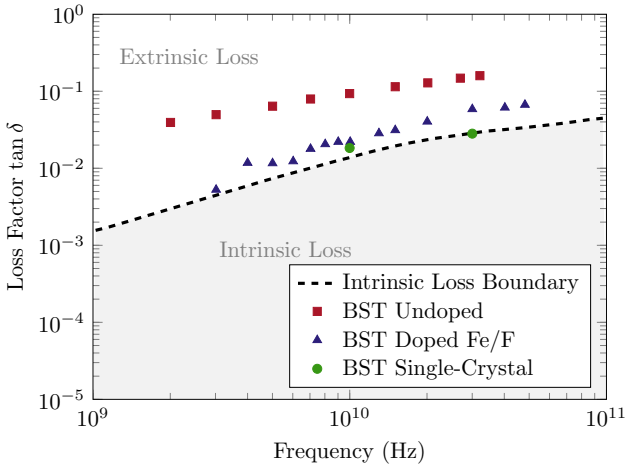

Figure 2.12.: Comparison of loss factors $\tan\delta$ of unbiased BST in the form of thick-films and ideal crystal [Men+11]. A doped thick film (blue triangles) is also compared with the undoped variant (red squares). The least $\tan\delta$ is shown by the ideal crystal, which is reaching the intrinsic boundaries.

and conducting losses, the loss due to induced piezoelectricity contributes to loss as part of stored energy is radiated into the air, as discussed in the previous section. Handling losses due to this induced piezoelectricity is one of the primary focuses of this work, and thus, a ferroelectric composites approach is applied.

Loss Reduction in Ferroelectric Composites

In the past, various additive approaches have been implemented. Initially, the metallic additions are made in the doping concentrations. An example of this is illustrated in Figure 2.12, where a BST thick-film varactor doped with Iron/Flourine (Fe/F). A clear reduction in dielectric loss is witnessed compared with an undoped sample. Other dopant in this category includes—Copper (Cu) [Sta+18], Manganese (Mn) [Nad+15] etc. These metallic dopants reduced dielectric loss in small amounts, which paved the way for low-loss dielectric addition into ferroelectrics. Hence, low permittivity and low dielectric loss simple-oxide dielectric materials such as Magnesium Oxide MgO [SB04], Manganese Oxide MnO [KSK98] came in as additive alternatives. According to [SB04; Hua+15; Zha+10], demonstrates the MgO addition in BST ferroelectrics, where compositions range from doping quantities to mixing quantities. This addition shows reasonable suppression of dielectric loss. Furthermore, complex dielectric oxide with better Q-factor Q_ε are proposed as alternatives to generate even better dielectric loss suppression. These complex oxides include - Magnesium Silicate (Mg_2SiO_4) [Tan+14], Magnesium Titanate (Mg_2TiO_4) [CZY07; Tan+14], Magnesium Borate ($Mg_3B_2O_6$) [ZZY11] etc. The $Mg_3B_2O_6$ (MBO) has extremely high Q_ε (¿2000) and is effective in reducing sinter temperatures [ZZY11] and, thus, is the optimal choice for this work. On the contrary, adding low-loss dielectrics into ferroelectrics also reduces tunability τ_ε, extensively. This trade-off between Q_ε and τ_ε is important for low-loss varactors. Apart from the dielectric loss, the composites also effectively reduce acoustic activity due to induced piezoelectricity in the ferroelectrics under the influence of applied electric fields. Equation (2.56) shows a direct relationship between the permittivity and the induced piezoelectric voltage coefficient D. Thus, the reduced permittivity of the ferroelectric-dielectric composites compared to ferroelectrics is crucial for reducing acoustic activity in context with low-loss varactor applications in this work. In the upcoming chapter, a detailed design in the form of bulk-ceramic varactor implementation is discussed, with succeeding chapters discussing tunability modeling and suppression of induced-piezoelectricity or acoustic behavior.

3. Bulk-Ceramic Composite Varactors

Cylindrical disks or cuboids of ferroelectric single crystals and ceramics can be used in tunable devices [Poz04]. The linear dimensions of these devices and their mass are proportional to the length of the electromagnetic wave propagating in the ferroelectric medium, which is related to the dielectric permittivity of the material as:

$$l = \frac{c}{f_o \cdot \sqrt{\varepsilon}} \tag{3.1}$$

where $c = 3 \times 10^8$ m/s is the approximate speed of light in vacuum, and f_0 and l are the frequency and length of the electromagnetic wave inside a ferroelectric medium, respectively. The expected change in dimensions by using a ferroelectric material is proportional to $\sqrt{\varepsilon}$. These elements are used at the radio frequencies (RF) as parallel plate tunable capacitors or varactors. Presently, a high loss of ferroelectrics (compared to that of semiconductor varactors at radio frequencies) and high bias voltage requirements for tuning limit the use of this kind of bulk varactors compared to the semiconductor ones.

Bulk-ceramic disk varactors present an alternative to thick-film and thin-film technology. These varactors are employed in the printed circuit boards to form a circuit board integrated bulk ceramic disk varactor module. This module includes a DC biasing network for tuning and is used for matching the RF source and receiver. These disk varactors can be arranged in series or parallel according to the size limitations or capacity requirements specifications. Hence, this work focuses prominently on characterizing these varactor pellets based on extracted parameters Q-factor, tunability, equivalent series resistance, etc. The various aspects, such as material compositions, additives, processing techniques, and thermal and electric properties of varactor pellets, are explored. Consequently, base material and its compositions with various metallizations and processing routines are implemented. The electrical characterization is done in the frequency range of 10-25 MHz with RF small-signal and a large DC bias. The choice of metalization depends solely on RoHS compatibility, adhesion to the BST surface, compatible PCB integration processes, and, most important, high conductivity. This work explores silver and copper as metals for electrodes.

3.1. Design and Optimization

The first significant challenge in the design and manufacturing of bulk ceramic disk varactor is the choice of shape and size, which are essential for mechanical and electrical stability. Considering this, the cylindrical body is chosen for the implementation. Mechanically, it is easier to distribute homogeneous compression pressure throughout the surface area of the varactor in comparison to a cornered geometry. Regarding electrical performance, the round body ensures homogeneous distribution of stray electric fields, which provides homogeneous field loading. However, to maintain a specific diameter, a minimum required thickness has to be maintained for mechanical stability, which lies around 0.6 mm. Thus, a thickness less than 0.6 mm is not feasible with manufacturing processes. In addition, due to the focus on the high power matching circuits, the high untuned or unbiased relative permittivity is beneficial, achieved with a much-increased thickness of the varactor.

Furthermore, the increased thickness of bulk-ceramic pellets compared to other technologies based on thick and thin films introduces new challenges. Due to increased thickness, the bulk ceramics exhibit significantly larger permittivities than other technologies (see Figure 2.6). Additionally, bulk ceramic's maximum DC biasing voltages are significantly high and reach the electrical field strength in the kV/mm magnitude range inside the material. Thus, a large DC bias voltage maintains equivalent tuning or biasing electric fields to achieve maximum tunability. In this work, the maximum voltages up to 1.1 kV are used to demonstrate the small-signal electrical characterization owing to the laboratory safety requirements. However, the varactors are intended for use with biasing voltages up to 6 kV in the application environment. Hence, due to technical restrictions of the measurement circuit and safety, the thickness is intended to be under the conditions to avoid the breakdown of the varactor.

Additionally, increasing or decreasing capacitance switching is desired to be rapid and continuous with the change in bias voltages for the varactor in the presented application in high-power matching circuits to compete with the current trends. A bulk ceramic ferroelectric varactor provides an exciting alternative. However, such varactors deal with massive electric field displacement. This leads to higher stresses over the adjacent materials. With the parallel plate capacitor topology implemented, having air in its surroundings and low electrical conductivity in the dielectric, the electric field distribution is mainly confined within the dielectric. Hence, stray field components in the adjacent material are present. However, they are significantly lower than in the dielectric.

Despite this, the field distribution in the transient case is determined by the permittivity contrasts between adjacent materials rather than their respective conductivities [Kie19]. In consequence, there is a significant displacement of electric fields into the low permittivity surrounding air. It is explained with the help of fundamental Ampere-Maxwell law, which is as follows [JS08a; Kie19]:

$$\nabla \times \mathbf{B} = \mu_0 \Big(\mathbf{J} + \varepsilon_0 \varepsilon_r \frac{\partial \mathbf{E}}{\partial t} \Big). \tag{3.2}$$

The second term denotes the displacement current density and generates a magnetic field similar to the magnetic field by the actual current. However, moving charges contribute to the actual current rather than the displacement current. It represents a time-varying electric field or rate of change of electric fields. In dielectric materials, this displacement current results from slight displacement of stored charges, also known as dielectric polarization. This displacement current dominates the total current for the materials with large permittivities. Hence, the displaced electric fields from this displacement current are usually higher in the ferroelectric-based bulk-ceramic varactors intended for use. Before going into detail about the stray fields in these varactors, their specific design parameters are discussed.

Specific Design Details

The bulk ceramic disk varactors intended for PCB applications have a diameter of 16 mm and thicknesses ranging from 0.6 mm to 1 mm to satisfy the capacitance load requirements. This study characterizes these varactors for capacitance tunability and acoustic behavior. The acoustic behavior predominantly depends on the varactor's thickness, whereas the capacitance depends on both the metalized surface area and the thickness of the varactor. However, the capacitance tunability is determined by bias voltages. It is indirectly related to the thickness of the varactor, as it depends on a strong bias electric field, which is associated with both bias voltages and thickness. Figure 3.1a shows the designed varactor in this work, which is in the shape of a cylindrical disk. This design is based on the parallel-plate capacitor topology to extract maximum tunability in this topology. The bias electric field is confined inside the high permittivity ferroelectric layer between the two electrode layers. The other topologies, which include the interdigital capacitor (IDC) and other gap capacitors, tend to lose a considerable amount of bias electric fields in adjacent material layers, which reduces the tunability as a consequence [Mau+10]. Although, gap-based capacitors are crucial for planar applications, which are essential for most mobile devices. As the focus is on characterizing ferroelectric material in this work, the parallel-plate capacitor topology is the most suitable among all topologies. The electrodes in the designed varactors, though, are smaller in diameter than the ferroelectric material diameter to counter the high-voltage electric field discharges at the edges of the varactor. Additionally, the difference in diameters of the top and bottom electrodes ensures fabrication misalignment.

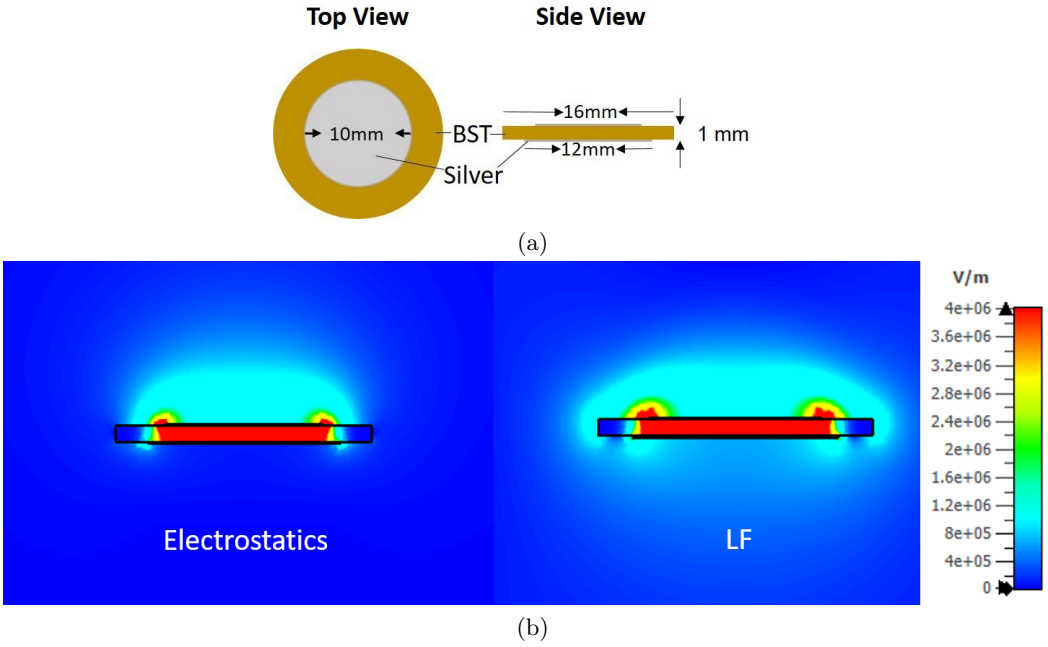

Figure 3.1.: Varactor designed in this work with its dimensions in (a), whereas (b) shows the comparison of Electrostatic and LF solver. Displaced electric fields are increased due to time-varying fields at the trijunction of high permittivity ferroelectric, low permittivity air, and the top electrode.

Field Analysis

The varactor in the stated geometry is simulated to get the expected capacitance values through frequency domain simulation in CST Studio Suite. The BST material's permittivity is around 2000, close to the values found in the real scenario [Wie+17]. The electrodes are perfect electric conducting (PEC) type. Ultimately, a discrete port is used to extract the capacitance from the capacitor model. The capacitance obtained is in the range of around 1.7 nF for a thickness of 1 mm. Moreover, in the actual scenario, the material is not uniform and has a lot of defects like air gaps or pores and metallic impurities, which reduce the capacitance values drastically. Another reason can be the difference in thickness of the varactor, which could increase the capacitance if thickness decreases slightly and vice versa. The thickness of the varactor can vary due to fabrication limitations such as different pressure while pellet formation or misappropriate volume of ferroelectric or dielectric powders. However, it is still expected that the capacitance is above 1 nF. The analysis is prominently done considering the BST-based varactor. However, due to these varactors' high dielectric losses, the resultant varactors' Q-factor is relatively low, around 100, in the intended frequency range of 10-25 MHz. Additionally, Electrostatic and LF-Solver detect the effects of time-varying fields with only DC and mixed signals

(DC and 10 MHz), respectively. The cylindrical disk shape prevents the concentration of bias fields and time-varying stray fields at a particular region inside the varactor material. This is visualized in Figure 3.1b, where acute radiation leakage effects are detected at the junction of the electrode, ferroelectric and air boundaries, reducing the varactor performance. An increase in radiation leakage is present with the mixed signals case due to additional RF signals. In the application environment, the effects are increased many-folds due to high power RF signal of around 1 kW. Thus, small RF signals characterize the material to minimize these radiation leakage effects. The round body of these varactors prevents radiation leakage by distributing the electric fields uniformly in all directions. Furthermore, these varactors achieve high capacitance values due to higher bounded electric fields. Though, a large RF signal analysis is performed in [Kie19] for such varactors.

Moreover, apart from dielectric losses, the acoustic activity further decreases the Q-factor, which is explained in Chapter 5. Hence, the BST is a mixed low-loss dielectric material capable of reducing dielectric losses and acoustic activity. Consequently, in the same varactor design, the relative permittivity is changed to a minimum of around 500 to imitate the effects of ferroelectric-dielectric composites and keep other parameters the same as in the earlier simulation. The capacitance for the composite came out to be around 0.62 nF. Later, a correct modeling approach is discussed in Chapter 4 and 5, and measured values of actual composite structures are compared and analyzed.

3.2. Fabrication and Processing

The crucial initial step in fabricating the bulk-ceramic varactor is the synthesis of correct BST stoichiometry. In this direction, the sol-gel method is presented [Pau06] is presented, which is used for producing the two BST stoichiometries, namely –$Ba_{0.6}Sr_{0.4}TiO_3$, and $Ba_{0.7}Sr_{0.3}TiO_3$. Different BST stoichiometry is based on the environmental conditions of the intended applications. If the application is under hot environmental conditions, higher Barium content BST is considered to achieve higher tunability while maintaining around 15-20 °C difference between measuring temperature and Curie temperature to keep centrosymmetry [Jeo04]. However, the primary benefit of the sol-gel method is the capability of more accessible addition of doping elements and other materials, which are used to modify the dielectric properties of the BST [Pau06; Zho12]. In addition, this method provides a scalable process for obtaining desired volume compositions.

Using the sol-gel method [Pau06; Zho12; Gev09; Häu+21], the basic materials, namely–barium acetate, strontium acetate, and titanium isopropoxide, are thoroughly mixed in aqueous conditions. Figure 3.3 depicts the fabrication process flow followed. The acetates are initially dissolved in acetic acid overnight, which is then added by titanium isopropoxide in the aqueous conditions. The thoroughly mixed

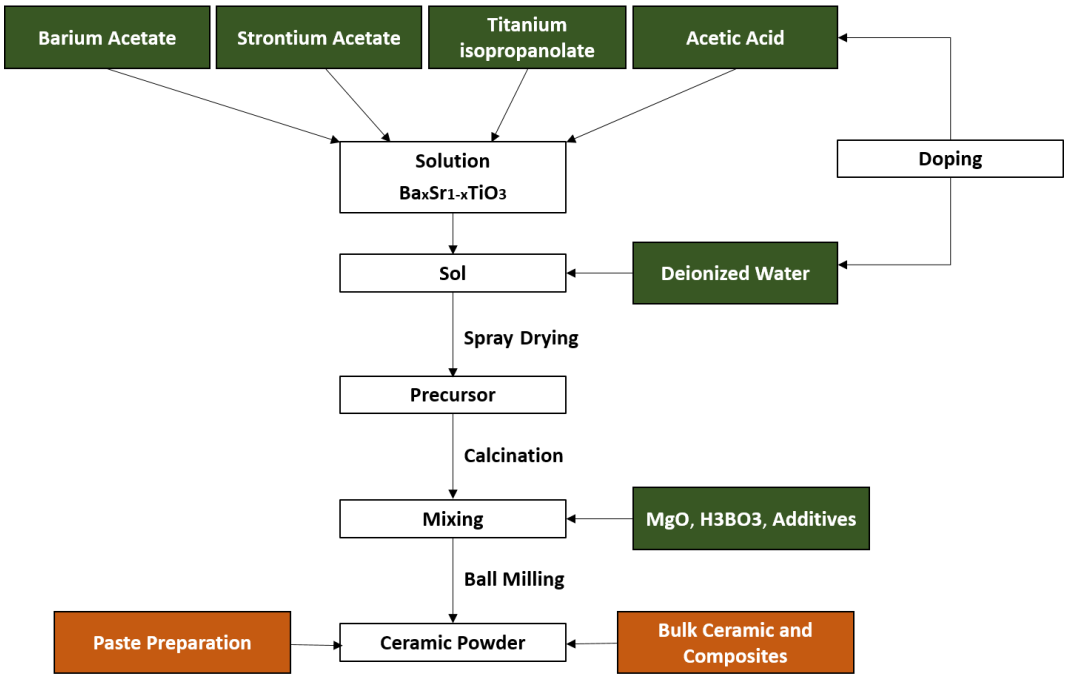

Figure 3.2.: Fabrication and processing of ceramic powder, which is then used to produce bulk ceramic varactors. Alternatively, in the paste form, it is used to produce planar varactors.

sol is then calcined at 1100 °C for 2 hours to promote the oxidation process. The prepared BST is then dried and milled to desired particle size to increase sinter activity. The MBO is prepared by the mixed-oxide scheme using MgO and B_2O_3 in specific stoichiometric amounts. The powders are then milled and homogenized for 4 hours in a planetary ball mill with water as the dispersion agent and zirconia milling balls. After separation of the suspension and the milling balls, the MBO is then dried and calcined at 1200 °C for 2 hours. The prepared mixtures of both mate-

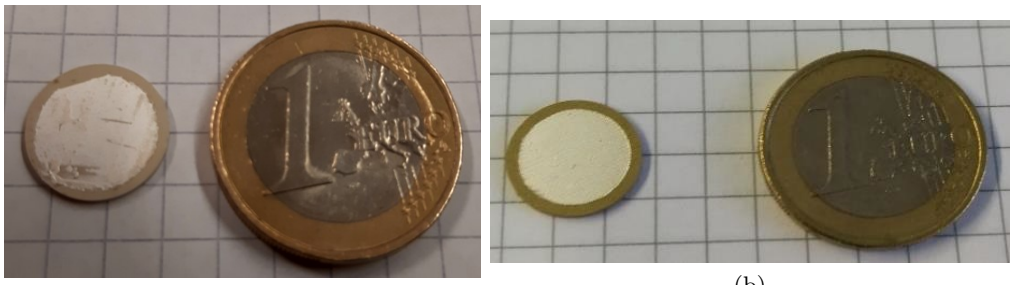

(a) (b)

Figure 3.3.: Realized varactor with (a,b) representing characteristic visuals of $Ba_{0.6}Sr_{0.4}TiO_4$ and $Ba_{0.7}Sr_{0.3}TiO_3$, respectively.

rials are mixed, considering the required volumetric ratios, in the ball mill with the same conditions taken for the MBO synthesis. The sludge of the resultant mixture is then spray-granulated to promote better pressing. The pellets from this mixture are made by pressing using a single-axis press at 150 MPa pressure. The pressed pellet is then densified during sintering, where the maximum sinter temperature is around 1200 °C for the composite varactor and 1400 °C for the 100 vol-% BST varactor. Table 3.1 demonstrates the different BST-MBO composite varactors, ranging from 10 to 100 vol-% BST for the $Ba_{0.6}Sr_{0.4}TiO_4$ stoichiometry, considered in this work. Apart from the volumetric compositions of BST and MBO, the different stoichiometry of BST and different forms of MBO are tried. The BST stoichiometries presented in this work are - $Ba_{0.6}Sr_{0.4}TiO_4$ and $Ba_{0.7}Sr_{0.3}TiO_3$ based on their application temperature. The extensive details about their application and characterization are discussed in Chapters 4 and 5. Moreover, the decrease in sinter temperatures of the composite pellets from the 100 vol-% BST pellet demonstrates another benefit of using BST-MBO composites. Finally, the sintered pellets are metalized for electrical and temperature characterization. The resultant pellets are portrayed in Figure 3.3, and the dimensions are depicted in Figure 3.1a. Concerning metalization, various options, such as silver, copper, and gold, are explored according to their adequacy for high-power RF applications. However, silver is chosen due to its better conductivity and cost-effectiveness. Although, the copper electrodes is a better option for long-term oxidation. The metalization is either applied by hand, using a brush and a stencil, or by galvanically on a printed seed layer or by the screen-printing method. Primarily, the latter form of screen-printing is used for the fabricated varactors. The metalized surface of the disk varactors is around 12 mm and 10 mm, leaving around 2-3 mm unmetalized surface at the edges of the pellets. As discussed already, this reduced diameter of the electrode compared to the diameter of the pellet is

Table 3.1.: Dielectric properties of the BST $Ba_{0.6}Sr_{0.4}TiO_3$ composite materials at room temperature (around 24 °C) at 13.56 MHz. The measured (Meas.) tunability is measured at 1.1 kV bias voltage. The lowered sintering temperatures and reduced dielectric loss in the mixtures of MBO and BST are the main benefits of the BST-MBO composite varactors. The notable degradation in tunablities is also observed.

BST-MBO(in vol-%)	Sinter temperature(°C)	Meas. Q_ε	Meas. τ_ε(%)
100-0	1350	136	41.2
80-20	1050	205	7.8
70-30	1000	220	6
60-40	1000	286	5.9
50-50	1000	310	5.72
40-60	1000	340	4.75
30-70	1050	418	1.6
20-80	1100	850	0.72
10-90	1100	2714	0.025

advantageous. As the intended application deals with high-power signals, the surface discharges are reduced due to increased creepage distance along the edge of the pellet. In addition, electric stray fields in the adjacent air around the pellet are reduced and prevent short circuits due to fabrication misalignment along the pellet edge. And the different electrode dimensions suppress fluctuating capacitance values due to misaligned issues at the surface of the varactor. The smaller electrode usually ensures minimum capacitance values. The upcoming sections discuss a detailed electrical and thermal characterization of these varactors.

3.3. Small-Signal RF Characterization

The RF characterization of a ferroelectric material is performed primarily using the following broad methods, namely–direct measurements, reflection type measurements, resonance methods, and waveguide or transmission-line type measurements. The transmission-line type method is suitable for planar devices and, hence, not considered in this work [Koz+95]. The waveguide type method is similar to the transmission-line type, where a ferroelectric material is placed inside the cavity to extract the scattering matrix followed by the calculation of dielectric permittivity

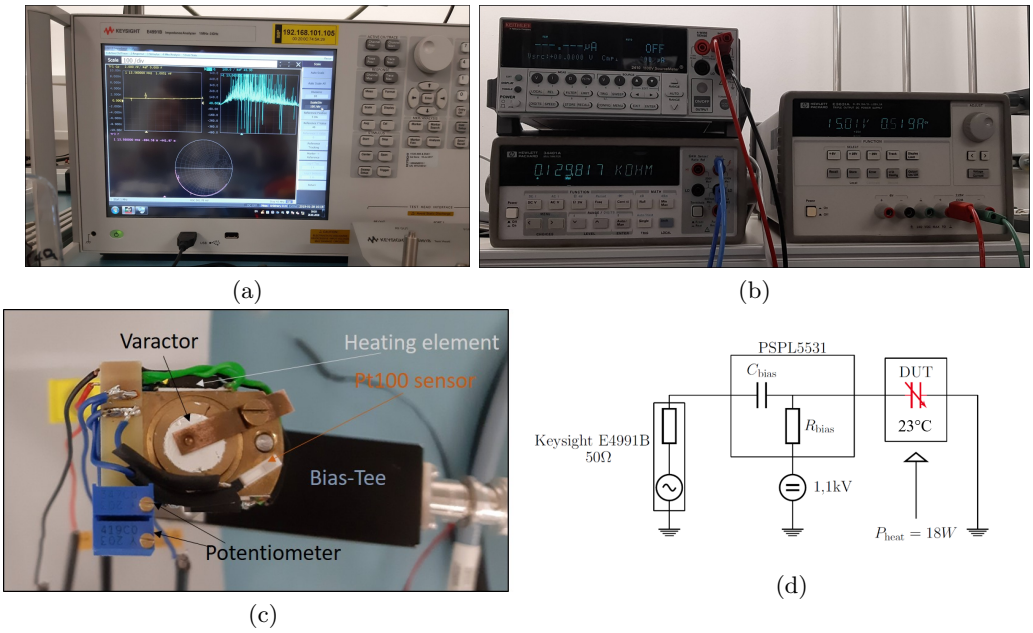

Figure 3.4.: Electrical characterization measurement setup with (a) showing Impedance Analyzer to extract measured indicators. (b) depicting other devices, which includes 1100 V DC Voltage source, Multimeter and 15 V constant-voltage source for the temperature-control element. Whereas (c) illustrates the varactor holder and (d) displays the measurement setup schematic.

[SFW63]. Both of these methods are extended to the resonance method, where a shift in resonance frequency (Δf_o) is investigated to extract the dielectric parameters, as mentioned in [Dub99; HC60]. The rest of the methods are more popular for ferroelectric material characterization. The reflection type usually measures S-parameters and extracts the capacitance from them, which introduces parasitic effects due to 50 Ω matching requirements [Tag+03; AGK15]. Moreover, the direct measurement is based on current and voltage measurements. Hence, no matching is required, leading to fewer instrumental and correction errors, and it is preferred for ferroelectric or dielectric material characterization. The direct measurements are extracted by using an impedance analyzer.

A small-signal RF characterization based on the direct measurement method is performed in this work. This in-house setup uses a small RF signal and a large DC signal to characterize ferroelectric material. A small RF signal reduces nonlinearity, and a large DC bias tunes the ferroelectric material to desired capacitances. In this work, the small-signal characterization fixture, as shown in Figure 3.4, can measure one device at a time. The device or varactor is held by spring-loaded contacts connecting to the metalization on both sides of the pellet. The geometry of these contacts has less impact on extracted electrical data due to the design of the fixture contacts. The fixture is based on the APC-7 type coaxial RF standard connector. A spring-loaded inner connector of the fixture in the center connects the pellet to the smaller electrode. The pellet's larger electrode side touches the fixture's grounded metallic housing through a fixed metal flap. The spring-loaded connector and metal flap stabilize the varactor's position and prevent the loose connection by precise screw tightening. A temperature-controlling module is also placed on the metallic housing to heat the fixture and maintain a fixed temperature inside the pellet to control the environmental temperature. The fixture introduces a parasitic series inductance of 16nH and is being handled in evaluating the varactor characterization data. The fixture is depicted in Figure 3.4c.

The temperature-control unit on the housing has the capability of maintaining temperatures ranging from around 24 °C to 80 °C at the fixture, which roughly transfers the maximum temperatures of 65-70 °C inside the pellets. The difference is due to the free distance degradation in temperature between the housing and the pellet. The unit consists of two DAWN DN505 9W self-regulating subminiature heating elements and a PT100 thermal resistor for precise temperature measurement with an accuracy of ± 0.7 °C at 50 °C. The heating elements contain a control circuit to regulate the input current. This change in current is manipulated by variable resistors ranging between 0.7 kΩ and 200 kΩ, and this resistance is directly related to the set temperature. The key benefit of these variable resistors is the compensation for small temperature fluctuations during the measurement. Moreover, the Pt100 resistor constantly keeps track of the temperature, which is recorded to allow for larger temperature fluctuations. The holder is heated in this process, and most heat is passed to the pellet along the unmetalized region. However, due to the free space

between the pellet and the fixture, a temperature difference of 7 °C is observed when the fixture is heated to 57 °C.

Due to the bulk-ceramic BST compositions chosen for the application in this work, the operational temperature ranges between 24 °C and 70 °C. Depending upon the application conditions, the mixing ratio of barium to strontium decides the operating temperature to maintain the minimum optimal difference from Curie temperature. Hence, $Ba_{0.6}Sr_{0.6}TiO_4$ composites are measured at around 24 °C and $Ba_{0.7}Sr_{0.3}TiO_4$ composites at around 50 °C, maintaining close to 20 °C difference with respective Curie temperatures. Apart from the application environmental conditions, the adjustments in the model in Chapter 4 require mitigating Curie temperature shifts. Hence, a series of additional measurements between 30 °C and 70 °C are made to include these Curie temperature shifts in the electromagnetic simulation environment.

The fixture is then mounted on a calibrated measurement setup. The setup includes the impedance analyzer Keysight E4991B as the primary RF monitoring device. The impedance analyzer is connected directly with a modified Tektronix PSPL5531 bias-tee [Kie19], which isolates the RF signals and high-voltage DC signals. The high-voltage DC signals of up to 1.1 kV are provided with the Keithley 2410 sourcemeter to tune the pellets. This high-voltage DC signal produces about 1.1 kV/mm of electric field strength for the pellets with a thickness of around 1 mm. In a nutshell, the impedance analyzer monitors the extracted capacitance and Q-factor over biasing voltages from 0 V up to 1100 V with 100 V step size and at the set temperature in between 24 °C and 70 °C. In Figure 3.4b, a multimeter HP 34401A and a DC source HP E3631A are also present, which are used to measure the Pt100 resistor and leakage currents, and provide a constant-voltage signal to power heating elements, respectively.

After measuring the different composite varactors for BST $Ba_{0.6}Sr_{0.4}TiO_3$, the varactors are characterized by the extracted Q-factor Q_ε and capacitance tunability τ_C, illustrated in Table 3.1. Later, in Chapter 4, these characteristics are discussed in detail and implemented in the tunability modeling. Additionally, the BST $Ba_{0.7}Sr_{0.3}TiO_3$ composite varactors are addressed in Chapter 5 to explore the acoustic behavior of the BST and its suppression in its composites.

3.4. Thermal Characterization of Capacitance and Shift in Curie Temperature

The behavior of the BST composite varactors is efficiently described by the Curie temperature (T_C) due to its direct relation with the material changes due to mixing [SB04]. The thermal characterization is primarily done to measure the T_C of the BST composite varactors. Due to the BST stoichiometries used in this work,

the T_C is expected to fall below 0 °C, which is out of the scope of the present RF characterization measurement setup. Consequently, an in-house measurement setup for recording such T_C is constructed, independent of this work's chosen radio frequency, i.e., around 13.56 MHz. This is due to the T_C remaining constant throughout any frequency range for a particular BST stoichiometric composites. The constructed setup for these measurements is portrayed in Figure 3.5, with top view, side view, and schematic circuit of the thermal characterization setup depicted in Figure 3.5a, 3.5b and 3.5d, respectively. The capacitance readings are recorded using an Agilent E4980A LCR meter at 1 MHz. The probes connect the LCR meter to a metal head and a metal base to maintain a continuous connection to the

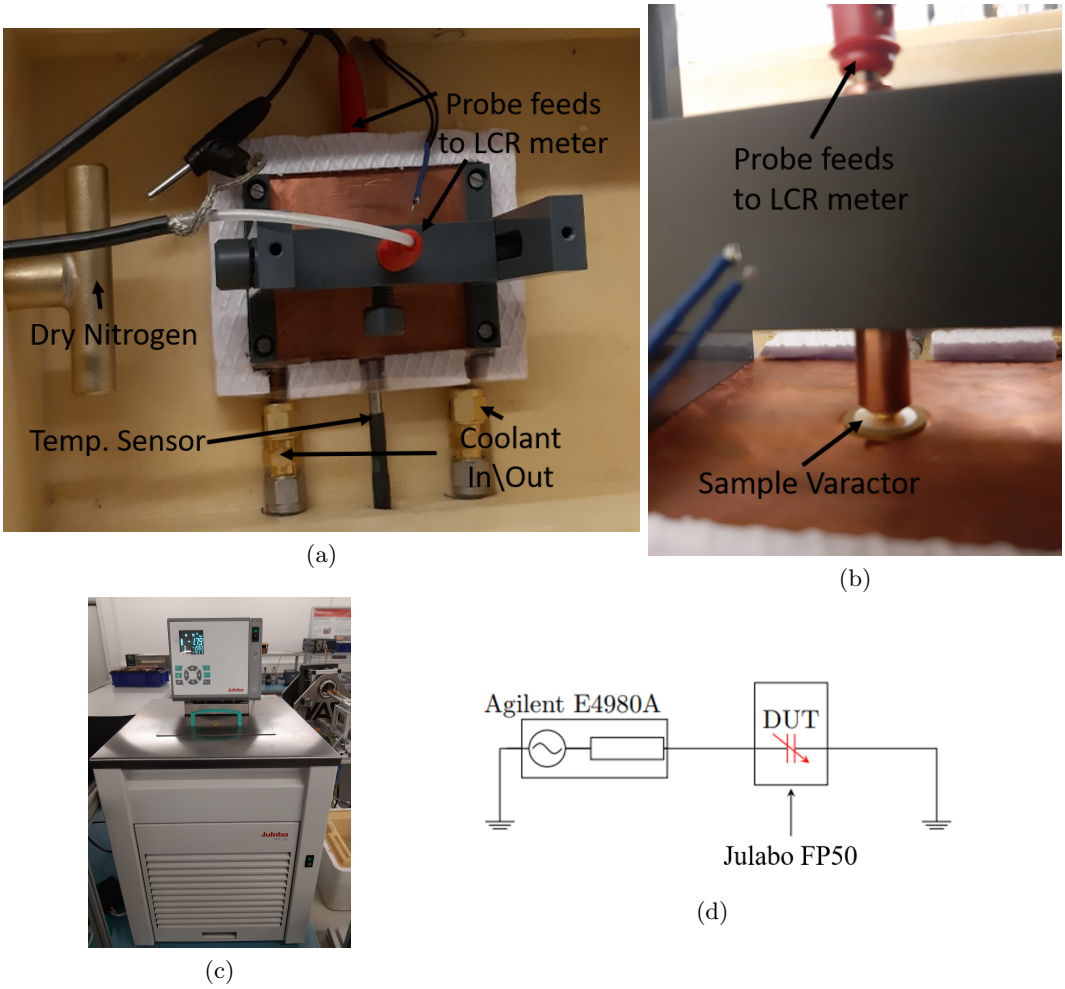

Figure 3.5.: Curie temperature T_C measurement setup with (a,b) depicting the top and side view of the varactor framework and (c) is the cooling unit, capable of maintaining minimum temperatures of −30 °C at the varactor in the present capacity. Additionally, (d) displays the measurement setup schematic diagram.

varactor pellet. The metal head has a spring-loaded contact to maintain a constant electrical connection with the varactor pellet. A temperature-controlled liquid from the Julabo FP50 cooling unit, displayed in Figure 3.5c, is made to flow in the metal base over which the varactor is placed, and thus, the varactor is cooled down to desired temperatures. The temperature close to the varactor is measured by a Pt100 temperature sensor, which is taken as feedback to control the temperature of the liquid coming out of the cooling unit. This process is repeated until the desired set temperature is achieved. Here, the pipes carrying the cooling liquid are thermally insulated by placing a PVC Nitrile Sponge RC02109 covering them, an excellent thermal insulator [Com]. This insulation reduces the difference from around 15 °C to around 4 °C between the temperature of liquid from the cooling unit and the temperature achieved at the pellet, for the set temperature of around −20 °C. After reaching the desired temperature, the capacitance measurements are extracted. In addition, dry nitrogen is made to flow in the vicinity of the varactor to prevent the frosting and defrosting effects due to temperature variations. The temperature at which the highest capacitance is achieved is the T_C of that varactor. Moreover, due

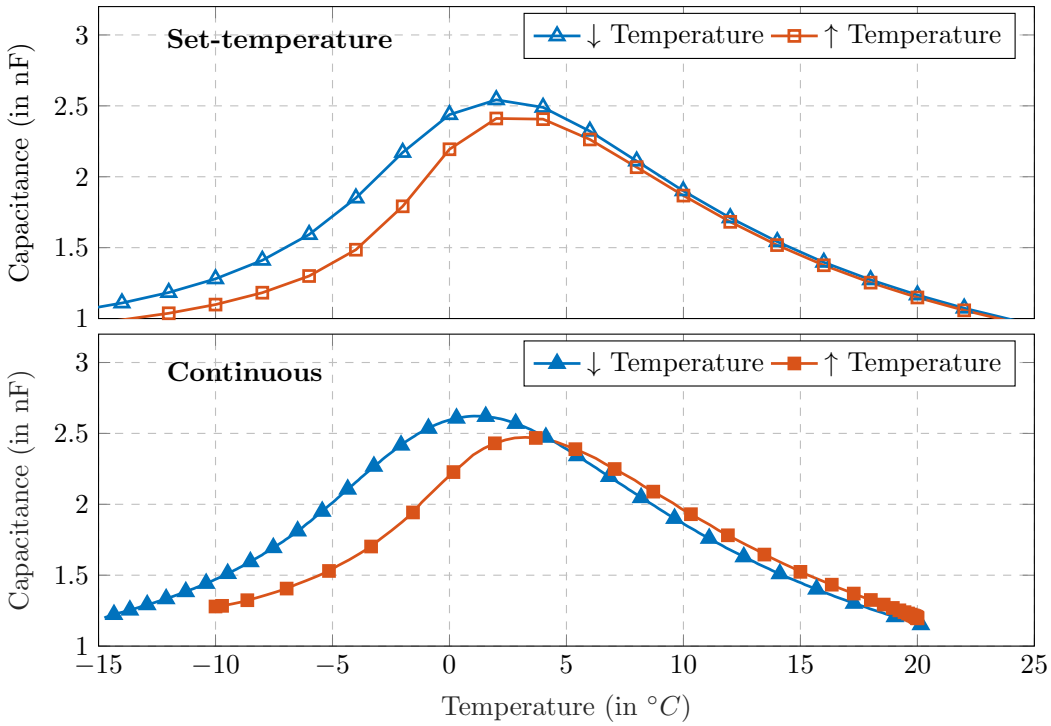

Figure 3.6.: Curie temperature T_C measurement techniques, namely – continuous and set-temperature comparison with increasing and decreasing temperature. Here, 100 vol-% BST $Ba_{0.6}Sr_{0.4}TiO_3$ pellet is used and the T_C is recorded around 2.5 °C and 3 °C from the set-temperature and continuous techniques, respectively.

to the liquid composition being a 1:1 mixture of water and glycol, the minimum temperatures achieved are around −35 °C out of the cooling unit and around −30 °C at the pellet.

The readings are taken in two formats – continuous and set-temperature capacitance measurement. Figure 3.6 compares the two measurement techniques. The set-temperature technique measures the capacitance after setting a series of temperatures on the cooling unit to the desired temperature. For example, a pellet is set at equidistant series of temperatures from 20 °C to −20 °C, with a common difference of 2 °C between the adjacent set temperatures. This technique prevents residual polarization effects, if any, due to enough time for each set temperature to settle capacitance values. Each set temperature is given around 15-30 min of time to settle the capacitance values, with lower temperatures requiring longer. Moreover, the resultant readings still show a slight residual polarization inside the varactor pellets. A little difference in the shape and values of extracted capacitance relation is observed compared with the literature readings. This is suspected due to slight thermal or humidity variations in the nearby environment. In addition, it takes around 8-10 hours to one varactor pellet, which leads to a significant amount of resource usage. Hence, the viability of this method is unsatisfactory, and a more reactive continuous measurement technique is examined. The continuous process involves setting the final desired temperature as the set temperature to the cooling unit directly and taking the capacitance readings continuously until the moment the set temperature or final desired temperature is achieved. However, the readings are not given sufficient time to settle the capacitance, which leads to the inclusion of residual polarization effects in the results. To handle this, the same pellet is measured in the same manner from the set final desired temperature to the initial higher temperature. This measurement shows the reverse stored polarization effect. The average T_C from both measurements is the resultant T_C, which lies close to the literature values. The most important reason which favored this method is the shape of the consequent capacitance readings, which falls in line with the set-temperature technique. This method almost wholly removes the stored polarization effect easily. Additionally, this method takes less than 2 hours for a varactor pellet, significantly reducing resource usage to around 4-5 times less than the set-temperature technique. For example, in Figure 3.6, the set-temperature and continuous processes give 2.5 °C and 3 °C as the T_C, respectively, which is quite near to the literature value of 2 °C. Therefore, for all other pellets, the continuous measurement technique is followed to get the precise temperature readings, and their measured T_C values are illustrated in Table 3.2.

Upon observing the T_C in Table 3.2, a significant reduction in T_C values is noted with MBO content in the composite varactor in comparison with 100 vol-% BST varactor. Moreover, the reduction in T_C increases with the increase in MBO content, and the highest reduction in T_C is noted for 40 vol-% BST $Ba_{0.6}Sr_{0.4}TiO_3$ composite varactor, which is around 32 °C. The T_C reduces from 3 °C to −29 °C. In addition, this reduction is witnessed in the other stoichiometric BST $Ba_{0.7}Sr_{0.3}TiO_3$ composites.

Table 3.2.: Measured Curie temperature T_C and extracted input fitting parameters for updated electrical characterization for different BST-MBO vol-% composite varactors.

BST-MBO(in vol-%)	$T_C(°C)$ for $Ba_{0.6}Sr_{0.4}TiO_3$	$T_C(°C)$ for $Ba_{0.7}Sr_{0.3}TiO_3$ $T_C(°C)$
100-0	3	28
95-5	-	4
90-10	-	0
85-15	-	-3.5
80-20	-20	-1
70-30	-19	-
60-40	-22	-
50-50	-24	-
40-60	-29	-

Due to the range of minimum temperatures reached, only composite varactors with MBO content till 60 vol-% are measured. This reduction in T_C with the addition of dielectric into ferroelectrics has also been witnessed in [SB04], which forms the basis of this whole additional temperature study of the varactor pellets in this work. However, the heavy reduction in T_C is not expected and can significantly change the characteristics of the composites, producing massive tunability deviations between the electromagnetic simulations and extracted measurements. In Chapter 4, these T_C-shifts are studied in detail, using the results from these measurements, and a solution is devised to incorporate these effects in the simulation environment.

4. Modeling Tunability for Composite Varactors

Historically, microwave devices based on engineered ferroelectric composite materials have been investigated experimentally. However, theoretical and simulation modeling has still not been investigated thoroughly. For better device design in the simulation environment, a detailed model of these material's behavior is required. It is to be noted that this work is adapted from the work presented in [Agr+23].

4.1. Existing Models and their Limitations

During the last decades, significant efforts have been directed toward the synthesis and dielectric modeling of such tailored ferroelectric-based materials. It is expected that the ferroelectric's microwave performance (reduced losses, increased tunability) can be improved beyond limitations, given by the intrinsic properties, by mixing them with non-tunable low-loss dielectrics [Tag+03]. Since ferroelectric/dielectric composite materials are generally studied experimentally, developing precise models of these engineered materials is desirable to create better devices with suitable properties.

Since the 2000s, ferroelectric composites have been primarily modeled by simple mathematical models, with components distributed in layers or columns, which do not accurately represent the nature of natural binary composites. A few years later, the approach of electric field distribution homogenization, illustrated in Figure 4.1, came into effect. This approach results in the determination of effective relative permittivities of the binary material systems. Here, ε_f and ε_d are the relative permittivities of the ferroelectric and dielectric, respectively. Whereas ε_{eff} represents the effective relative permittivity of the whole composite. The spherical inclusion models [Ber78; JS08b; She+06] are proposed based on such assumptions that the electric field is homogeneous throughout the composite. However, these models are only accurate for small concentrations (less than 8%) of additives and exhibit high inaccuracy for high dilution ratios. This inaccuracy is the result of inconsideration of significant re-distribution of electric fields due to high dielectric contrast between the spherical inclusions and the dielectric matrix within the material, making this modeling approach unsuitable for ferroelectric/dielectric composites.

With the advancements in computer-aided design (CAD) techniques, a few mod-

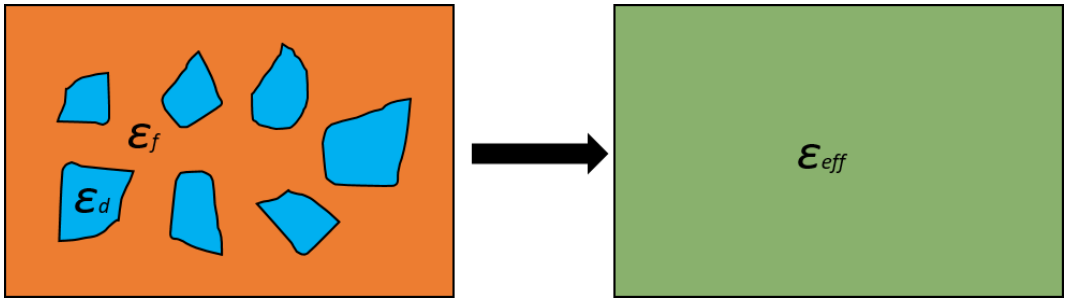

Figure 4.1.: Ferroelectric-dielectric composite homogenization with ε_f, ε_d and ε_{eff} being the relative permittivities of ferroelectric, dielectrics and the effective composite media.

els [Wie+17; Lei15] started to come into existence. These models considered the distribution of electric fields but still lack accuracy for the whole range of dilution or composite ratios. This motivates the novel CAD design method based on [Lei15] is presented here, which shows close experimental proximity between the simulation and experiment. However, before going deep into the presented model, few existing model evaluations are demonstrated concerning the ferroelectric and dielectric employed, which further strengthens the significance of the model presented.

4.1.1. Analytical Models

Usual composite analytic models are based on columnar, layered, and randomly-placed inclusions approach [Tag+03; Gev09]. Figure 4.2 shows the representation of the three approaches. Here, the mixture of ferroelectric (orange) and dielectric (blue) is placed between two metal electrodes (gray). The bias fields are applied at the metal electrodes to change the dielectric properties of ferroelectrics. For further investigations, f is considered the volumetric fractional composition of ferroelectrics in the mixture.

Columnar: In this approach, the ferroelectric block and dielectric rods are placed between two metal electrodes. Hence, this approach emulates that a capacitor based on ferroelectric and many capacitors based on dielectrics are in parallel with each other. The effective permittivity is calculated by the classical approach of capacitors in parallel. The effective relative permittivity is given by [Tag+03]:

$$\varepsilon_{\text{eff}} = f\varepsilon_f + (1-f)\varepsilon_d. \tag{4.1}$$

This approach ensures a uniform electric field distribution in the ferroelectric region, which dominates the resultant relative permittivity of the composites and the tunability of the composites. Theoretically, the resultant tunability remains the same as ferroelectric. However, the dielectric loss is also dominated by ferroelectrics

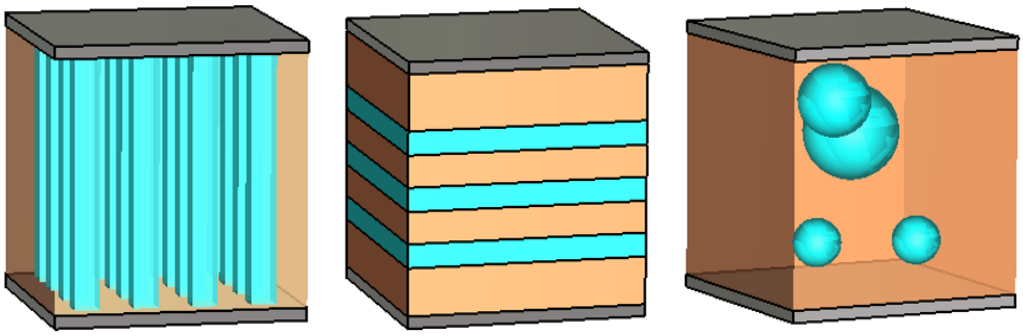

(a) (b) (c)

Figure 4.2.: Basic representation of three composite analytical models – Columnar (a), Layered (b), and Spherical Inclusion Model (c). Here, ferroelectric, dielectric, and metal electrodes are shown with orange, blue, and gray colors, respectively.

in the composite, hence, contradicting the main objective of using dielectric to reduce loss.

Layered: In this approach, the ferroelectric and dielectric layers are placed between two metal electrodes. Hence, this approach emulates that capacitors based on ferroelectrics and dielectrics are in series with each other. The effective relative permittivity is given by [Tag+03]:

$$\varepsilon_{\text{eff}} = \frac{\varepsilon_{\text{f}}\varepsilon_{\text{d}}}{f\varepsilon_{\text{d}} + (1-f)\varepsilon_{\text{f}}} \tag{4.2}$$

This series approach ensures the domination of lower relative permittivity dielectric dominating the resultant relative permittivity of the composites. Consequently, theoretically, the composite's tunability remains the same as the dielectric's, which is negligible. Although, the dielectric loss of the composites heavily reduces as more electric fields pass through the dielectrics, which agrees with the primary objective of mixing ferroelectric with dielectrics to minimize loss. However, the almost null tunability is unacceptable, and hence, this model is not widely used for the low-loss varactors manufactured in this work. This pushes the random-arranged solutions or engineered functional composites popular for such applications.

Inclusion: In this approach, the ferroelectric and dielectric elements are in parallel and in series. Hence, the classic series and parallel capacitor methods do not apply. Instead, the effective permittivity is calculated by homogenization, as shown in Figure 4.1. The irregular shapes of the inclusions phases or conglomerates are considered more recognizable shapes of circles or squares in the 2D scenario and spheres or cubes in the 3D scenario. The most popular earlier model includes the one based on Maxwell-Garnett [Gar04], and Bruggeman symmetric [Bru35] classical mixing equations. Equation (4.3) and (4.5) represent Maxwell-Garnett and Bruge-

mann symmetric mixing equation for spherical inclusions, respectively.

$$\text{Maxwell-Garnett: } \varepsilon_{\text{eff}} = \varepsilon_{\text{d}} + f(\varepsilon_{\text{f}} - \varepsilon_{\text{d}})\frac{3\varepsilon_{\text{d}}}{\varepsilon_{\text{f}} + 2\varepsilon_{\text{d}} - f(\varepsilon_{\text{f}} - \varepsilon_{\text{d}})} \tag{4.3}$$

$$\text{Brugemann Symmetric: } 2\varepsilon_{\text{eff}}^2 + \varepsilon_{\text{eff}}[(3f-2)\varepsilon_{\text{d}} + (1-3f)\varepsilon_{\text{f}}] - \varepsilon_{\text{f}}\varepsilon_{\text{d}} = 0, \tag{4.4}$$

$$\Rightarrow \varepsilon_{\text{eff}} = \frac{1}{4}\left[-3f\varepsilon_{\text{d}} + 2\varepsilon_{\text{d}} - \varepsilon_{\text{f}} + 3f\varepsilon_{\text{f}} + \sqrt{8\varepsilon_{\text{d}}\varepsilon_{\text{f}} + (-3f\varepsilon_{\text{d}} + 2\varepsilon_{\text{d}} - \varepsilon_{\text{f}} + 3f\varepsilon_{\text{f}})^2}\right]. \tag{4.5}$$

Although both equations are valid for small volume fraction limits for a regular phase of spherical inclusions, the Bruggeman effective medium theory is widely chosen because of its many beneficial properties. It averages the permittivity around each inclusion, and the electric field inside the sphere depends on the volume fraction of the spheres in the mixture. Consequently, the Bruggeman effective medium theory for spheres has a percolation threshold at a volume-filling ratio of around 0.33. The percolation threshold is the volume-filling ratio, where the effective permittivity as a function of the volume fraction of inclusions changes rapidly. For this amount of filling, randomly dispersed spheres become connected [ZZY11].

Based on the Brugemann effective medium theory, Sherman et al. [She+06] introduced a modified effective medium approximation (MEMA) model, where a non-linearity is included in the equation. This non-linearity is particularly based on the electrical sensitivity of dielectric properties of ferroelectrics. The effective permittivity ε_{eff} can be written as follows:

$$\text{Sherman et al.: } \varepsilon_{\text{eff}} = \frac{3f-1}{2}\varepsilon_{\text{f}}, \tag{4.6}$$

$$\tau_{\text{eff}} = (1.2 - 0.2f)\tau_{\text{f}}, \tag{4.7}$$

where τ_{eff} and τ_f are the mixture and ferroelectric tunability, respectively, whereas $\varepsilon_d \ll \varepsilon_f$ and $f \approx 1$ are considered conditions. The model is approximated to the lower composition of ferroelectric dilution with dielectrics. Around the same time, Jylha et al. [JS08b; Jyl08] also modified the Brugemann effective medium to include the ferroelectric non-linearity with numerical methods. This work demonstrates the permittivity dependence on electric fields [Jyl08] and is given as follows:

$$\varepsilon_{\text{eff}} = \frac{1}{l \cdot V_{\text{pot}}} \int D \cdot dA \tag{4.8}$$

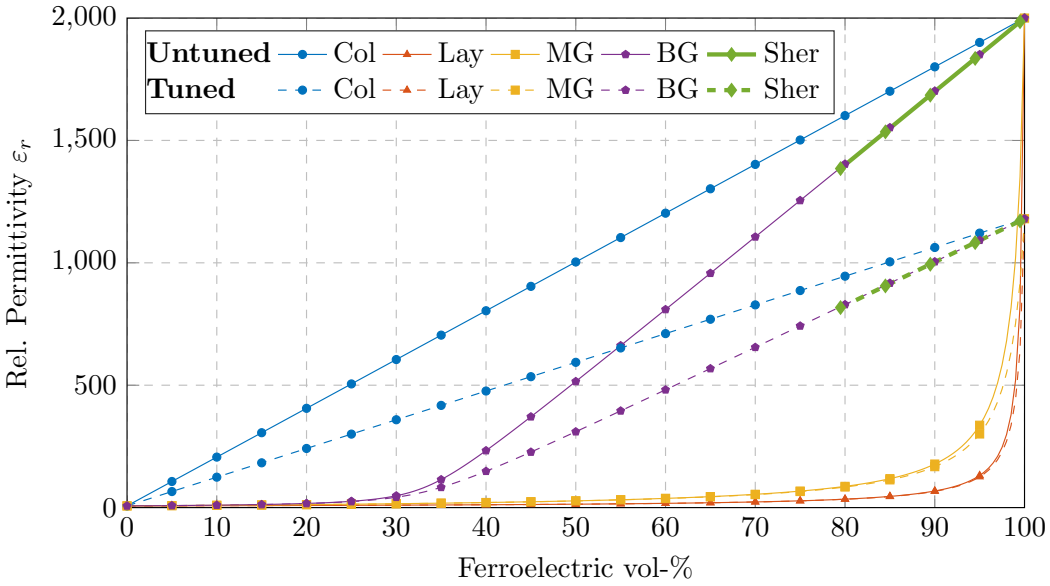

(a)

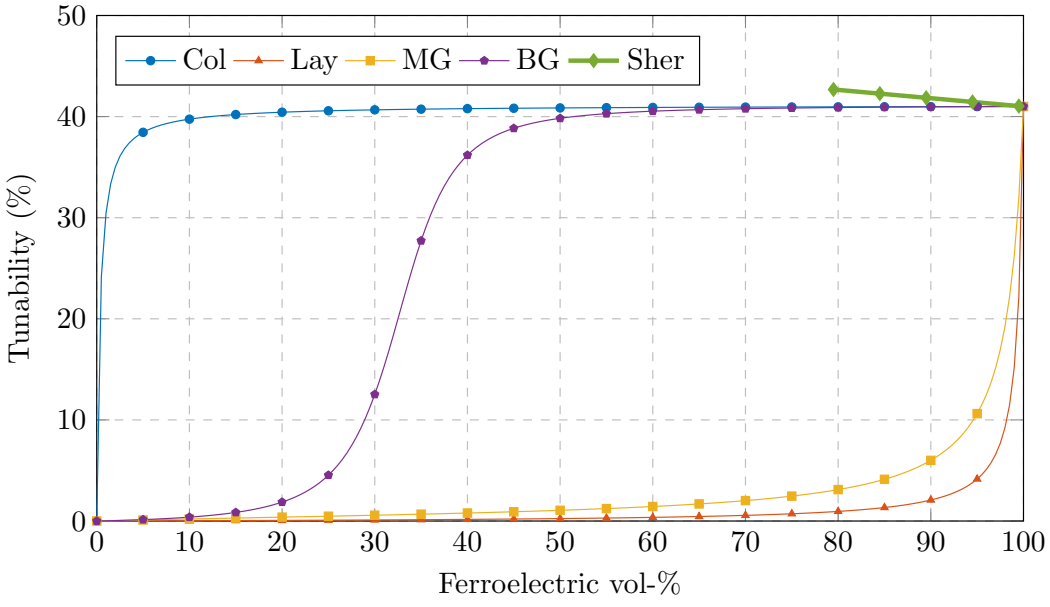

(b)

Figure 4.3.: Illustrations of the extracted permittivity (a) and tunability (b) from different composite analytical models – Columnar (COL), Layered (Lay), Maxwell-Garnett (MG), Bruggeman symmetric (BG) and Sherman et al. (Sher). (a) compares the tuned and untuned permittivities where untuned ε_r of ferroelectric and ε_r of dielectric are considered to be around 2000 and 7, respectively.

where l and A are the length and cross-sectional area of the section of composite considered with periodic boundaries, V_{pot} is the static potential difference maintained across the length of the composite varactor, and D is the electric flux. Despite both models predicting the tunability for the whole range of composites, the experimental proximity is limited to small amounts of dielectrics in Sherman et al. and small amounts of ferroelectrics in Jylha et al.

Figure 4.3 compares the analytical models discussed above regarding permittivity and tunability variations. As expected, the columnar model (COL) has similar tunability for composites and ferroelectrics. In contrast, the layered model (LAY) illustrates a behavior close to dielectric in terms of tunability for composites. Additionally, the Maxwell-Garnett (MG) behaves relative to the layered model, which depicts the dominance of dielectric behavior and is not well suited for tunable applications. Moreover, Bruggeman symmetric (BG) shows well-accepted behavior in terms of tunability and, thus, is popular among researchers until computer-aided (CAD) modeling is introduced. Sherman et al. (Sher) became popular due to its simplicity but could predict results for the short range of composites. Here, the limited experimental proximity results from insufficient consideration of the distribution of electrical fields inside the composite phases due to homogenization. This saturates the analytical propositions, and further improvements are made due to the introduction of CAD modeling in an electromagnetic environment.

4.1.2. CAD Modeling

With advancements in CAD modeling in the RF domain, many commercial CAD simulation software, such as COMSOL Multiphysics and CST Studio Suite, came into existence. These softwares can distinguish between different dielectrics due to their meshing techniques, and hence, the distribution of electrical fields inside the ferroelectric-dielectric mixtures can be studied. This modeling can be 2D or 3D in nature. The 3D simulation is more accurate but requires more time and computational resources than 2D simulations. As the main drawback of previous modeling techniques is the accuracy, more 3D simulation models are discussed here.

In [Lei15], a 3D-CAD model focuses on the random distribution of ferroelectric and dielectric cubical phases. In this approach, an assumed equivalent cubical shape replaces the real shapes and sizes of the ferroelectric and dielectric phases. In addition, this model neglected the porosity effects, which are air traps between different phases introduced during the material fabrication process. The model is simulated in COMSOL Multiphysics, and a non-homogeneous distribution of local electric fields among ferroelectric and dielectric is obtained. The extracted relative permittivity ε_r and tunability τ_ε are illustrated in Figure 4.4a. Due to a lack of clarity regarding the local electrical fields in consideration, the model's accuracy is not known. In addition, the model does not demonstrate close experimental proximity.

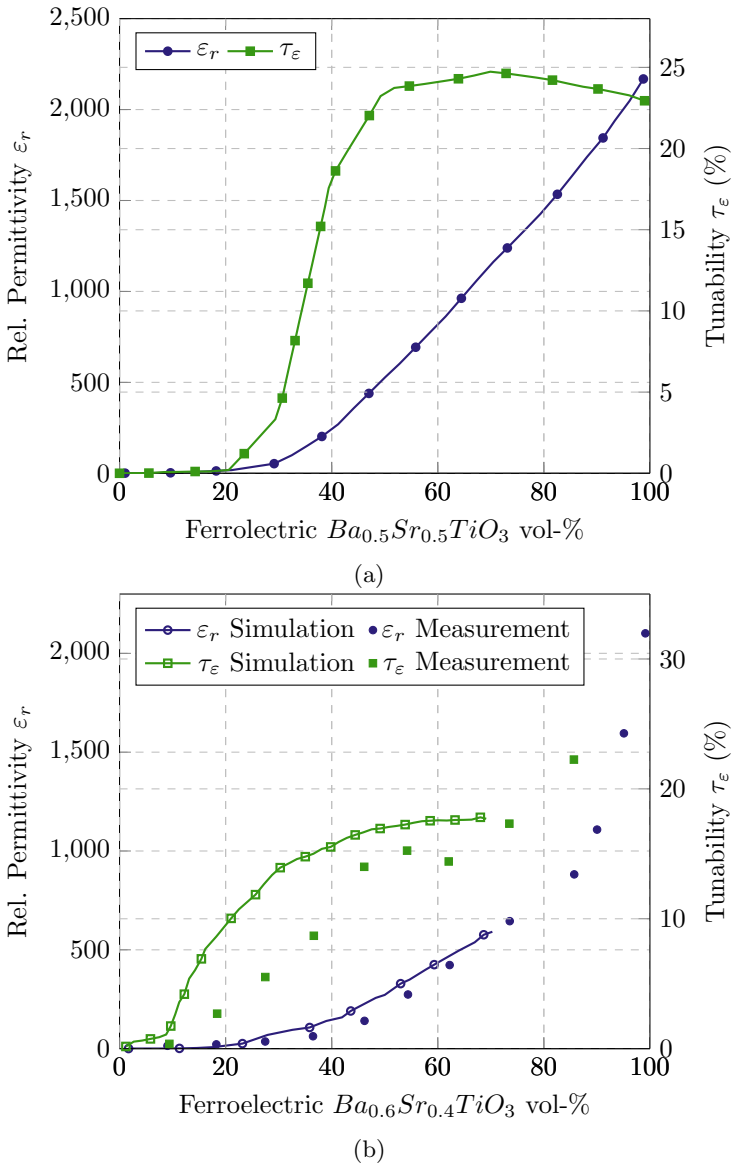

Figure 4.4.: Illustrations of the extracted CAD model results by [Lei15] (a) and [Wie+17] (b). (a) denotes the model extractions of simulated extraction of rel. permittivity ε_r and tunability τ_ε for the composites $Ba_{0.5}Sr_{0.5}TiO_3$-Mg_2TiO_4. Here the comparison with measured extractions is not mentioned. Whereas (b) compares the same parameters with extraction from measurement and simulations for different compositions of $Ba_{0.6}Sr_{0.4}TiO_3$-$Mg_2B_3O_6$ composites.

Another 3D-CAD simulation model is presented in [Wie+17], which is simulated in CST Studio Suite. The model used the spherical inclusions of ferroelectrics instead of dielectrics. According to different volumetric compositions, the ferroelectric

spheres are filled inside the dielectric background material. This model assumes the ferroelectric phase in spheres but considers the size variation of each phase. In addition, this model considers the interaction and interconnected chains of different ferroelectric phases. The model shows various statistical spreads of tunability and Q-factor due to such variations. The extracted relative permittivity ε_r and tunability τ_ε are displayed in Figure 4.4b. However, the model fails to produce results due to the resource-intensive computation above 60 vol-%. In addition, the model shows the experimental proximity for ferroelectric vol-% lower than the percolation limit of around 33 vol-%. After the percolation limit, the interconnection between ferroelectric phases increases, thereby tunabilities. This gap between the model and experiments is suspected to be due to the limited consideration of bias field re-distribution inside the different ferroelectric and dielectric phases. In addition, the model does not explain the sudden drop in tunability in composites of ferroelectric and dielectric. From now on, a novel 3D-CAD model is discussed, which considers the re-distribution of bias fields inside the composites essential to predict correct tunabilities.

4.2. Novel 3D-CAD Simulation Modeling

According to the discussions about the previous models, the main drawback faced by all the models is the limited consideration of the distribution of the local electric fields inside the ferroelectric and dielectric materials under the influence of bias fields affecting the dielectric properties of the composites. In addition, the sudden drop in tunabilities in ferroelectric-dielectric composites is still not appropriately concluded for all the vol-% of ferroelectrics. These two significant problems form the basis of this model, and close insights into the methods and techniques will be described further in this section.

Simulation Model Setup: A random-arranged cubic phase model is chosen for the simulation environment in CST Studio Suite. This model includes 1000 cubes of $1 \times 1{\times}1\,\mu m^3$ to form a complete cube of $10 \times 10{\times}10\,\mu m^3$. The cubes are divided among ferroelectric and dielectric materials based on different desired volume compositions. The tunable ferroelectric material is the perovskite ferroelectric BST in the stoichiometric form of $Ba_{0.6}Sr_{0.4}TiO_3$. This BST has the Curie temperature T_C around 0 °C, which enables the measuring operation at room temperature [Jeo04]. The displaced operating temperature is essential to ensure that the BST stays in the paraelectric or non-polar phase to maintain centrosymmetry [Jeo04]. The BST has relative permittivity ε_r of around 2000 and Q-factor Q_ε of around 100 in the lower MHz range [Wie+17]. As discussed in Section 2.5, the MBO in the form of $Mg_2B_3O_6$ is chosen as the additive, which has a ε_r and Q_ε of around 7 and 2500 [Wie+17], respectively. The whole cube of $10 \times 10 \times 10 \mu m^3$ is shown in Figure 4.5a

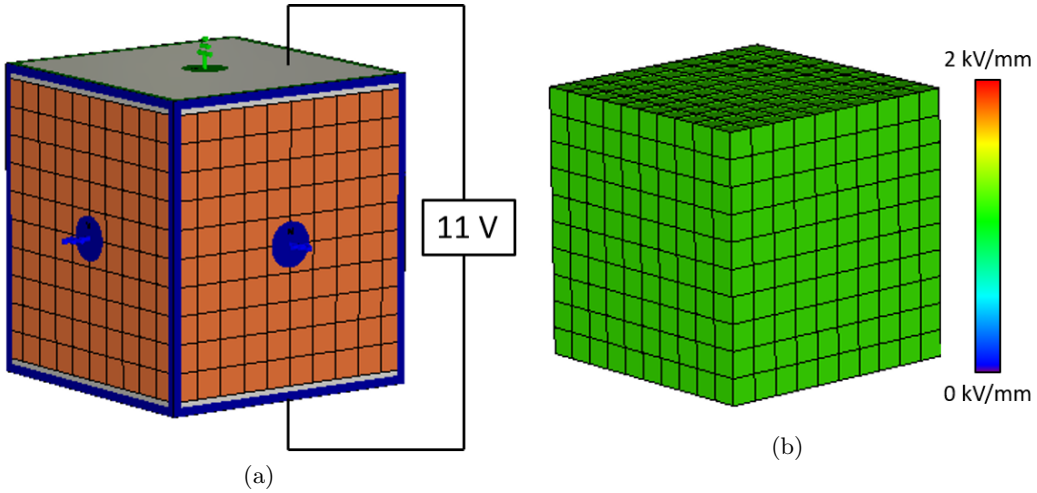

Figure 4.5.: Novel CAD model design with (a) depicting the model design and (b) revealing the field distribution. The model includes 1000 cubes of ferroelectric (orange) material between two electrodes (gray) to form a complete varactor with a bias field equivalent to 1.1 kV/mm. Additionally, as the depicted model has no permittivity contrast, the field distribution is uniform throughout the varactor.

for 100 vol-% BST composition. Electric boundaries bound the whole cube at the two opposite vertical faces, denoted by the gray perfect electrical conducting (PEC) layers, to create the effect of a parallel-plate capacitor. These boundaries also act as the bias electrodes, which are provided with a voltage potential difference of 11 V. A voltage difference or DC bias of 11 V corresponds to the 1.1 kV mm^{-1} of an overall electric field. These boundaries can also be represented with the modification of Gauss's Law as follows:

$$\nabla \cdot \mathbf{E} = 0. \tag{4.9}$$

Additionally, the rest of the faces are surrounded by magnetic boundaries to prevent leakage of normal electric flux. The varactor is then simulated using the Electrostatic Solver of CST, which results in the electric field distribution and the capacitance of the model varactor in the non-biased state. The electric field distribution is depicted in Figure 4.5b. In observation, no field variation is visible due to no ε_r contrast, although the extracted ε_r is around 2000. This ε_r is calculated using varactor dimensions and extracted capacitance in Equation (2.16). The varactor is then introduced with MBO material to create a composite varactor. Initially, a slab of MBO with dimensions $10 \times 10 \times 5\mu m^3$ is introduced, comprising the 50 vol-% of the varactor, to verify the model varactor's accuracy. The MBO is introduced in parallel as well as series configuration, and their obtained electric field distribution is

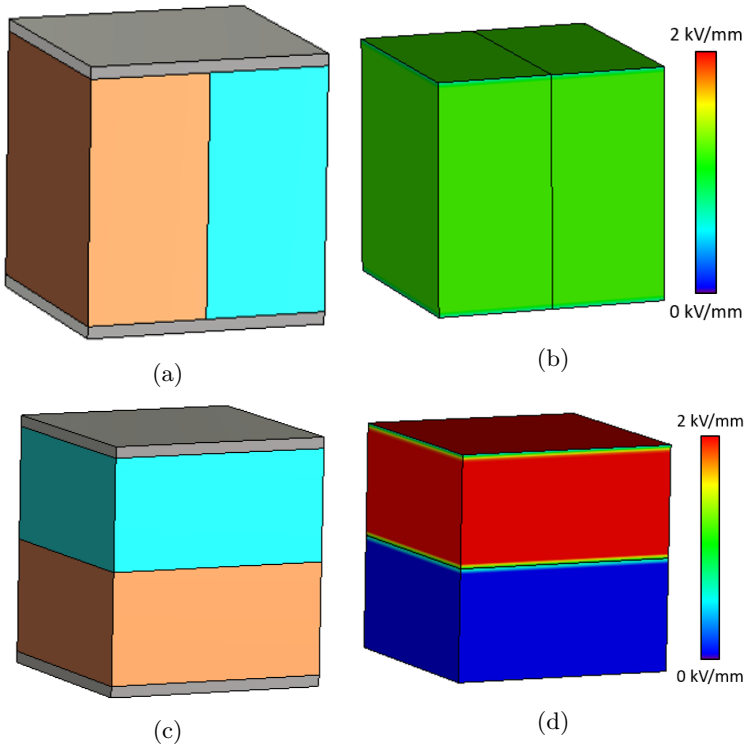

Figure 4.6.: (a) and (c) denote the parallel (columnar) and series (layered) arrangement of the BST-MBO composites, respectively. (b) and (d) illustrate the field distribution for parallel and series, respectively. The field distribution is uniform throughout the parallel arrangement, indicating the dominance of BST in tunability. Whereas the almost negligible electric field inside BST indicates the dominance of MBO towards tunable behavior.

shown in Figure 4.6. The calculated and simulated permittivities are around 1003.5 and 14.35 for parallel and series configurations, respectively. The permittivities are calculated using Equation (4.1) and (4.2) for parallel case and series, respectively. In parallel, the electric field distribution is uniform in both materials, suggesting the dominance of BST behavior. Whereas, in the series case, the electric field in BST is also almost negligible, suggesting the dominance of MBO. This verified the model for further investigations by including MBO in random arrangements in various compositions.

Consequently, different compositions of BST and MBO are randomly arranged to form a varactor as shown in Figure 4.7a, 4.7b, 4.7c and 4.7d for 80, 60, 40 and 20 vol-% BST compositions, respectively. The electric field distribution indicating the extent of the bias field present at each solid cube as shown in Figure 4.7e, 4.7f, 4.7g and 4.7h for the 80, 60, 40 and 20 vol-% BST composition varactor model, respectively. Additionally, The probability density function (PDF) of bias fields is

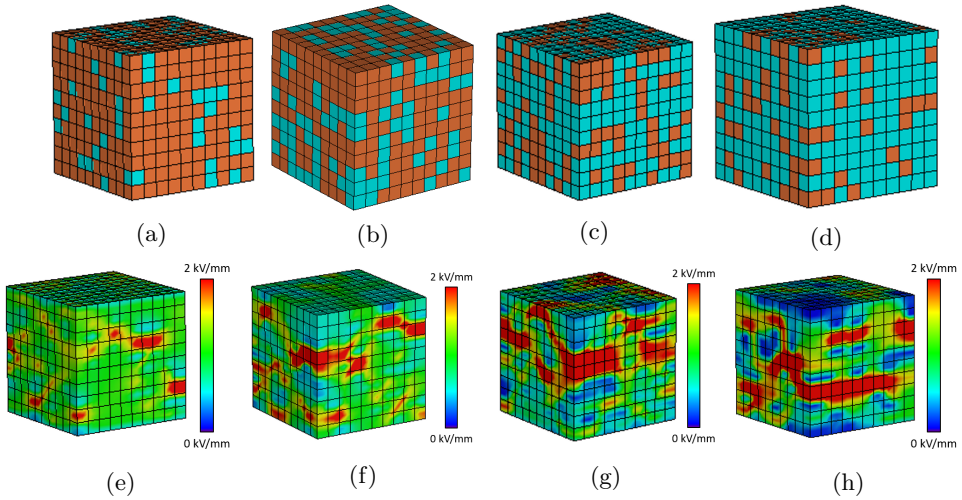

Figure 4.7.: (a), (b), (c), and (d) denote the 80, 60, 40, 20 vol-% BST composition of the BST-MBO composite varactor model random arrangements, respectively. Whereas (e), (f), (g), and (h) illustrates the field distribution for the respective compositions.

demonstrated in Figure 4.8a, 4.8b, 4.8c and 4.8d for 80, 60, 40 and 20 vol-% BST composition varactor model, respectively. The blue bar graph depicts the PDF of the average bias electric field in each mesh cell across different cubes, and the black line graph indicates their Rayleigh distribution fit. Generally, Rayleigh fit is characterized by the Rayleigh parameter σ_R, which estimates the behavior of electric field distribution of the composite varactor. With the increasing MBO Vol-%, the electric fields get more distributed across the mesh, indicating reducing electric field in the BST region. Before going more in-depth on electric field distribution analysis, the mesh dependence is validated, and an optimum setting is selected. The mesh type of 'Hexahedral(legacy)' type is chosen for these simulations as each mesh cell is in the shape of cubes or cuboids, which is the preferred form for this work. The cube or cuboid is easier to redesign to replace the untuned material with tuned material at that mesh cell. Figure 4.9 demonstrates the σ_R of different mesh configurations with increasing mesh cells for the 50 vol-% varactor. Although the model accuracy increases with the increasing number of mesh cells, the model complexity also increases, especially with later tunability implementation. Considering this trade-off between complexity and accuracy, an optimum mesh setting is chosen, as depicted with chosen mesh configuration. The σ_R starts to saturate around this configuration, which supports the selection. Compared with the succeeding configuration, the time for overall calculations and computational resources required to implement the tunability formulations across overall mesh cells increases exponentially to around four times with no notable accuracy improvements.

According to the chosen mesh configuration, the PDF and the Rayleigh distribu-

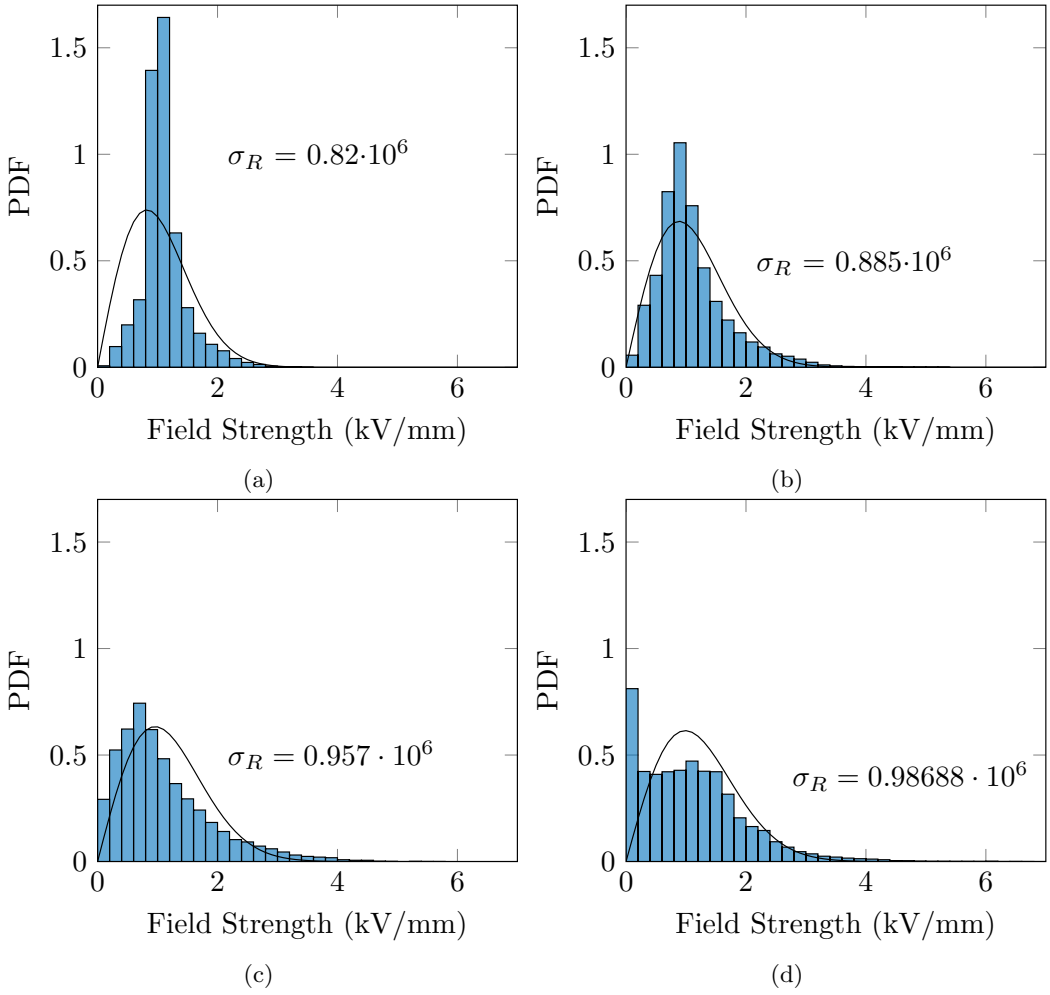

Figure 4.8.: (a), (b), (c) and (d) demonstrate the probability density function (PDF) of the 80, 60, 40, 20 vol-% BST composition of the BST-MBO composite varactor model, respectively. The blue bar depicts the electric field distribution across each mesh cell, whereas the black line is the Rayleigh distribution fit of these bias fields.

tion are calculated for the various compositions of the BST-MBO composite varactors. The extracted σ_R is shown in Figure 4.10 where the increasing σ_R with increasing MBO vol-%, denotes the electric fields shift towards MBO region as observed earlier. Although, the σ_R reduces for 20 vol-% BST varactor, which shows the decreasing trend of σ_R. The trend of increasing σ_R and then decreasing again coincides with the percolation threshold [ZZY11]. The average of overall bias fields, as shown in Figure 4.11a, are calculated to observe the division of bias fields between MBO and BST regions. Furthermore, the different random arrangements of BST and MBO cubes in each composition are influential in determining the average fields in the BST and the MBO region and the distribution of overall bias fields. Therefore,

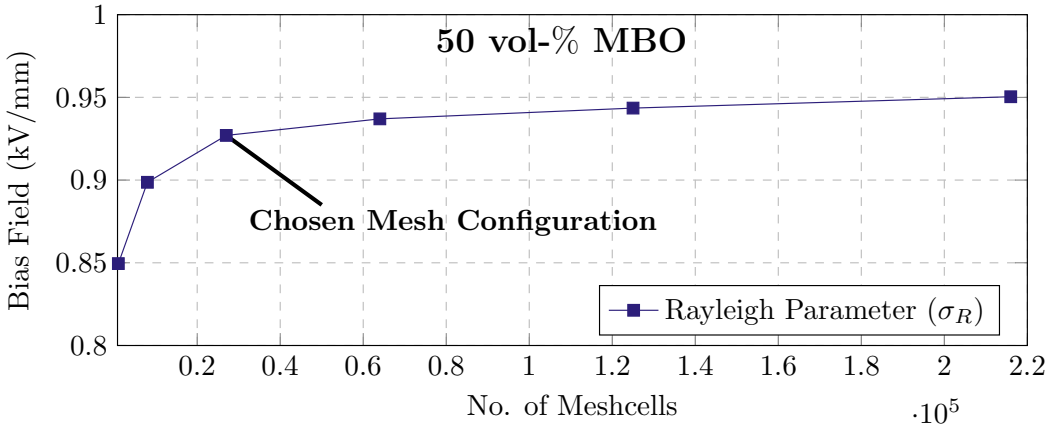

Figure 4.9.: Different mesh configurations considered in the 50 vol-% BST composition varactor model with the chosen mesh configuration.

around 50 different random arrangements for each BST-MBO composition are simulated, emulating the Monte Carlo analysis. The average of fields across all mesh cells in each simulation remains the same, and in the MBO mesh cells, field analysis is inconsequential as it is not tunable. Hence, the Monte Carlo analysis is done for the mesh cells in the BST region. However, the σ_R variations with differently arranged simulations are depicted by a shaded blue area in Figure 4.10.

Figure 4.11b displays the extracted cumulative mean μ and cumulative upper bound limit $\mu + 3 \cdot \sigma$ of the average fields in the BST region for each 50 vol-% BST composition's simulations. The decrease in this limit with increasing no. of simulations depicts commonly-occurring arrangements dominating the spread of the average bias fields and the decreasing effect of outlier compositions. As the upper

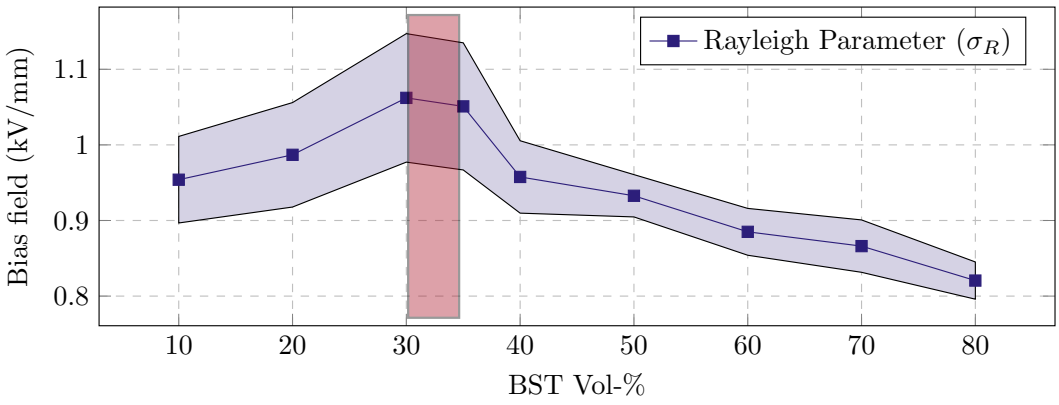

Figure 4.10.: Rayleigh parameter σ_R variations with the BST vol-% in the composite varactor. The shaded region denotes the effect of different arrangements in each composition.

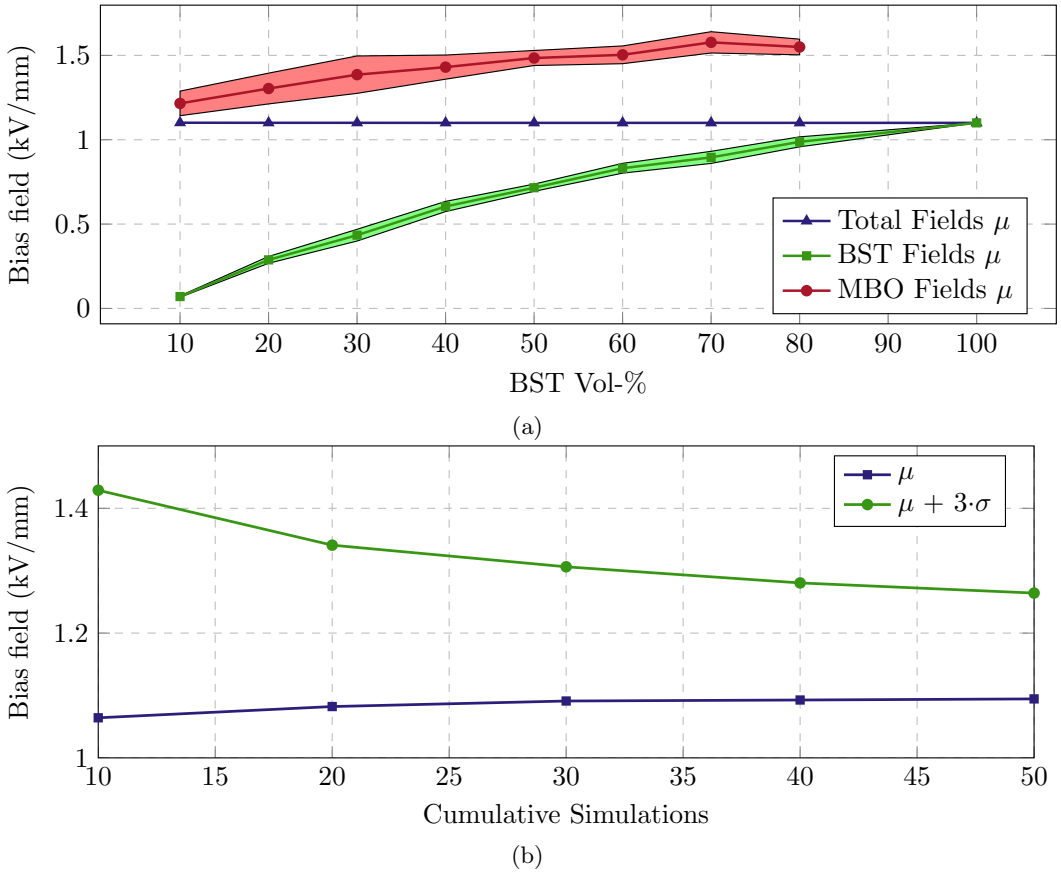

Figure 4.11.: Field analysis with mean of average fields in each region for differently arranged simulations in (a), with the shaded area representing the overall simulations variations. Whereas (b) illustrates the statistical field analysis in the BST region as it influences tunability determination. Here, the average field's mean (μ) is almost similar for all simulations. The upper limit of $\mu + 3 \cdot \sigma$ (mean + 3*standard deviation) decreases with an increase in no. of simulations, estimating the most-occurring alternative.

bound limit is settling with 50 simulations, illustrating the 50 simulations are enough to get credible bias field distribution which is valid for the most-occurring random arrangement, which can be used for further tunability investigations. The maximum and minimum of these bias fields form the range this model lies around and is shown with the shaded region in Figure 4.11a. The deviation of average bias fields in the BST region is not negligible, although not influential in producing noticeable deviation in the ε_r of the 50 vol-% BST composite varactor as well. The permittivity variations of these 50 simulations are demonstrated by blue-filled dots in Figure 4.12. A deviation of 6% from the mean ε_r value is observed here. The red triangle and the black square depict the extent of the maximum and the minimum ε_r possible, which is parallel and series configuration, respectively. Hence, the model with the mean

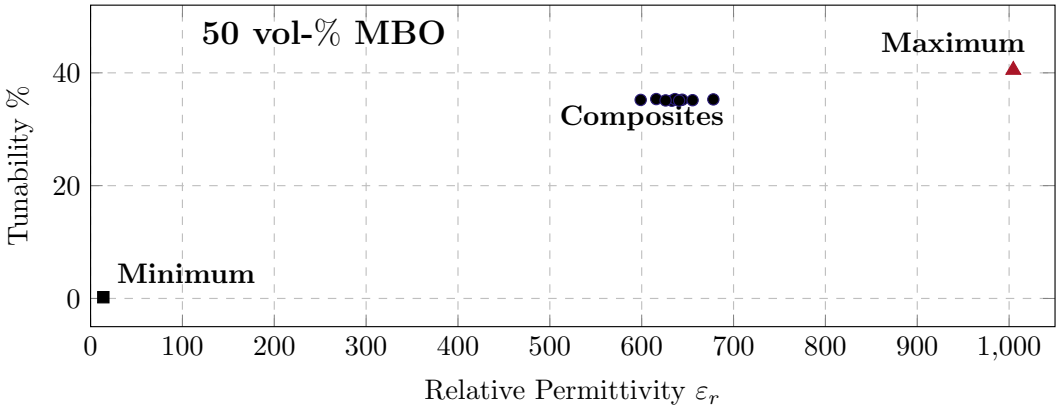

Figure 4.12.: Permittivity vs. tunability variations from the 50 vol-% BST composition model varactor with different random arrangements.

of average field distribution in the BST region is chosen for further investigation for tunability studies. The bias electric field in each BST mesh cell of this model is then used to calculate the tuned ε_r of BST in the respective mesh cells utilizing the tunability formulations, eventually creating the complete tuned varactor model.

Introducing Tunability: As already discussed in Chapter 2, the equation by Weil allows an improved adaptation to real measured data by using two fit parameters a_1 and a_2, and a supporting parameter $\tau_\varepsilon(E_A)$ [Mau11]. Therefore, Weil's equation is the suitable choice for the model in this work. This equation is given as:

$$\varepsilon_r(E) = \varepsilon_r(0)\left[1 - \tau_\varepsilon(E_A)\frac{(1 + a_1 + a_2)|E/E_A|^2}{1 + a_1|E/E_A| + a_2|E/E_A|^2}\right], \tag{4.10}$$

where a_1 and a_2 are the fitted parameters extracted from the electrical measurements of 100 vol-% BST varactor. E is the input bias electric field strength. Apart from these variable parameters, other parameters $\varepsilon_r(0)$, $\tau_\varepsilon(E_A)$ and E_A are the constants. The $\varepsilon_r(0)$ is the maximum relative permittivity at $E = 0$ or zero DC bias, $\tau_\varepsilon(E_A)$ is the maximum tunability achieved at input bias electric field strength $E = E_A$. According to the 100 vol-% BST varactor data in Table 4.1,the $\tau_\varepsilon(E_A)$ is 41.2 % at E_A=1.1 kV mm^{-1} and under room temperature conditions around 24 °C which gives the fitting parameters a_1=4.364 and a_2=5.899. In observation, Equation (4.10) fits well at higher and lower bias than other equations. This is evident from the R^2-value more than 99% depicting the goodness of fitting at all bias values. Moreover, using the extracted fitting parameters and the bias electric fields extracted from CST Studio Suite, the tuned ε_r is calculated for solids in each mesh cell in the BST region, using the Equation (4.10). These tuned ε_r are then replaced for the BST solids at the respective mesh cells. The main issue faced here is the

number of new materials formed. The new materials formed are almost equivalent to the number of mesh cells in the BST region. This requires extremely high computational capabilities, making the model extremely inefficient. A proposed solution is to quantize the tuned ε_r at the cost of an optimum decrease in the accuracy of tunability calculations. Consequently, few quantization values are tried out with the 80 vol-% composition model varactor. The 80 vol-% BST varactor ensures the worst-case performance among the considered compositions. If the quantized interval is 100, then 20 quantization levels or new materials are created with the ε_r in the range [100, 200, 300,..., 2000]. For example, for the tuned ε_r = 1393.5 after calculation, it is considered 1400 in the final tuned model varactor. Various quantized intervals in the range [1, 3.125, 6.25, 12.5, 25, 50, 100, 200] are considered. All the considered quantization intervals show similar values of tuned ε_r around 870 (after simulation). The untuned ε_r is 1450 of the whole varactor, as shown in Table 4.1. Hence, a minimum possible solution of the quantized interval of 25 is chosen for tunability investigations for all the compositions. The quantized interval above 25 are not showing any advantage regarding computational complexity, and below 25, resource usage increases substantially. Finally, an obtained color-coded tuned design model varactor for 80 vol-% BST is shown in Figure 4.13c, where the more redness indicates the more tuned region, i.e., a more biased BST region. As an example, the less bias field region (A) in Figure 4.13b displays a less tuned area in Figure 4.13c with black color and vice versa for the region (B) and (C). This tuned model varactor is then simulated to get the tuned capacitance. The tuned and untuned capacitance are used to calculate the overall tunability τ_C. The τ_C is equivalent to τ_ε for the parallel plate capacitors designed [Wie+17] and can be represented according to the following relation:

Table 4.1.: Dielectric properties of the composite materials at room temperature (around 24 °C) at 13.56 MHz. The measured (Meas.) tunability is measured at 1.1 kV bias voltage. The simulated (Siml.) tunability for composites is calculated with fitting parameters from measurements of pure BST at room temperature. The lowered sintering temperatures and reduced dielectric loss in the mixtures of MBO and BST are the main benefits of the BST-MBO composite varactors. A notable degradation in measured tunablities is observed.

BST-MBO(in vol-%)	Sinter temperature(°C)	Meas. Q_ε	Meas. τ_ε(%)	Siml. τ_ε(%)	Siml. ε_r
100-0	1350	136	41.2	41.33	2000
80-20	1050	205	7.8	40.11	1450
70-30	1000	220	6	38.35	1144
60-40	1000	286	5.9	37.72	868
50-50	1000	310	5.72	36.21	675
40-60	1000	340	4.75	35.12	428
30-70	1050	418	1.6	30.03	243
20-80	1100	850	0.72	17.52	90
10-90	1100	2714	0.025	4.09	19

$$\tau_\varepsilon = \frac{\varepsilon(0) - \varepsilon(E)}{\varepsilon(0)} = \frac{\varepsilon(0) - \varepsilon(\frac{V}{d})}{\varepsilon(0)} = \frac{C(0) - C(\frac{V}{d})}{C(0)} = \frac{C(0) - C(E)}{C(0)} = \tau_C, \tag{4.11}$$

where $C(0)$ and $\varepsilon(0)$ are the capacitance and the relative permittivity at zero DC bias, respectively, and $C(E)$ and $\varepsilon(E)$ are the capacitance and the relative permittivity at bias electric field E. V is the DC bias voltage applied across the capacitor, and d is the capacitor's thickness. E depends on V and d, which compare the distribution of bias fields in the designed varactor and the realized varactor equivalent. The V and d are scaled to maintain the same E. The dielectric loss study is neglected here, as it is not the focus of this particular model. Similarly, the model is simulated for all compositions mentioned in Table 4.1.

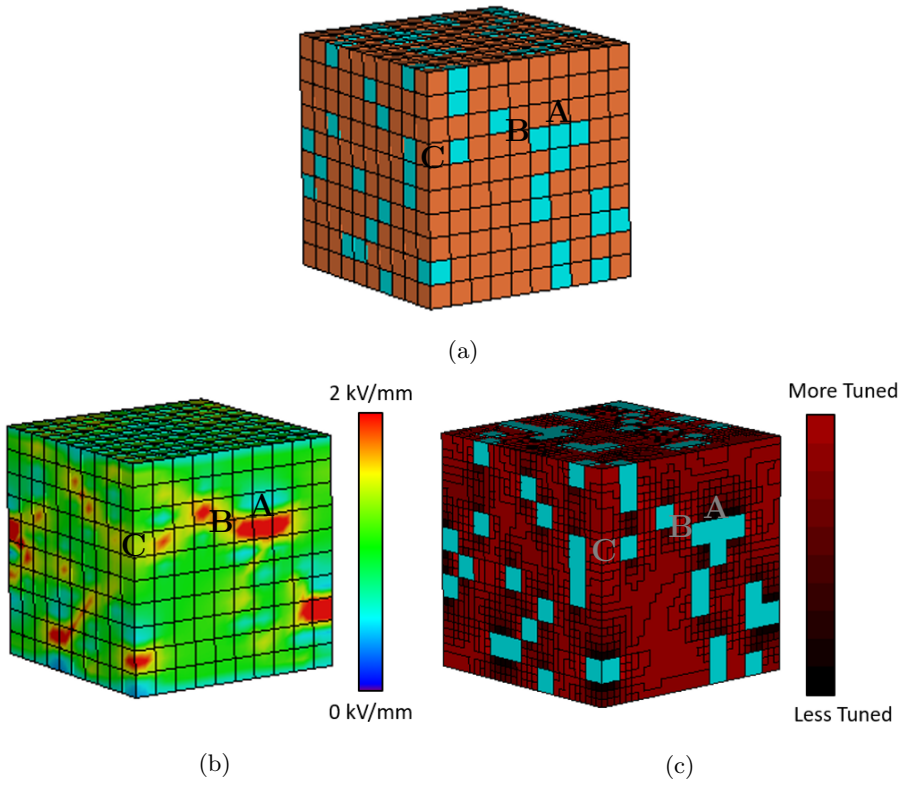

Figure 4.13.: Varactor model for 80 vol-% BST with a) representing untuned model design, b) demonstrating the bias electric field distribution, and c) depicting the tuned model design, where redness indicates the extent of tuning. Point A represents the region with a less bias electric field, so less tuned BST in this region is depicted by dark red. Similarly, points B and C represent the high-bias electric field regions, so the more tuned BST in this region is shown by bright red.

Figure 4.14 illustrates the extended σ_R of the bias fields distribution across each mesh cell for various compositions of BST-MBO. A comprehensive analysis in the red-shaded region denotes the variation in σ_R values due to different random arrangements of BST compositions between 30 and 35 BST vol-%. This analysis is done as the percolation threshold in the simulated model varactor lies between 65 vol-% MBO composition and 70 vol-% MBO composition. After performing simulation for BST vol-% in the range [31, 32, 33, 34], to calculate the highest point of σ_R. The highest value of σ_R is observed at 34 vol-% BST composition, depicting the percolation threshold [ZZY11]. The σ_R values increase with increasing MBO content and then decrease again with MBO content increasing beyond 66 vol-%. The associated shift of bias electric fields away from the BST region reduces the tunabilities substantially, illustrated by the calculated simulated tunabilities in Figure 4.15 with

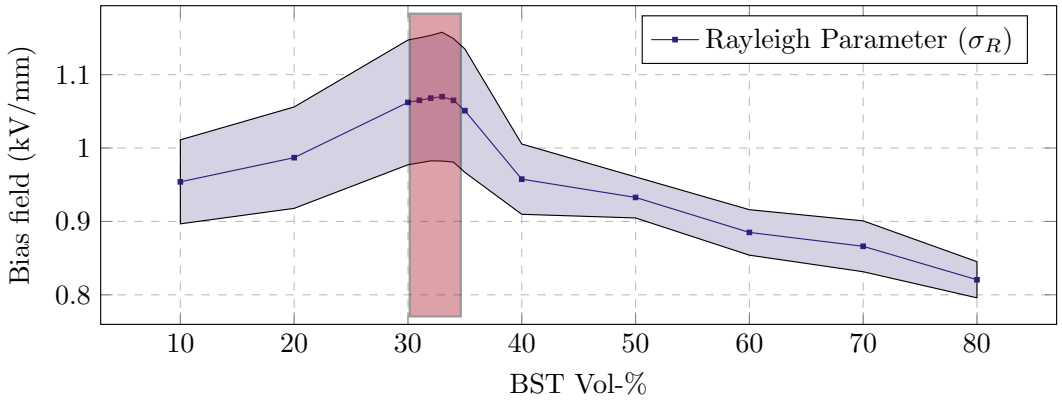

Figure 4.14.: Rayleigh parameter σ variations with the BST vol-% variation in the composite varactor with an extended percolation limit investigations. The red-shaded region denotes the region where a major displacement of electric fields from the BST to the MBO region happens.

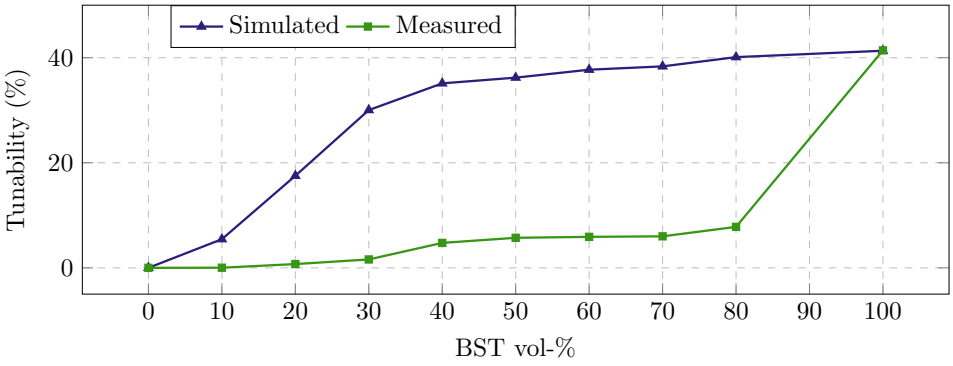

Figure 4.15.: Simulated tunability (blue triangles) with 100 vol-% BST data at room temperature as input in comparison with the measured tunability (green squares) for different BST-MBO vol-% compositions.

a blue triangle line. Upon observation, the tunabilities start declining rapidly around 70 vol-% MBO compositions, which are following the shift of bias electric fields away from the BST region, corresponding to the percolation threshold [ZZY11].

The simulation results from the model are then verified with the extracted results from the measurements, as discussed in Chapter 3. A significant difference is witnessed, as shown in Figure 4.15, which immensely questions the model's credibility. For this reason, a detailed physical study is performed to inspect the varactor's structural or material damages.

4.3. Structural Analysis of Substitution Effect

The initial physical investigations are performed by using scanning electron microscope (SEM) scans with XRD studies. The SEM scans of the microstructure are taken using an SEM (Supra 55, Zeiss, Oberkochen). The SEM scan images are exhibited in Figure 4.16a. The BST and MBO are represented by white and black color, respectively. Moreover, upon observation, the gray-colored region is also detected, which denotes the presence of the third material phase. Additionally, the SEM is equipped with an energy dispersive X-ray (EDX) setup (EDAX, AMETEK GmbH, Wiesbaden) to observe the elemental distribution in the composite varactor under test. An EDX line scan is recorded for the composition of 40 vol−% BST varactor, as shown in Figure 4.16b, which demonstrates the elemental distribution across the BST and MBO regions as well as the interface boundary. No recognizable substitution is observed in the BST region, particularly the Mg^{+} substitution, which has been suggested in [ZZY11] as the prominent reason for lower tunabilities. However, weak Mg^{+} doping might be suppressed under the detection limit of the EDX. Moreover, in the MBO region, a considerable amount of Ti^{4+} ions are detected. This leads to significant oxygen vacancies in the BST region. Since the central position in the BST lattice is either unoccupied or substituted by another element, the tunabilities are affected severely. Considering both the SEM images and EDX line scan, the presence of the third phase can be confirmed with the gray color in SEM images and Ti^{4+} substituted to the MBO region in the EDX line scan. The identity of the third phase cannot be concluded but is suspected to be Mg_2TiO_4, considering the Raman spectral analysis [Häu+21], for the similar varactors. This effect is termed as substitution effect in this work due to its effects not being limited to an increase in the doping range but also in the mixing range. The upcoming section demonstrates how this effect can be measured proportionally with a physical parameter like temperature and its integration in the electromagnetic environment, which is crucial for the model's accuracy.

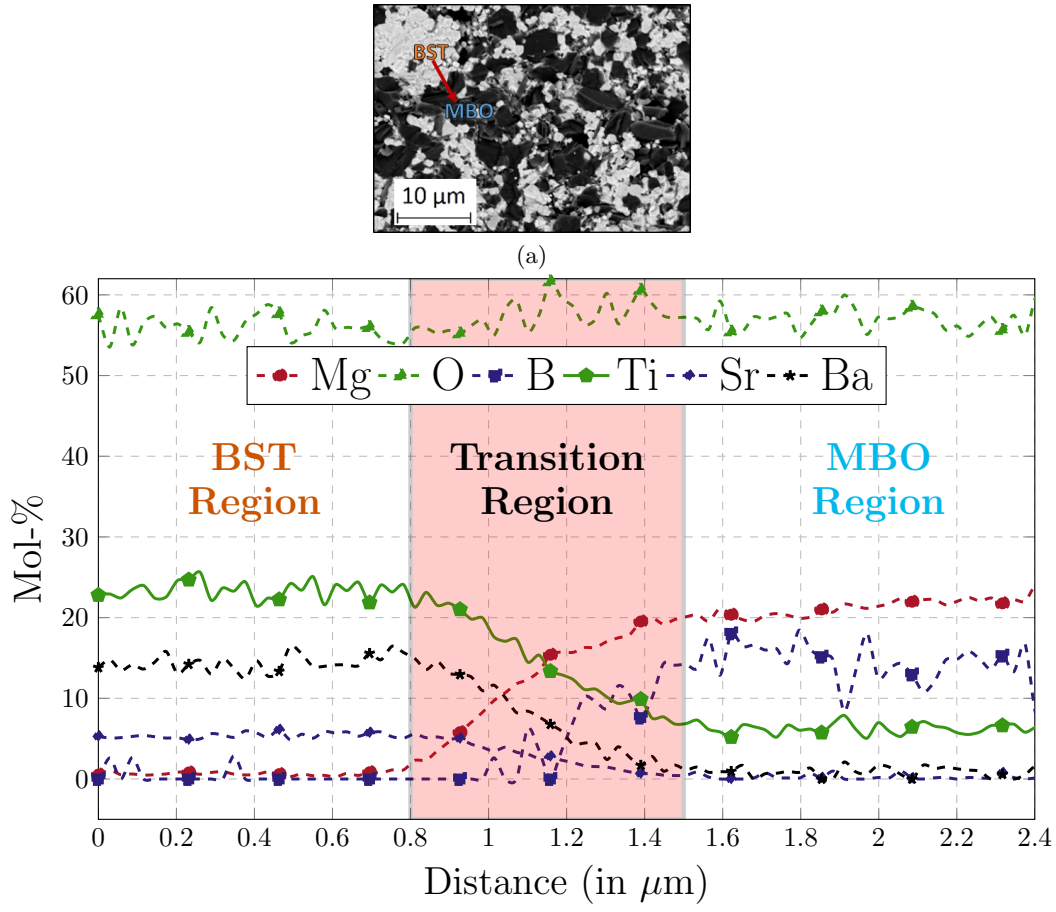

Figure 4.16.: (a) portrays the SEM image of the 40 vol–% BST pellet with BST in white color and MBO in black color. The red line denotes the path of the EDX line scan, as shown in (b) for the 40 vol–% BST pellet. The undesirable detection of Ti^{4+} ions in the MBO region, shown by the green-filled pentagon line in (b), denotes the substitution effect. This substitution effect leads to the formation of the third phase, and the presence of this third phase is witnessed in SEM image with gray color and is suspected to be Mg_2TiO_4 [Häu+21].

4.3.1. Thermal Analysis of Curie Temperature Shifts

According to [SB04], the formation of the third phase in the ferroelectric-dielectric composite structures is related to Curie temperatures (T_C) or maximum relative permittivity temperature (T_{Max}) or phase-change temperature (T_P) [VVK00]. It is to be noted that for bulk ceramics, the following relation is assumed:

$$T_{\mathrm{C}} = T_{\mathrm{Max}} = T_{\mathrm{P}}. \tag{4.12}$$

The relation fails to hold its relevance when thick-film or thin-film technologies are considered (see Figure 2.6). Hence, a simple analytical relation utilizing the two measured capacitance extraction is formulated, employing Equation (2.25) in paraelectric or non-polar phase. This relation is as follows:

$$T_C = \frac{\varepsilon_{r1}T_1 - \varepsilon_{r2}T_2}{\varepsilon_{r1} - \varepsilon_{r2}} = \frac{C_1T_1 - C_2T_2}{C_1 - C_2}, \tag{4.13}$$

where ε_{r1} and ε_{r2} are the relative permittivities at temperatures T_1 and T_2, respectively. As capacitance is proportional to permittivity, the C_1 and C_2 are measured capacitances at temperatures T_1 and T_2, respectively. Consequently, the T_C is predicted for various composites in the non-polar phase analytically. In this equation, two observations at room temperature and 50°C are considered. The predicted graph is shown in Figure 4.17 with the blue-triangled line, which shows strong arguments for experimental thermal characterization of various varactor compositions. The graph demonstrates the decreasing T_C with decreasing BST vol-%. These shifts in T_C lead to a decrease in capacitance, and hence, tunability at room temperature which is the measuring temperature for the varactor samples used in this model. And this decrease in tunability due to T_C-shifts, is not included in the electromagnetic modeling. However, from the simplified analytical analysis, only the idea of T_C shifts can be taken, and more validated experimental analysis is needed to prove the real T_C-shift scenario. As discussed in Chapter 3, the thermal characterization setup shown in Figure 3.5 is set up in-house to thermally investigate all the composite varactor possible in the range of -30°C and 30°C. The continuous temperature measurement approach is chosen for these measurements due to its reliability in producing consistent and resource-efficient results extraction.

Initially, the 100 vol-% BST varactor is characterized to verify the accuracy of

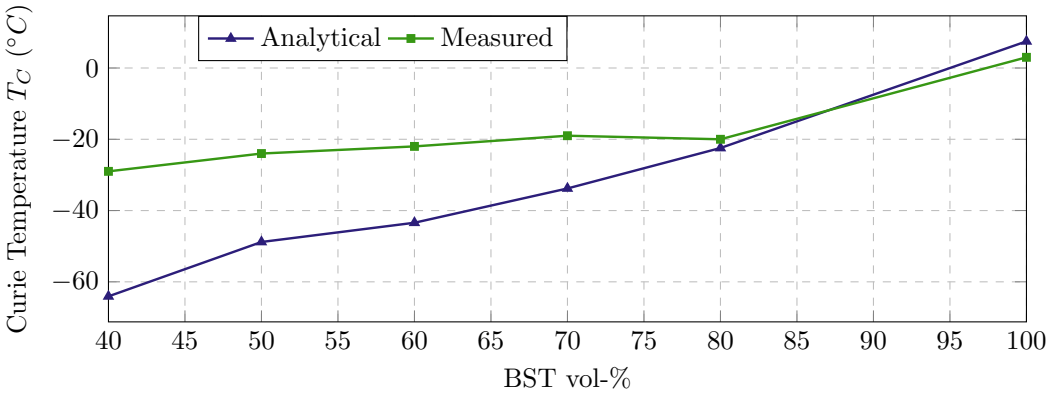

Figure 4.17.: Curie Temperature vs. BST vol-% with analytical and measured comparison.

the setup. The theoretical T_C is around 2°C for the stoichiometric ratio of the BST chosen for this analysis. Figure 3.6 shows the measured capacitance with the varying temperature. The temperature at which the highest capacitance peak is recorded is taken as the T_C. The extracted T_C from measurement is around 3°C, which is close to the theoretical value of 2°C. Similarly, the other possible composite varactors are thermally characterized. Below 40 vol-% BST, the T_C shifts below -30°C, exceeding the minimum reachable temperature limits of the setup. Nevertheless, the concept of T_C shifts is experimentally established with the available set of measured T_C, which provides a reasonable cause for the difference between simulated and experimental tunabilities. Table 4.2 illustrates all the measured T_C-shifts for various compositions possible. Additionally, the table includes the updated fit parameters for the respective composition's substitution effect. The decreased T_C with MBO addition conclusively establishes the substitution effect is proportional to T_C-shifts and further, its integration with the electromagnetic environment is demonstrated.

4.3.2. Substitution Effect Modification

As it is established that T_C shifts are proportional to the substitution effect, which causes the significant difference in simulated and experimental tunabilities. So, suppose these T_C shifts can be included in the varactor simulation model. In that case, the substitution effect is excluded from the varactor simulation model, and the composite varactors are examined according to electromagnetic behavior. Considering this, a solution is devised to include T_C shifts in the model in the CST Studio Suite simulation environment.

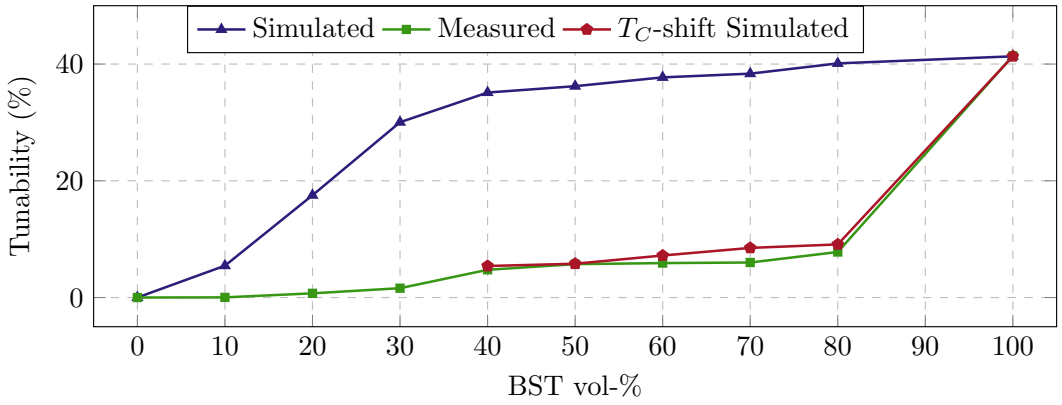

Figure 4.18.: Tunability comparison between simulations with 100 vol-% BST varactor data at room temperature in blue triangles, measurements in green squares and T_C-shifted simulations with 100 vol-% BST varactor data at different temperatures in red pentagons. All the measured observations exhibited are performed at 13.56 MHz under room temperature conditions and 1.1 kV maximum bias.

Table 4.2.: Measured Curie temperature T_C and extracted input fitting parameters for updated electrical characterization for different BST-MBO vol-% composite varactors.

BST-MBO(in vol-%)	$T_C(°C)$	100 vol-% BST varactor|		
		$T_{M,updated}(°C)$	$\tau_{\varepsilon,updated}(\%)$	fit parameters(a1,a2)
100-0	3	24	41.2	(4.364, 5.899)
80-20	-20	47	9.35	(-0.1342, 0.2767)
70-30	-19	46	9.35	(-0.1342, 0.2767)
60-40	-22	49	7.5	(-1.272, 0.6316)
50-50	-24	51	7.25	(4748, -1934)
40-60	-29	56	6.2	(4.168, -2.503)

To merge the effects of T_C shifts, extensive extra measurements for 100 vol-% BST varactor are performed as the base for the updated simulations for the respective composites. Here, the 100 vol-% BST is measured at $T_{M,updated}$, which is shifted by the gap between the T_C of 100 vol-% BST and composite varactors:

$$T_{M,updated} = T_M + [T_C(100) - T_C(y)], \tag{4.14}$$

where $T_{M,updated}$ is the updated measured temperature of 100 vol-% BST composition, T_M is the regular measured temperature i.e. room temperature around 24 °C and $T_C(y)$ is the T_C of y vol-% BST composition. The result of this 100 vol-% BST varactor's measurement at the updated temperatures is considered for the inputs in the selected tunability model equation (see Equation (4.10)) for updating the simulation varactor model. The calculated $T_{M,updated}$ for the different compositions related to BST $Ba_{0.6}Sr_{0.4}TiO_4$ is given in Table 4.2. The analysis for BST $Ba_{0.7}Sr_{0.3}TiO_4$ reaches higher temperature boundaries of the electrical characterization setup, which introduces vulnerability in the extracted measurements. The vulnerabilities introduce errors in deriving fitting parameters. Hence, only $Ba_{0.6}Sr_{0.4}TiO_4$ composites are considered for updated measurements. For 80 vol-% and 70 vol-% BST composite varactor, the measurements of 100 vol-% BST varactor measured at 46-47 °C is considered for fitting parameter extraction for the Equation (4.14) as the difference in T_C is negligible. Similarly, for 60, 50 and 40 BST vol-% compositions in consideration, the measurements of 100 vol-% BST varactor measured at 49 °C, 51 °C and 56 °C, respectively, are considered for fitting parameter extraction. After simulating the T_C-shifted tuned varactor model for all compositions, the calculated simulated tunabilities are observed close to measured tunabilities as illustrated in Figure 4.18. For all compositions, the difference in tunabilities is reduced from around 32% to under 2.5%. Moreover, the measured tunabilities are still exhibiting slight deviation from simulated tunabilities, which can be attributed to the lack of consideration of real shapes of each material's phase in the model. In addition, the cubical shapes of each phase are responsible for corner radiation effects, leading to a slight increase in the tuning of BST at the corner interface of BST and MBO. Additionally, slight

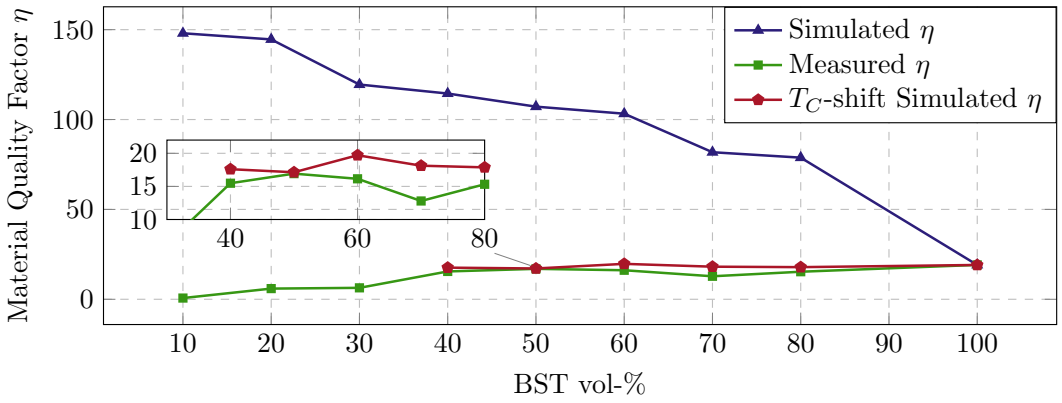

Figure 4.19.: Material quality factor η : comparisons between simulations, measurements and T_C-shifted simulations.

thermal vulnerabilities in the high-temperature measurements of the 100 vol-% BST varactor are also observed to be the reason for the deviation, as it affects the fitted results from Equation (4.10).

Ultimately, the performance of the varactor or figure-of-merit (FOM) is evaluated using the material quality factor η [Gie09], and is defined as

$$\eta = Q_\varepsilon \cdot \tau_\varepsilon. \tag{4.15}$$

The η variation is displayed in Figure 4.19 for all composite varactors. Here, the Q_ε is considered the same as discussed in Table 4.1, for all simulations and measurements. However, the tunabilities are taken from the T_C-shifted simulations and extracted measurements in Figure 4.18 for the respective simulations and measurements. The varactor with 50 and 60 vol-% BST possesses the highest η around 18, illustrating the most optimum performance from the aspects of tunability and dielectric loss. However, the τ_ε is less than the higher BST content varactor. The trade-off between Q_ε and τ_ε is essential in realizing the low-loss characteristics for composite varactors. Moreover, these composite varactors are expected to operate up to a maximum bias voltage of 6 kV before breaking down. Hence, by extrapolating the η, as mentioned in [Agr+21], a substantial improvement in tunability can be expected, provided the acoustic effects are under control. Therefore, the next chapter discusses the acoustic resonances present in the BST varactor and their suppression with the addition of MBO.

5. Modeling Acoustic Resonances and its Suppression

Apart from dielectric loss, the acoustic resonances are degrading the Q-factor of the ferroelectric-based devices. These resonances result from electric-field-induced electrostrictive strain across the ferroelectric layer, resulting in acoustic waves reflected from adjacent layers, reducing the varactor's Q-factor. In thin-film devices, acoustic resonances are a well-known phenomenon [Gie+08; Gha+16] and, recently, their presence in thick-film applications has also been observed in the lower MHz range [Kie+18a]. As we advance, acoustic resonance methodology and a method for their suppression in BST-based bulk-ceramic varactor will be discussed by using the composite ceramic approach. It is to be noted that this work is adapted from the work presented in [Agr+21].

5.1. Analytical Principle

As discussed in Chapter 2, the main acoustic activity is present inside the ferroelectric layer of the varactor. To understand the analytical concept, a parallel-plate varactor with a bulk ferroelectric layer between two thick electrodes is assumed. Due to the acoustic nature of ferroelectric crystals, an acoustic strain is induced across the layer with the application of an electric field. Revisiting the main principle of acoustic generation, according to [Li+14; New05], this strain is represented as

$$S = GP^2(E), \tag{5.1}$$

where G is the voltage electrostrictive coefficient and $P(E)$ is the polarization due to the electric-field E across the layer. The characterization of the functional materials, such as BST, is done by performing small-signal analysis with a large DC bias signal E_{DC} to tune the material layer. A small RF is chosen to maintain the linearity of the varactor's performance by keeping the effects of harmonics under the detection limit. Additionally, the BST is stoichiometrically aligned to be in the non-polar or paraelectric phase to maintain centrosymmetry [Jeo04]. This leads to negligible remnant polarization P_R. Therefore, the large DC bias signal is mainly responsible for the polarization P(E). Therefore, the strain is simply expressed as

$$S = GP^2(E_{DC}) \propto G\varepsilon^2 E_{DC}^2, \tag{5.2}$$

where ε is the BST layer's permittivity. As G is inversely proportional to the permittivity of the ferroelectric layer ε [Li+14; New05], modifying the Equation (5.2)) to

$$S \propto \varepsilon E_{DC}^2, \tag{5.3}$$

which suggests that the strain is directly dependent on the permittivity of the material along with the bias fields. Finally, the induced piezoelectricity D is expressed as

$$D = \frac{\partial S}{\partial P(E)} = 2QP(E_{DC}) \propto 2G\varepsilon E_{Tun}, \tag{5.4}$$

which is responsible for the presence of acoustic in the small RF signal.

Physically, the displacement of the Ti^{4+} ions in the BST crystal with the application of large bias fields leads to the above-mentioned strain S. This generates a proportional mechanical energy to counter the ionic displacement of Ti^{4+}. Consequently, acoustic waves are provoked due to this mechanical energy. A part of this energy is reflected back to the BST layer at interfaces to adjacent layers, forming standing waves or acoustic resonances. Simultaneously, due to energy conservation, the acoustic waves lead to an increase in the varactor's loss, which is detected in the increase in equivalent series resistance (ESR) [GVL06]. The increase in ESR leads to a decrease in Q-factor Q_ε. Since these acoustic resonances are harmonic in nature and are spread over a frequency range, equivalent harmonic drops of the Q-factor or spikes in ESR are witnessed in the affected frequency range. According to Equation (5.3), the proposed solution is to introduce a small amount of low-dielectric-constant (LDK) material, such as Magnesium Borate $Mg_2B_3O_6$ (MBO) to the BST layer to reduce the relative permittivity ε_r of the BST layer. This eventually reduces electrostrictive strain S and, thereby, the effects of induced piezoelectricity D, as is deduced in Equation 5.4. Hence, the effects of standing acoustic waves are minimized. However, it is to be noted that the reduction in this ε_r comes at the cost of a decrease in tunability. In the next section, a detailed modeling approach utilizing the COMSOL Multiphysics Simulation environment is demonstrated to showcase the suppression of such acoustic effects.

5.2. 2D-CAD Acoustic Simulation Model

The crucial dimensional parameter for acoustic is the thickness of the ferroelectric layer, which decides whether the acoustic activity is interfering with the varactor's performance. Other significant dimensions are determining the behavior of the

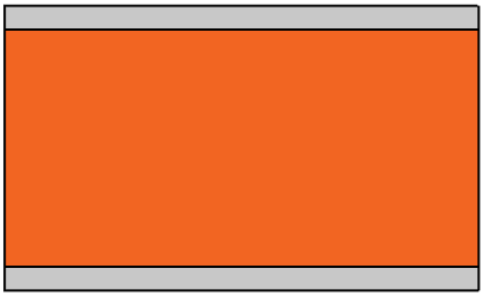

Figure 5.1.: Preliminary 2D simulation model design with BST (orange) between two silver electrodes (gray) without the inclusions. The BST is 2×1 mm^2 in dimensions.

acoustic resonances rather than their presence or generation. This leads to the 2D modeling sufficient for simulating the effects of acoustic resonances and their suppression. Additionally, a multifold increase in computational complexities associated with the introduction of 3D modeling forces the use of 2D modeling prominently in this work. Furthermore, this model requires the coupling of both the electromagnetic and mechanical domains at the same time. Hence, COMSOL Multiphysics is chosen for simulations, as it provides the integration of the RF and Structural Mechanics modules.

Consequently, a piezoelectric/acoustic simulation environment is set up in COMSOL Multiphysics, as shown in Figure 5.1, where a BST bulk of 2×1 mm^2 cross-section is placed between two silver electrodes to form a parallel-plate varactor. In the third dimension, the varactor is assumed to be uniform, forming plane-symmetric geometry. The model is in the strain-charge form of the piezoelectric effect, computing the structural strain S from the applied electrical field E to investigate the electrostrictive effects of the BST-based varactors, as mentioned in [Kie+17]. Here, the elastic compliance s_{33} is marginally higher in comparison, at around $6.35{\cdot}10^{-12}$ Pa^{-1} [AE18], to compensate for the lower strontium content in the BST considered. This BST, which is $Ba_{0.7}Sr_{0.3}TiO_3$, is taken for its operation at around $50°C$, leading to Curie temperature around $27°C$. Whereas, the coupling compliance d_{33} is taken as $8.56{\cdot}10^{-11}$ CN^{-1}, which is similar to the naturally occurring ferroelectric crystal $BaTiO_3$. The other crucial material parameter is the density of the ferroelectric material, which is taken to be around 5000 kg/m^3. The permittivity of BST is taken to be around 2000 [Wie+17]. In the composite varactor configuration, a small amount of BST is replaced by the low dielectric constant (LDK) additives. Experimentally, MBO is chosen due to its extremely low dielectric loss and its ability to reduce sinter temperatures [ZZY11]. However, due to the lack of knowledge of MBO's mechanical parameters, the material for LDK additives is chosen to be COMSOL pre-defined linear elastic material, Alumina Al_2O_3, with a dielectric contrast of around 1:350 in comparison with BST. Alumina's relative permittivity is defined as 9, which is close to the MBO's permittivity of around 7 [Wie+17]. As the effects

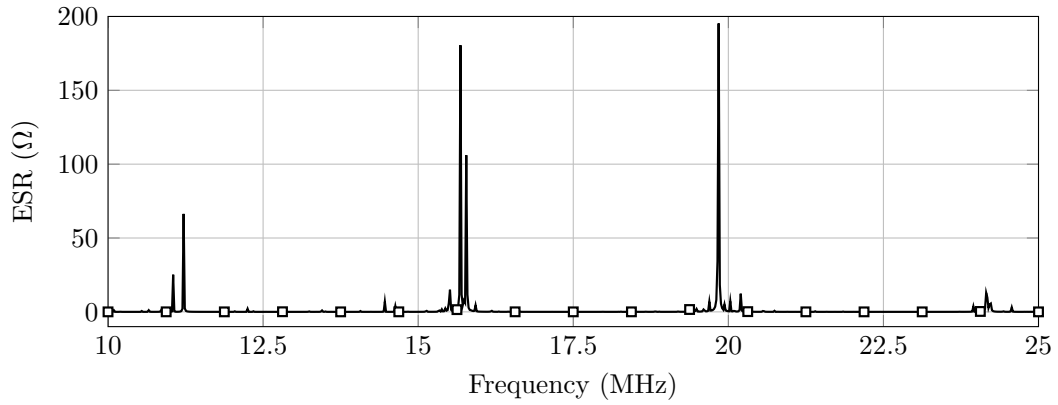

Figure 5.2.: The extracted simulated ESR vs. frequency for the BST varactor with no inclusions from the preliminary 2D model. A presence of strong acoustic activities at around 11.3 MHz, 15.7 MHz, 19.9 MHz, and 24.1 MHz.

of lower permittivity of additives are investigated here, Alumina appears to imitate MBO's properties well. The mechanical and electrical effects are coupled using the combination of 'Electrostatics' and 'Solid Mechanics' study modules. In solid mechanics, using the piezoelectric property, the mechanical damping coefficient is set at 0.001 to contribute to the structural loss for the BST bar. Under electrostatics, the piezoelectric charge conservation property is applied to the BST bar. Additionally, a bias voltage is applied at the lower electrode, and the upper electrode is taken as ground. The level of bias voltage, however, is of less significance as the model deals with the detection and suppression of acoustic activity.

Initially, the model without inclusions is simulated to demonstrate the presence of acoustic resonances. As stated previously, in Section 5.1, the acoustic activity is observed in the form of an ESR vs. frequency relationship. The 'Structural' and 'RF' physics modules are selected in COMSOL Multiphysics to include the effects of both material and RF domain. The requisite settings for these modules and mesh configurations are set. The model setup considers the impact of material properties influence in the longitudinal directions only and neglects the other directions due to open boundary constraints in other directions. Finally, frequency domain analysis is performed to extract the ESR values as displayed in Figure 5.2. The figure confirms the presence of strong acoustic activities at around 11.3 MHz, 15.7 MHz, 19.9 MHz, and 24.1 MHz, which degrades the varactor's performance considerably. With slight changes in the thickness of the varactor, the ESR peak frequency shifts. These shifts are not beneficial in the working environment as these resonances can interfere with the working frequency, which makes the suppression of these resonances more critical. The main focus of this model is to either suppress the resonances completely or shift the resonances to higher or lower frequencies. Considering this, three approaches are considered, namely – layered, columnar, and inclusions, to introduce

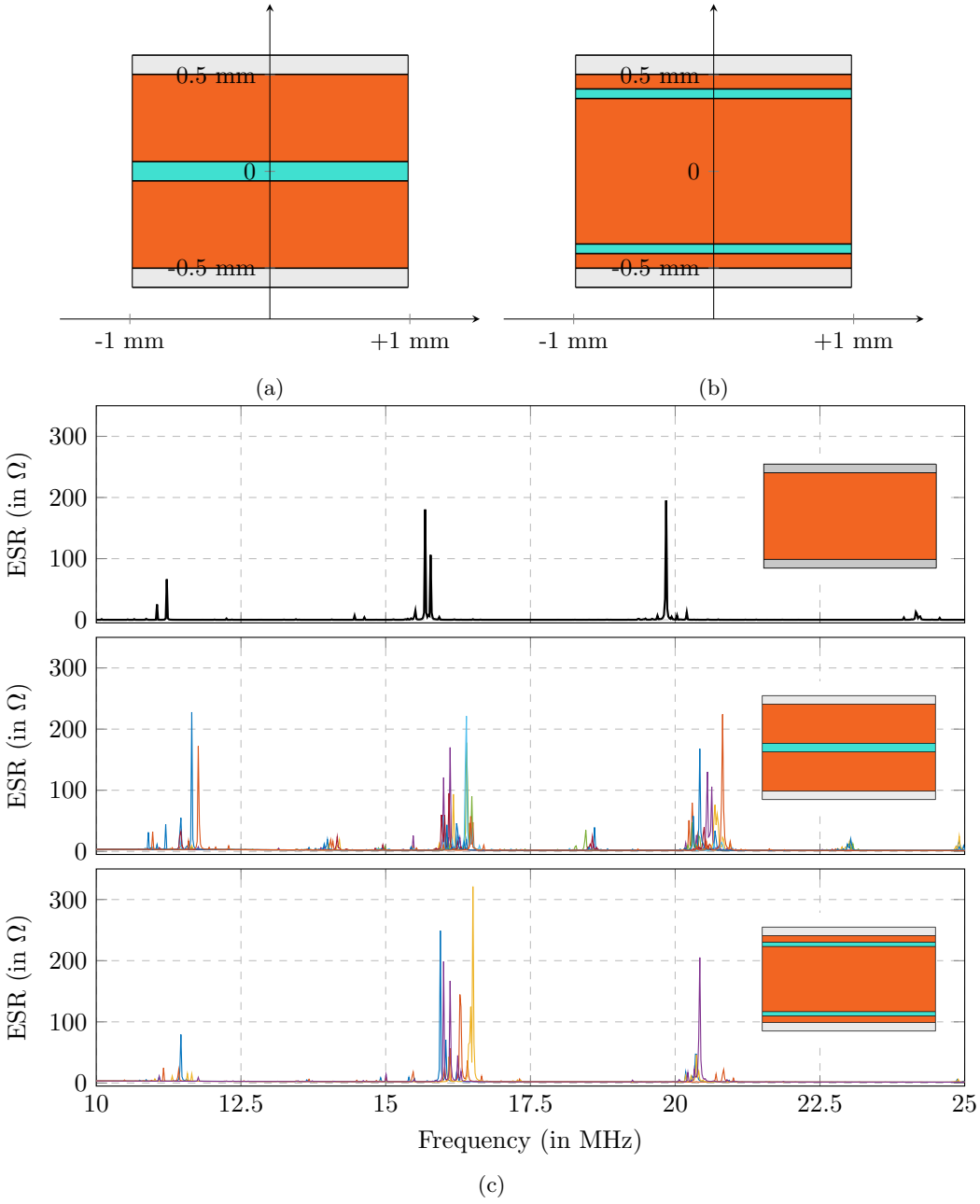

Figure 5.3.: Preliminary 2D model in the layered approach, with (a) and (b) signifying the single and double layered approach. In both configurations, the 10% LDK layer, in an additive composition, is placed along the vertical direction at different positions to investigate acoustic suppression. (c) denotes the extracted simulated ESR vs. frequency comparison in the layered approach. The different colors denote the different positions along the vertical axis of the LDK bar.

the linear elastic material, Alumina, to break down and suppress the acoustic resonances. It is to be noted that the dielectric loss of all materials is ignored here to focus on the effects of the low dielectric constant and related mechanical properties of LDK additives.

Layered: This approach divides the ferroelectric layer of the varactor into different parts in the longitudinal direction, as displayed in Figure 5.3a. Now, the acoustic resonances are generated due to thinner layers of ferroelectrics. The LDK composition corresponds to 10% of the whole composite varactor here. To analyze better behavior in a layered approach, the LDK layer is further divided, as shown in Figure 5.3b. Apart from this, the reliability of the suppression in this approach is inspected by moving the LDK bars at different positions along the longitudinal direction. This is visualized by moving the bar along the vertical axis from -0.5 mm to 0.5 mm in Figure 5.3a and similarly, in Figure 5.3b. The extracted ESR analysis of acoustic resonances is illustrated in Figure 5.3c. Upon observing and comparing with the without-inclusion model, it is witnessed that suppression is there, but it is restricted to specific positions in both the single and double LDK layer model. The colors of the line represent the different positions, and due to simplicity, all are superimposed on each other. Moreover, the double LDK layer is not much different regarding acoustic behavior than the single LDK layer. Although resonance peaks show better suppression in the 11 MHz and 20 MHz region, few positions make it worse to live up to the promise of reliable suppression. Collectively, the ESR in some positions is even higher than the model without inclusions, which remarkably reduces reliability with the layered approach in acoustic suppression. Hence, it is concluded that the division of the LDK layer in the longitudinal direction does not affect the acoustic behavior reliably and can not be considered for acoustic suppression. This makes a strong argument for including LDK in the form of columns and inspecting the suppression behavior.

Columnar: This approach also divides the ferroelectric layer of the varactor into different parts along the broad side, as portrayed in Figure 5.4a. This leads to acoustic resonances generation due to the narrower width of ferroelectrics. Similar to the layered approach, the LDK composition corresponds to 10% of the whole composite varactor. Additionally, to analyze better behavior in the columnar approach, the LDK layer is further divided, as displayed in Figure 5.4b. Again, the positional analysis of the LDK bar along the horizontal axis is important for the reliability of acoustic suppression. Hence, the LDK bars are placed at different positions from -1 mm to 1 mm, mentioned in Figure 5.4 for both configurations. Upon observing the acoustic behavior in the ESR graph, similar unreliable behavior of acoustic suppression is witnessed in the layered model above. Few positions of the LDK column depict acoustic suppression, but a reliable suppression can not be assured. After dividing the LDK column to examine the influence of ferroelectric column width, the acoustic activity has been suppressed completely with acoustic around 14 MHz

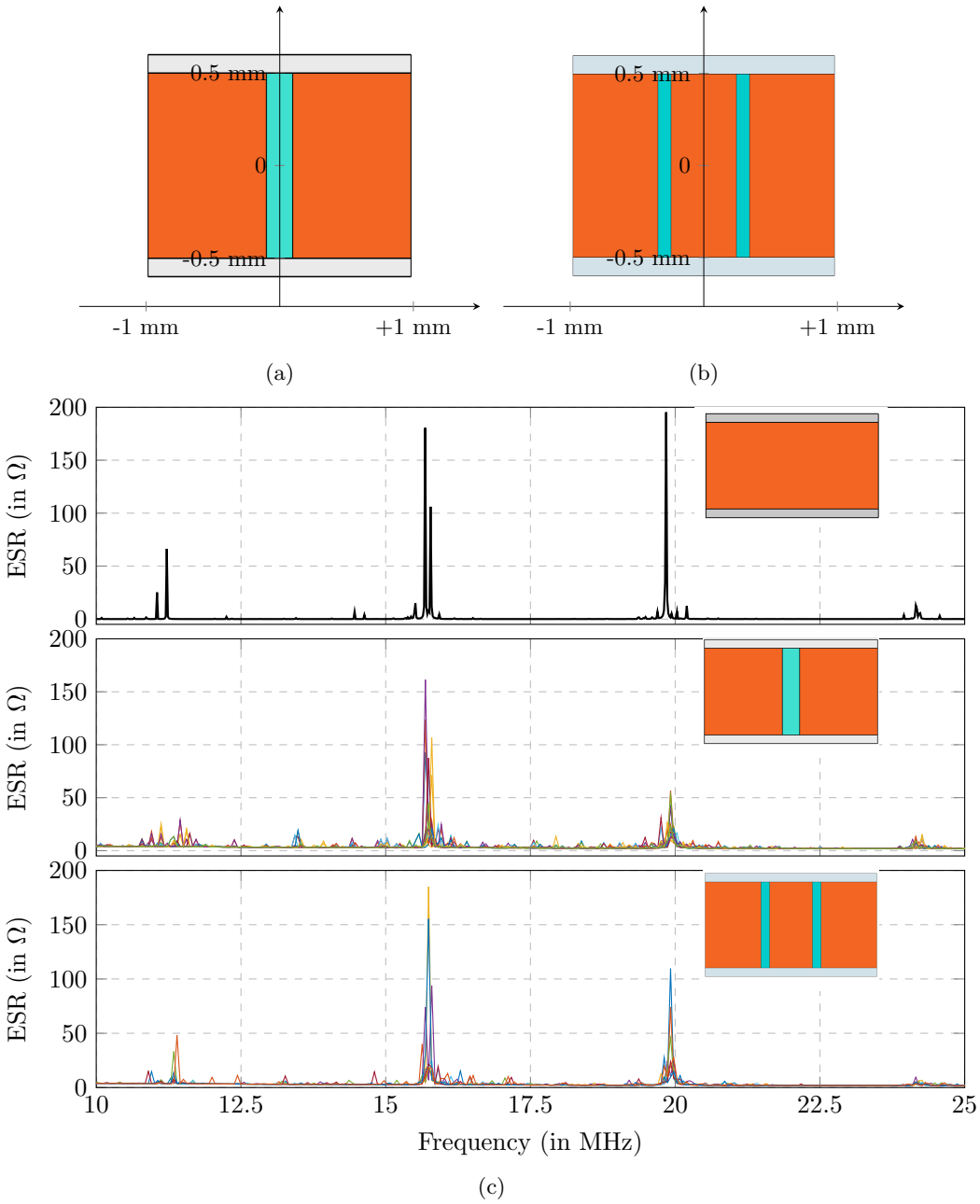

Figure 5.4.: Preliminary 2D model in the columnar approach, with (a) and (b) representing the single and double columnar configuration, respectively. In both configurations, the 10% LDK layer, in an additive composition, is placed along the horizontal direction at different positions to investigate acoustic suppression. (c) denotes the extracted simulated ESR vs. frequency in the columnar approach. The different colors denote the different positions along the horizontal axis.

and 18.5 MHz. But acoustic activities near 16 MHz and 21 MHz have increased in level. The main idea which is drawn from both approaches is that the mixture of both layered and columnar modeling is beneficial for the suppression of acoustic resonances. This made the basis for the next approach of LDK additives as inclusions, forming the mixture of the columnar and the layered approaches.

Inclusion: This approach considers LDK additives as several inclusions, which can be triangular, squarical, circular, or any other shape. The simplest one of all is the circular, as it has no edges, which ensures there are no corner effects. Figure 5.5 illustrates a model where the blue-colored circles represent LDK inclusions. Each inclusion is 0.16 mm in diameter, based on the observations from Figure 5.5f, for a 10 vol-% BST composite varactor. Moreover, each circle contributes around 1% of the 2D model varactor, representing 1% inclusion in the composite form. So, if a 3% composite varactor is needed, then three circles of this diameter are easily be placed in the BST region. Simultaneously, three configurations of 5, 10, and 30% LDK inclusion compositions are selected to demonstrate the incremental effects of additives inside mixtures, as portrayed in Figure 5.5. Compared with the layered and columnar approaches, the LDK additives are spread at random positions across the BST region. Thus, this approach gives the impression that it lies between the other approaches.

After setting the requisite physics and mesh settings, the ESR is extracted for three different random position arrangements for each composition. Figure 5.6 compares these extracted ESR with the extracted ESR from the model without inclusions. The significant reduction in ESR, for the peak around 15.7 MHz and 19.9 MHz, from around 200 Ω to under 70 Ω for all configurations of inclusions, demonstrates a considerable suppression of acoustic resonances, whereas an occasional suppression around 11 MHz acoustic resonance peak. Moreover, many additional resonance peaks are witnessed in the composites, which is acceptable, provided they remain under the level of suitable suppression. This level is taken less than 100 Ω in this model. There is a possibility of a few arrangements where the suppression is not reliable to show the viability of this model. Hence, it is imperative to follow the Monte-Carlo simulation analysis and statistically ensure the model's viability. Consequently, 100 simulations for each configuration with different non-overlapped random arrangements of LDK inclusions are carried out to prove the reliability of the acoustic suppression in the model with inclusions. The random arrangements are based on the uniform distribution of probabilities of the position of LDK inclusions across horizontal and vertical directions within the BST layer. Generally, the analysis of the indicative parameter, ESR over here, is concluded by the variance σ^2 and mean μ studies. The σ^2 helps to generate the consequence of the no. of simulations or random arrangements considered, and the μ helps in quantifying the adequate possible levels of the indicative parameter.

After simulating all the compositions, the μ of the extracted ESR is compared in

Figure 5.7. The μ shows extreme acoustic suppression of ESR values reducing from 200 Ω to around 25 Ω. However, due to the narrow bandwidth of the resonance peaks

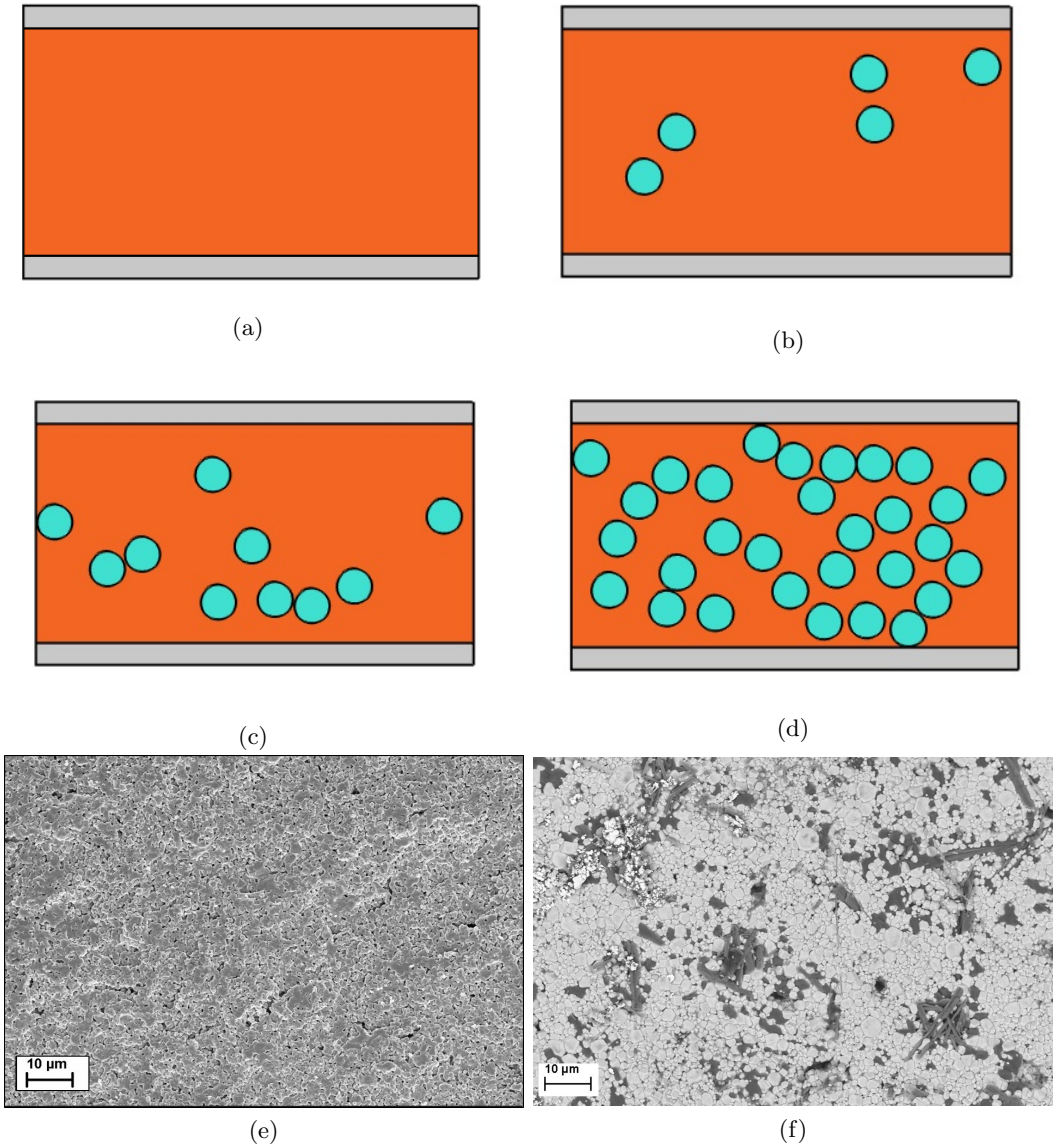

Figure 5.5.: Preliminary 2D simulation model design with BST (orange) between two silver electrodes (gray) with randomly placed LDK inclusions (blue): (**a**) without inclusions and (**b**–**d**) with 5%, 10%, 30% LDK inclusions in the BST region. Each inclusion is 0.16 mm in diameter. Microstructural analysis of realized 100 vol-% (e) and 90 vol-% (f) BST varactors. In the second BST varactor, 10 vol-% MBO is added, depicted with grayish-black color. Whereas the BST is displayed in white color.

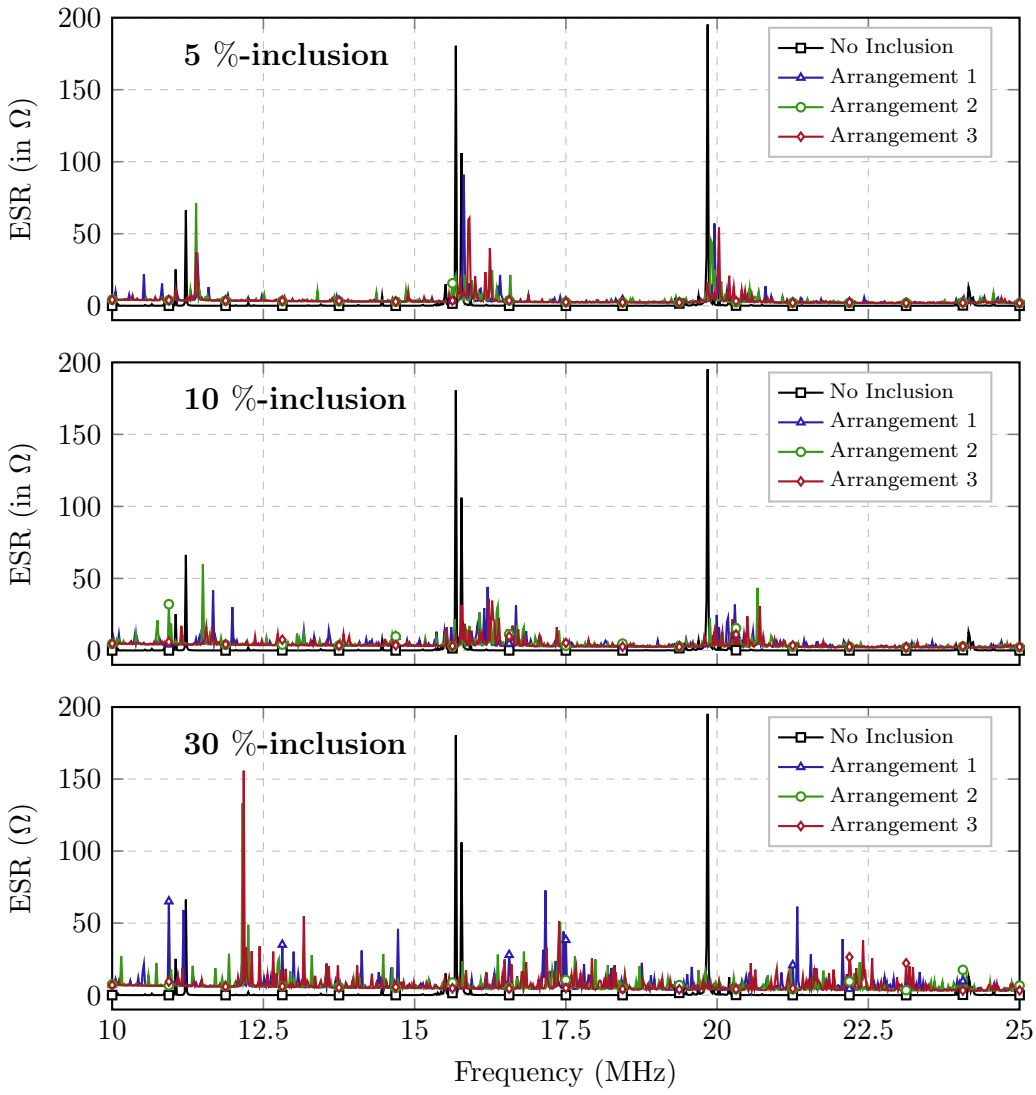

Figure 5.6.: Illustrations of ESR extracted from 2D simulation model with increasing composition percentages of inclusions for three random arrangements of each configuration. Upon observation, acoustic suppression is detected with increasing inclusion vol-% till 10 vol-%, but with 30 vol-% inclusion, the suppression is reversed. The acoustic frequency shifted towards higher frequencies suggesting the breaking of strong resonances into several weak resonances to suppress the amplitude of resonances.

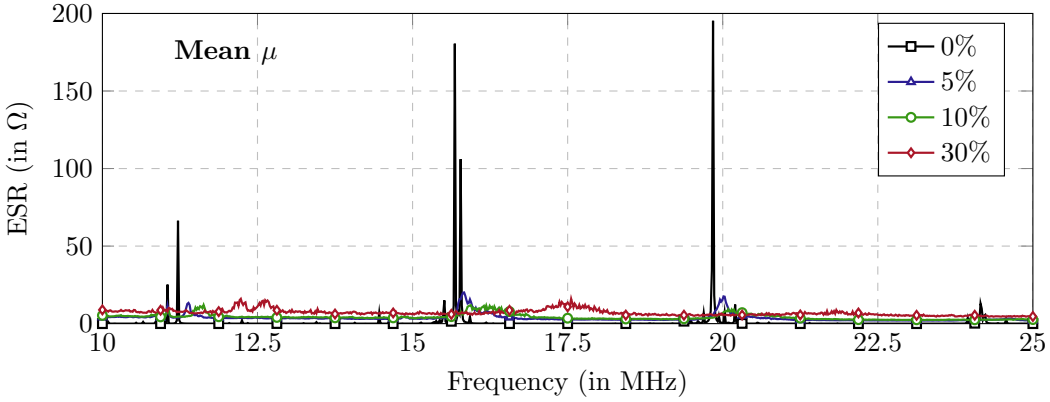

Figure 5.7.: Comparison of mean μ ESR extracted from preliminary 2D simulation model with increasing composition percentages of inclusions. Considerable suppression of acoustic resonances is detected with a tolerable increase in ESR at non-acoustic frequencies.

and varying resonating frequencies in the inclusions model, the outlier ESR values can be ignored. Hence, σ^2 spread and levels are needed to include the influence of these outliers towards extreme ESR values possible, which is also witnessed in Figure 5.6. Additionally, σ^2 spread and levels include the influence of frequency shifts of resonance peaks in the model with inclusions. While accumulating the simulations, a cumulative σ^2 of the extracted ESR for the inclusions model is recorded and is illustrated in Figure 5.8. It is observed that with the increasing number of simulations with different arrangements of inclusion, the spread of extracted ESR reduces, and the simulation environment becomes saturated with further changes in the spread of ESR for all the compositions. In fact, cumulative variance for 50 and 100 simulations is almost similar for 5% and 10% inclusion composition, suggesting the 50 simulations are enough to gain reliable insights for suppression in these compositions. Whereas, for 30% inclusion composition, 100 simulations are required to gain the acceptable level of the settlement of the σ^2. Therefore, 100 simulations are considered to ensure definite or reliable suppression of the acoustic resonances. It should be noted that the narrow bandwidth of acoustic resonance peaks and small shifts in acoustic resonance frequencies with different arrangements are the reason for the high variance here.

The σ^2 spread of all the simulations for each inclusion composition is depicted in Figure 5.9, and it is the minimum for a 10% inclusion configuration at all the frequencies. This denotes that the 10% inclusion configuration shows less influence from microstructural changes with the different arrangements of inclusions. It is deduced that a trend of increasing suppression with increasing inclusion's composition until around 10 vol-%, followed by the receding acoustic suppression with the increased levels of σ^2 for 30 % inclusion composition.

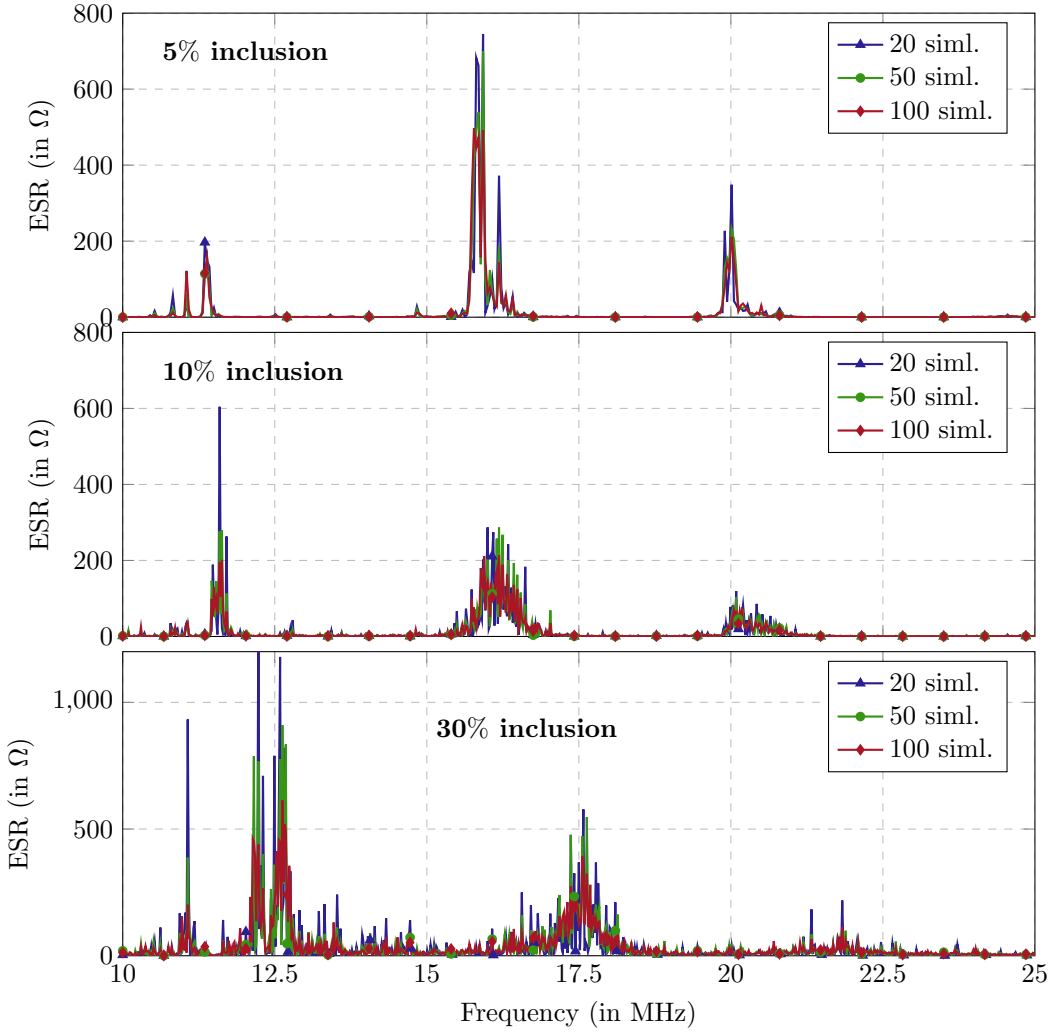

Figure 5.8.: Cumulative comparison of variance σ^2 of ESR extracted from preliminary 2D simulation model with the increasing number of simulations of each inclusion composition. For 5% and 10% inclusion composition, the σ^2 settle down with 50 simulations. Whereas, for 30% inclusion composition, it settles down at 100 simulations.

Finally, the extracted ESR for the model without inclusions is compared with the statistically adjusted extracted ESR of each inclusion composition, as illustrated in Figure 5.10. For comparison, the upper bound limit of the extracted ESR from the model with inclusions is considered. The upper bound is stated by the μ of 100 simulations with the addition of $3{\cdot}\sigma$, assuming the extracted ESR varies according to normal distribution. This upper bound limit, statistically, considers the 99% confidence interval of the extracted ESR values for each frequency point in all the

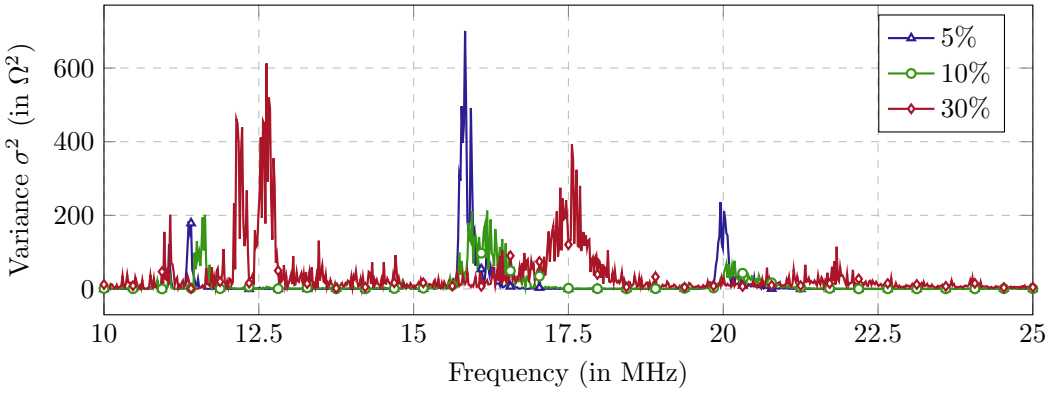

Figure 5.9.: Comparison of variance σ^2 of ESR extracted from preliminary 2D simulation model for 100 simulations of each inclusion composition. For 10% inclusion composition, the σ^2 demonstrates the best results with the least outliers simulations. With increasing LDK inclusions, the acoustic resonances suppression increases but decreases again with a further increase in inclusions.

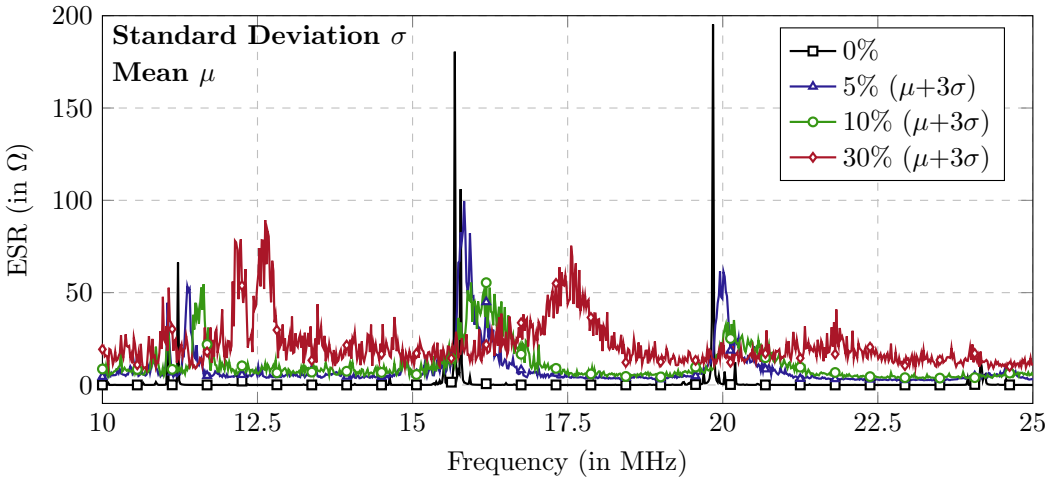

Figure 5.10.: Comparison of ESR extracted from the preliminary 2D simulation model with increasing composition percentages of inclusions. Here, the upper bound limit (99% confidence interval) of ESR from the mean μ and the standard deviation σ is considered, and the lower bound is ignored. Considerable suppression of acoustic resonances is observed here, with a tolerable increase in ESR at non-acoustic frequencies. A shift in frequencies of acoustic resonances to higher frequencies is also present with increasing amounts of inclusion's composition.

simulations considered for each inclusion composition. The reduction in ESR, for the peak at around 15.7 MHz and 19.9 MHz, from around 200 Ω to 100 Ω for all configurations of inclusions, ensures the considerable suppression of acoustic resonances. This suppression effect of around 11.3 MHz and 24.1 MHz is limited due to the rise of new small resonances as a consequence of microstructural changes, with different arrangements for all inclusion compositions. However, with the 30 vol-% inclusions, these acoustic resonances are more pronounced. In conclusion, when comparing all the inclusion configurations, the extracted ESR and microstructural influence with different arrangements is least for the 10% inclusion composition than the other inclusion compositions for the whole range of considered frequencies. In fact, a similar trend of the increasing and then decreasing suppression of acoustic resonances with the increase in inclusion's composition is witnessed here. This leads to the 10% inclusion composition being selected as the most appropriate choice for the experiment among the three compositions of inclusions considered.

As the realized varactor is in a different geometric form than the preliminary 2D model, as portrayed in Figure 5.11, the model geometry is modified, displayed in Figure 5.12. The modified geometry becomes more complex and requires more

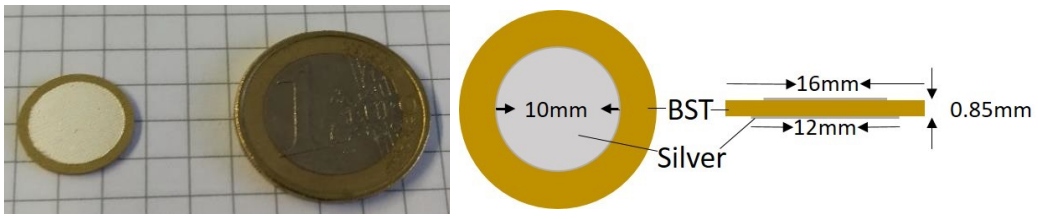

(a) (b)

Figure 5.11.: The realized varactor used in this work in (a) and its dimensions (b).

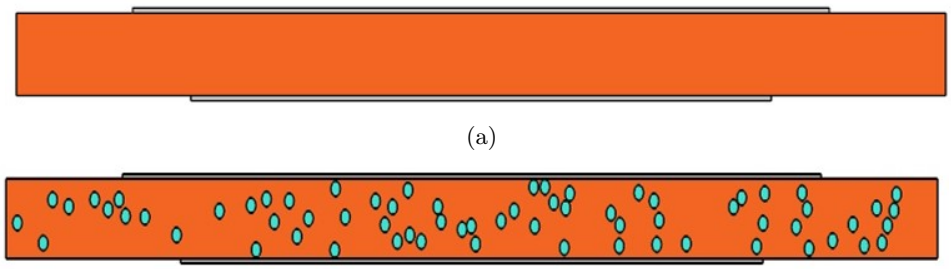

(a)

(b)

Figure 5.12.: Modified 2D simulation model to adapt the realized varactor. (a) and (b) are the model without and with 10% LDK inclusions (blue), respectively. The electrodes are 0.01 mm thick, and the BST (orange) region is 16 × 0.85 mm^2 in dimensions close to the measured dimensions of the realized varactors. Similar to the preliminary 2D model, each inclusion is 0.16 mm in diameter.

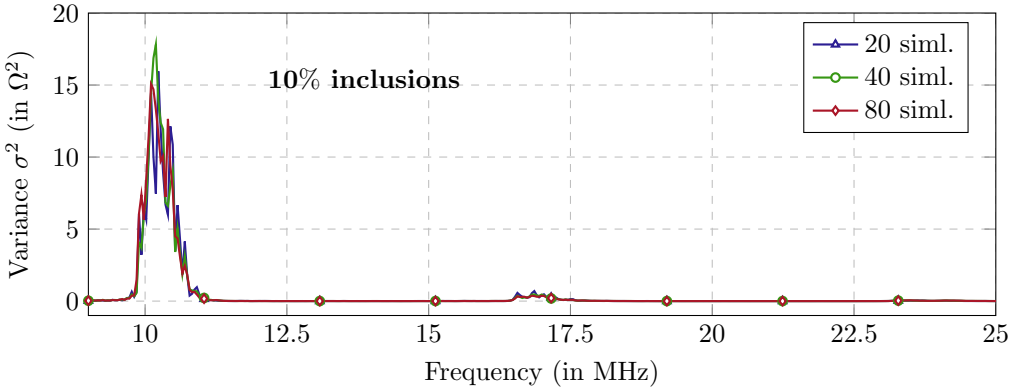

Figure 5.13.: Cumulative comparison of variance σ^2 of ESR extracted from the modified 2D simulation model with the increasing number of simulations in 10% inclusion composition. The σ^2 adequately settles down with 40 simulations, although, for definitive suppression behavior, 80 simulations with different random arrangements are executed.

inclusions to cover the required inclusion composition in the BST region. The realized varactor's widest cut slice, as shown in Figure 5.11b, is assumed for the 2D simulation environment to consider the effects of its crucial dimensions. Moreover, it has already been illustrated above in the preliminary 2D model in Figure 5.10 that the suppression behavior is better in 10% inclusion composition. Hence, only

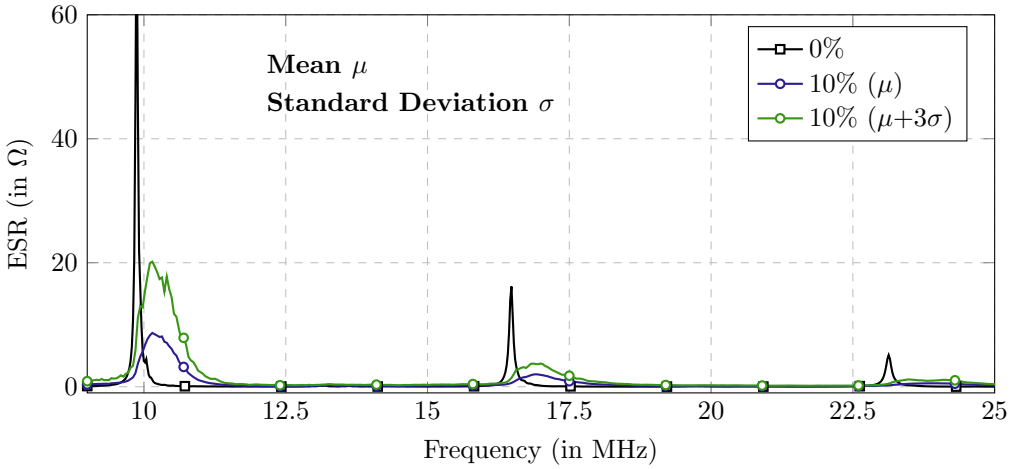

Figure 5.14.: Comparison of extracted simulated ESR statistics from a modified 2D simulation model of 10% inclusion composition. The upper bound limit $\mu + 3\sigma$ and μ of extracted ESR of 10% LDK inclusion configuration for 80 simulations are compared with the no-inclusion model. A similar acoustic resonances suppression is present compared to the preliminary 2D simulation model discussed earlier.

10% inclusion composition is considered in the modified 2D model form. This modified model is simulated with similar physics settings as the preliminary 2D model and appropriately updated mesh settings to demonstrate the acoustic suppression behavior expected in the realized varactor geometry.

Similar to the preliminary 2D model, a number of simulation investigations are executed with different arrangements of inclusions. Hence, a cumulative ESR variance distribution σ^2 is extracted according to the number of simulations, illustrated in Figure 5.13. Upon observation, the influence of the number of simulations can be ignored as there is a negligible difference in the three cumulative variances. This deduces that due to an increase in the number of inclusions, to maintain the requisite composition in the modified varactor, the random arrangement's influence is decreased. Hence, the modified model becomes independent of different random arrangements of inclusions, and even one such arrangement is capable of producing reliable results. Moreover, this also concludes that apart from the size of inclusions, the minimum number of inclusions is influential in reducing the effects of random arrangements of inclusions. Additionally, the influence of the phase or conglomerate size of LDK inclusion on acoustic resonances in comparison with the whole varactor size plays an important role in deducing acoustic resonances suppression.

Ultimately, the simulated ESR of both, with inclusions and without inclusions, is shown in Figure 5.14. Here, the upper bound limit of the extracted ESR for the modified 2D model with inclusions is compared with the modified 2D model without inclusions. The distinct acoustic resonances are observed at around 9.9 MHz, 16.5 MHz, and 23.1 MHz. Additionally, the acoustic resonances are placed at an equal difference of 6,6 MHz, suggesting harmonic resonance behavior. The main advantage of the modified 2D model is the position of the acoustic resonances in the frequency range, which is expected to match the extracted measured ESR. Hence, in the next section, the measurements are evaluated and compared with these simulated results.

5.3. Evaluation and Prediction of Acoustic Resonances

As the focus is mainly on plasma applications during this work, the main requirement is to maintain higher operating temperatures of around 40-50 °C. This is mainly due to excessive heat dissipation during the plasma ignition interval. Concerning this, the ratio of barium to strontium in BST is chosen so that its Curie temperature (T_C) is around 20 °C. The difference in temperatures ensures that the BST stays in the non-polar or paraelectric phase, despite the slight temperature variations in the vicinity of the setup. As already stated in previous chapters, the BST $Ba_{0.7}Sr_{0.3}TiO_3$ has a relative permittivity of more than 2000 and shows a Q-factor of around 100 in the lower MHz range, as seen in Figure 5.15. Hence, a low-loss LDK Magnesium Borate $Mg_3B_2O_6$ (MBO) is chosen as an additive, as has already been discussed in Section 2. Small-signal characterization is performed from 10 MHz to 25 MHz with a

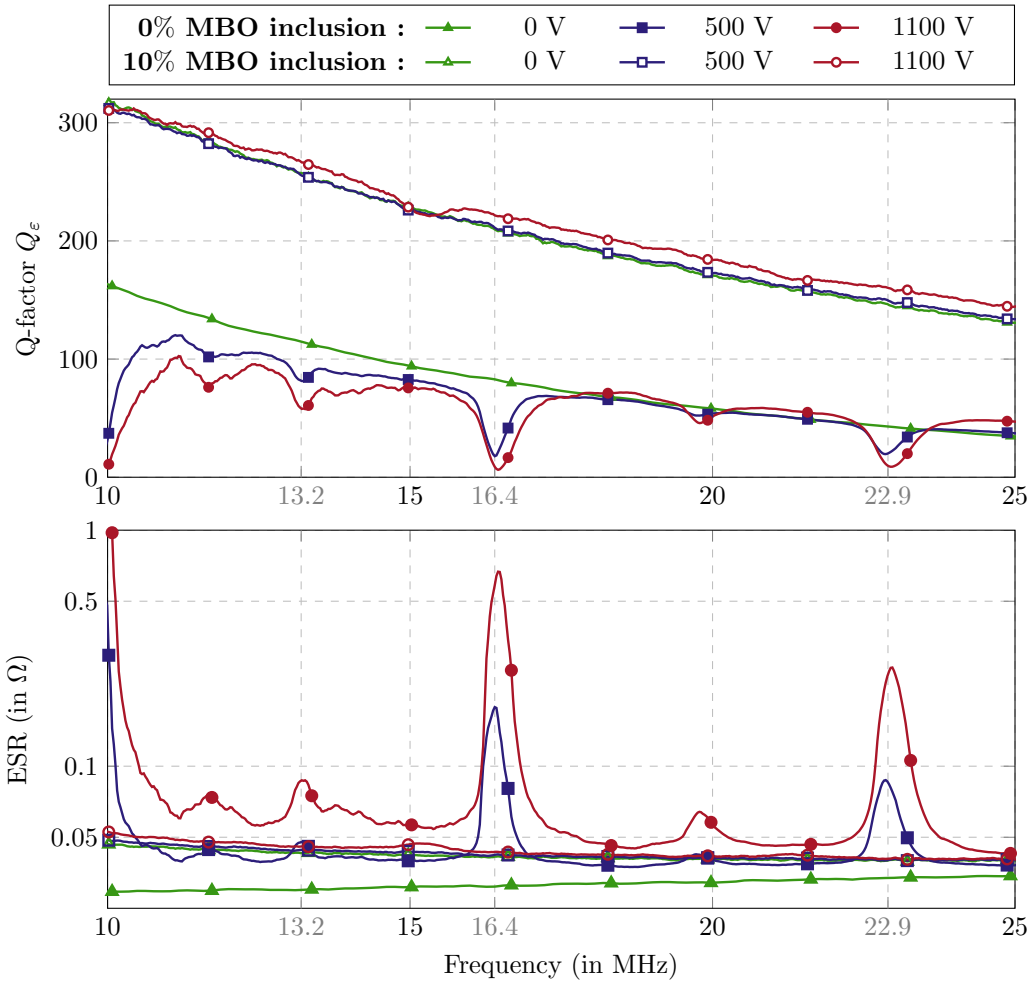

Figure 5.15.: Extracted material values from measurements: Q-factor (top) and ESR (bottom) with bias electric fields from 0 kV to 1.1 kV.

Keysight Impedance Analyzer E4991B as discussed in Chapter 3. The schematic of the measurement circuit is depicted in Figure 3.4d. DC bias voltages up to 1100 V are applied using a Keithley 2410 Sourcemeter. The maximum electric field of around 1.29 kV/mm is generated across the varactor. Prior to every measurement, the setup is calibrated by standard short, open, and load (SOL) calibration at the end of the biasing circuit, and the DC bias source was switched on at 0 V. The extracted capacitance, ESR, and Q-factor readings of the varactor are taken directly from the Impedance Analyzer. Figure 5.15 compares the extracted Q-factor Q_ε and ESR from measured values for both compositions with respect to frequency, respectively. A significant presence of acoustic resonances in 0% MBO inclusion varactor is observed at 13.2 MHz, 16.4 MHz and 22.9 MHz, which decreases the Q-factor with increasing bias voltages. In comparison, an almost complete suppression of acoustic resonances

is observed at any bias voltage applied in the 10% MBO varactor. The ESR shows the same behavior, as predicted in the simulation environment earlier, shown in Figure 5.14. Due to the simplification with no dielectric losses, the simulation model cannot extract the absolute magnitudes of extracted ESR. The comparison is only made for the relative changes. In terms of the position of acoustic resonances in the frequency range, the distinct acoustic resonances are present at similar frequencies of around 10MHz, 16.4 MHz and 22.9 MHz, confirming the simulation model's viability. The difference in the distinct acoustic frequency position is around 6.4 MHz, which also conforms with the modified 2D simulation model.

Moreover, the unbiased Q-factor Q_ε is increased from around 120 to 270 at 13.2 MHz, denoting the decrease in dielectric loss. The shift in ESR peaks over frequency is not noticeable, which is suspected to be due to the low dielectric loss of MBO, further increasing the Q-factor and reducing the ESR values. Some small

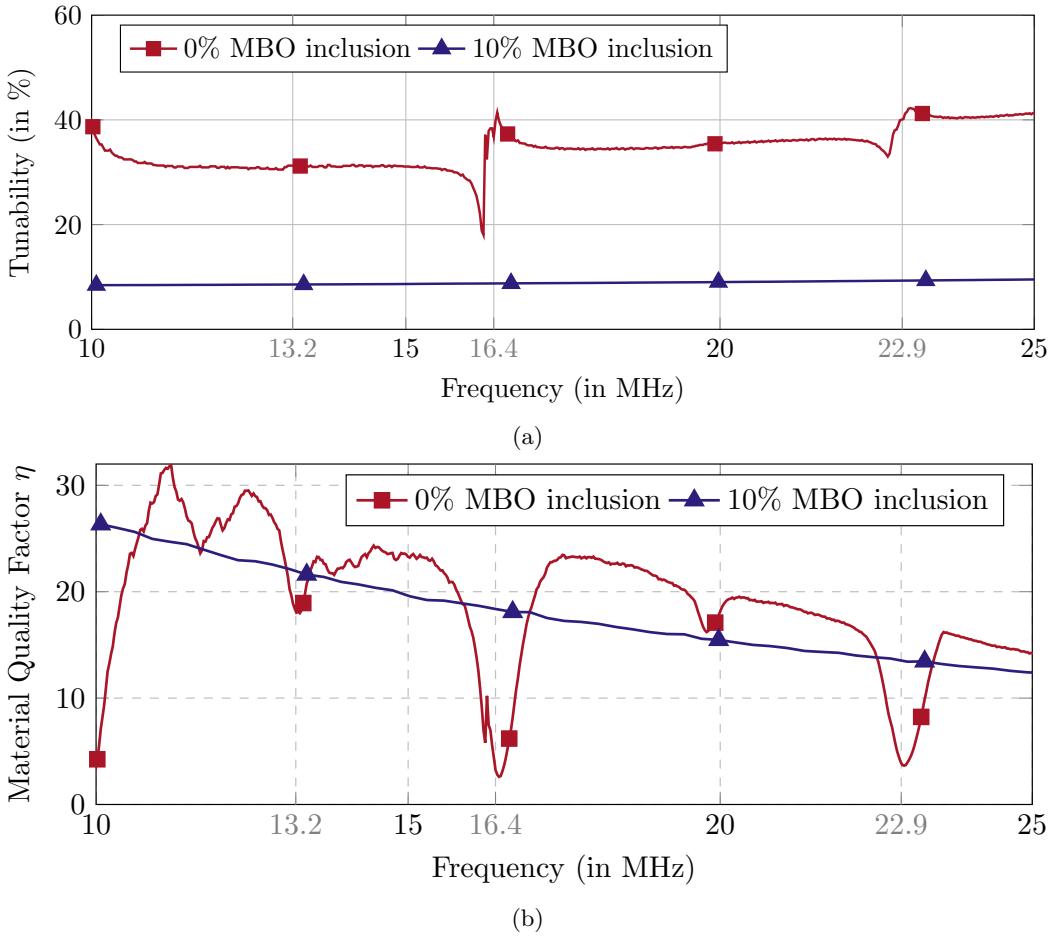

Figure 5.16.: Extracted material values from measurements: tunability (a) and material quality factor (MQF) at maximum bias electric fields around 1.1 kV.

dips, such as the one around 15 MHz, in the Q-factor, are visible in the 90% MBO varactor, but nothing conclusive can be stated from these. As discussed in [Wie+17], the extracted capacitance values are directly proportional to the extracted relative permittivity for the cylindrical disk capacitor used in this work. This leads to the conclusion that the capacitance tunability τ_C equals the permittivity tunability τ_ε and is defined as

$$\tau_\varepsilon = \frac{\varepsilon(0) - \varepsilon(V)}{\varepsilon(0)} = \frac{C(0) - C(V)}{C(0)} = \tau_\mathrm{C}, \tag{5.5}$$

where $\varepsilon(V)$ and $C(V)$ are the relative permittivity and capacitance at voltage V, respectively. τ_ε decreases from around 30% to 10%, as shown in Figure 5.16a. The reduction in τ_ε is observed to be larger than expected and is certainly not comparable to the elevation in Q_ε, which is suspected to be due to the formation of a third non-tunable phase due to ionic exchanges between BST and MBO, which is suspected to be $MgTiO_4$, as discussed in previously in Chapter 4 as well as in [She+20]. The same behavior is also witnessed with the non-biased capacitance, as the value decreases from around 3.58 nF to around 1.11 nF with the introduction of MBO. The figure-of-merit is taken as the material quality factor η [Gie09], which is defined as

$$\eta = \min(Q_\varepsilon) \cdot \tau_\varepsilon, \tag{5.6}$$

as shown in the Figure 5.16b. At 16.4 MHz and 22.9 MHz, a significant improvement in η is observed for the 10% MBO varactor over 0% MBO varactor. However,

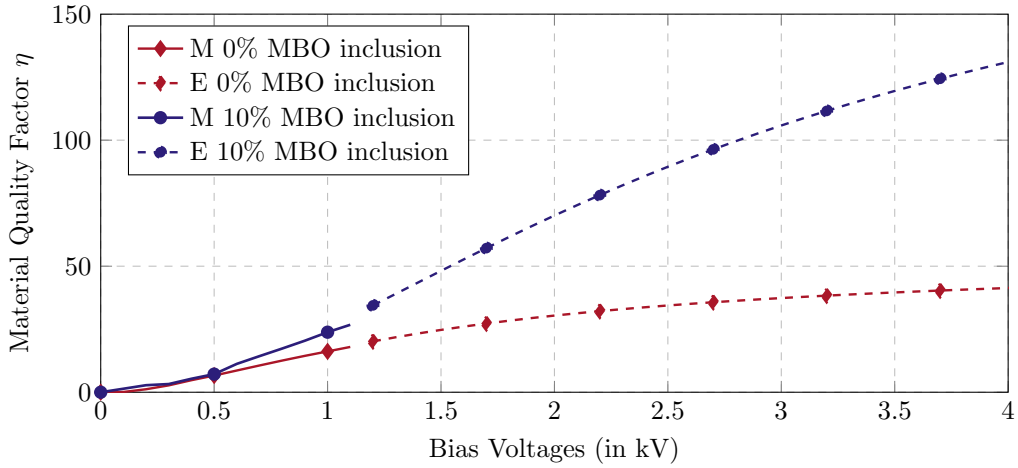

Figure 5.17.: Extracted material quality factor: (M) from measurements with bias electric fields from 0 kV to 1.1 kV and (E) from the extrapolated measurements with bias electric fields from 1.1 kV to 4 kV.

the interference from the strong acoustic resonances is present at these frequencies, which not only degrades the η, but also shows a distinct resonance effect in tunabilities. At 13.2 MHz, the η is slightly better for the 10% MBO varactor in comparison, but it is expected to improve for bias voltages above 1.1 kV, as shown in Figure 5.17 with the dashed line. These dashed tunabilities, in the extracted η, are extrapolated by using measured data in the model by Chase et al. [CLY05], as shown in

$$\varepsilon_r(V) = \frac{\varepsilon_r(0)}{2\cosh\left[\frac{2}{3}\cdot\sinh^{-1}\left(\frac{2V}{V_2}\right)\right]-1}, \tag{5.7}$$

where $\varepsilon_r(V)$ is the calculated permittivity at bias voltage V, $\varepsilon_r(0)$ is the unbiased permittivity and V_2 is the bias voltage at which 50% tunability is achieved. V_2 is the fitting parameter from the extracted measured values of relative permittivities between 0 V and 1.1 kV, which is around 1.9 kV and 4.1 kV for the 0% and 10% MBO varactor, respectively. However, the minimum Q_ε is set as identical to those in the Figure 5.15, producing the best-case for the 0% MBO varactor at the bias voltages above 1.1 kV. Although, Q_ε does not show significant acoustic degradation for the 10% MBO varactor. It is thought that this may appear when increasing the voltage from 1.1 kV to 4 kV, which is also not considered while calculating the composite varactor's extrapolated η.

6. Conclusion

With an enormous increase in RF devices in lower GHz range, new alternative technologies are taking shape at higher frequencies up to 65 GHz. Additionally, the smaller sizes of the RF components in the large and dynamic RF sensor networks introduce space constraints. Consequently, these device's critical dimensions reach atomic boundaries (≈100 Å). The imperfections, or roughness of the surface atomic layer, contribute to these RF device's performance significantly. Hence, atomic layer etching (ALE) has gained much attention recently. The implemented plasma processes in such etching techniques are prone to colossal impedance mismatch during the transition between different intervals. A dynamically tunable RF matching is used to maintain the requisite amount of RF power transfer and prevent reflections due to impedance mismatch. Traditionally, L-match circuits are implemented, using mechanically tunable varactors based on the parallel-plate topology with vacuum as dielectric. But they provide limited tuning speeds of minimum 1 ms for a relative change in capacitance. This becomes a bottleneck due to the reduced plasma ignition and extinction phase times with reduced thickness of the etched material layer. Various alternatives can be considered, which include semiconductor varactor diodes, PIN-diode switched capacitor banks, microelectromechanical systems (MEMS) based solutions, and varactors based on ferroelectrics.

The ferroelectric BST-based varactor approach is chosen due to its extremely fast and dynamic tuning under the influence of bias electric fields. In recent years, BST has been one of the most studied tunable ferroelectric, where the tunability is generated from the displacement of titanium ions in the lattice. This is the reason for the high tuning speed in the μs range. Additionally, this varactor provides high linearity and power-handling capabilities, which match the standards of mechanically-tuned varactors. However, this varactor has a Q-factor Q_ε around 100 in the intended ISM (industrial, scientific, and medical) frequency range, which is insufficient for the intended plasma applications. Additionally, the presence of electrostriction-induced piezoelectricity decreases the varactor's performance. Due to this, the generated mechanical energy interferes with the electrical domain, thereby reducing Q_ε. Therefore, a composite approach is adopted to minimize the dielectric loss and the loss due to induced piezoelectricity due to acoustic activity. In the literature, numerous works discuss the modeling of dielectric loss and its reduction in the composite ferroelectric varactor. Still, hardly any literature can be found in acoustic resonances suppression. Since the early 2000s, tunability modeling has been studied quite expensively. Still, it could not explain the heavy reduction of tunability due to the replacement of

ferroelectrics compared to the decrease in dielectric loss. The previous models also lacked the precision and accuracy to match the experiments. Therefore, this work focuses on these two open areas in detail. The first model concentrates on complete electromagnetic tunability, and the second on suppression of acoustic activity in the BST-based bulk ceramic composite varactors.

The BST-based varactor generally exists in three technologies, namely – thin-film, thick-film, and bulk ceramic. The bulk ceramic exhibits large capacitance values leading to high power handling capabilities of up to 4 kW, which are required in the plasma application environment. Additionally, as the focus is on the characterization of the BST composite materials, the bulk ceramic in parallel-plate capacitor topology demonstrates better field distribution throughout the composite material layer. In fact, due to the interconnected grain structure owing to high densification in bulk ceramics, the permittivity and the tunability are high, with less dielectric loss. In the composite form, Magnesium Borate $Mg_3B_2O_6$ (MBO) is chosen as the additive for the BST composites for its extremely low dielectric loss ($Q_\varepsilon \geq 2000$) and linear elastic properties. Moreover, MBO is also crucial in reducing sinter temperatures from around 1350 °C to around 1100 °C.

Tunability Modeling

A complete electromagnetic tunability CAD-3D model is presented, which is executable for a full range of volumetric compositions of BST and MBO. The model consists of 1000 cubical phases, each belonging to BST or MBO. The relative permittivities ε_r of BST and MBO are 2000 and 7, respectively. Depending on the volumetric compositions of BST and MBO, each one is assigned requisite phases. All simulations utilize the electrostatic solver of the Simulia CST Studio, with the input bias electric field similar to the experimental applied bias field of 1100 V/mm. The distinctive feature of this model is the precise consideration of the distribution of the bias electric fields at an optimum mesh configuration. Using these bias electric fields, each BST solid in the respective mesh cell is then tuned to an updated ε_r. The revised ε_r is calculated using Weil's equation of tunability, which provides a better fitting with experimental extraction of the critical indicators such as tunability and capacitance of the 100 vol-% BST varactor. After simulating the untuned and tuned model, the tunability is calculated for the composite varactor. Similarly, the process is repeated for various BST and MBO mixture volumetric compositions. Due to size differences between the model and the realized varactor, the comparison is made with the tunability indicator. The experimental electrical characterization is done at room temperature and 13.56 MHz, which leads to the use of BST in the $Ba_{0.6}Sr_{0.4}TiO_3$ stoichiometric ratio. As the main objective of the model is to compare tunabilities, the room temperature here ensures fewer variations due to higher temperatures, which are expected in intended plasma applications.

Upon comparing the modeled and experimental-extracted tunabilities, a huge de-

viation is witnessed. For example, for the 80 vol-% BST composite varactor, the simulated and measurement extracted tunabilities are around 40% and 8%, respectively. Similar observations are made in the other compositions, and the model requires additional degrees of freedom to consider the material changes with the mixing. Consequently, microstructural studies are performed using SEM equipped with an EDX setup for an elemental distribution scan from the BST region to the MBO region. It is noted that a significant amount of Ti^{4+} ions is leaked into the MBO region, which is responsible for high BST tunability loss. This effect is termed the substitution effect in this work. In the literature, this substitution effect is directly proportional to Curie Temperature T_C shifts in the composite varactor. Considering this, T_C of the various compositions is extracted by using an in-house manufactured thermal characterization setup. For the 100 and 80 vol-% BST varactor, T_C is recorded to be around 3 °C and −20 °C, respectively. This T_C-shift is not covered in the electromagnetic simulation environment, and a solution is devised to include these shifts. The simulations are updated by modifying the input of Weil's equation of tunability. Here, the input of 100 vol-% BST varactor is measured at the shifted temperature, where the shift is the same as the respective composition's T_C-shifts. After this revision, the simulated and measurement extracted tunabilities conform, evident from the tunability difference from 32% down to 2% for the 80 vol-% BST composite varactor. Moreover, due to the limitation of achieving a minimum temperature of −30 °C only, with the thermal characterization setup, the T_C-shifted simulation is available till 40 vol-% BST composition. Nevertheless, the reason for the huge deviation is precisely explained, and the simulation with T_C-shifts modification demonstrates the viability of the simulation model. This model is the first such model that predicts the BST-MBO mixtures tunability with such proximity to experiments. This model presents a flexible solution and is also expected to hold applicability in other ferroelectric-dielectric systems.

Acoustic Resonances Suppression Modeling

Most of the electromechanical applications are based in the non-polar or paraelectric phase due to the absence of remnant polarization. But electrostriction is imminent, which induces piezoelectricity and, thus, acoustic activity. Physically, the displacement of the Ti^{4+} ions in the BST crystal with the application of bias electric fields leads to electrostrictive strain. The proportional mechanical energy due to this ionic displacement generates acoustic waves when excited with RF. A portion of this mechanical energy is reflected back to the BST layer at interfaces to adjacent layers, forming standing waves or acoustic resonances. Consequently, these acoustic resonances interfere with the electrical signals in the RF domain due to energy conservation, decreasing the varactor's Q_ε or increasing equivalent series resistance (ESR). In this work, the origins of such acoustic activity are detected in the non-polar phase of the bulk ceramic-based BST varactor. A solution is modeled to remove or suppress them, which is then verified with experiments. The model is set up in COMSOL

Multiphysics, as it integrates RF and structural mechanics domain for piezoelectric materials, which are used to imitate the induced piezoelectricity of the BST layer in the non-polar phase of the designed varactor.

Theoretically, a directly proportional relationship are established between the induced piezoelectricity coefficient D and the permittivity and the bias electric fields. This suggests that with the reduction in relative permittivity ε_r of the BST layer, the induced piezoelectricity is reduced, thereby, the effects of acoustic resonances under the influence of high bias electric fields. Consequently, a low dielectric constant (LDK) and a linear elastic material, MBO, are added to the BST layer to reduce the acoustic resonances. As the mechanical properties of MBO are not known, another LDK, Alumina (Al_2O_3), is used in the simulations, which is defined in the COMSOL. In contrast, the BST layer's mechanical properties are adjusted according to the $Ba_{0.7}Sr_{0.3}TiO_3$ stoichiometric form, which is chosen to adapt to the heated environment of the plasma applications.

A quasi-complete suppression of acoustic resonances is witnessed in a BST-MBO varactor, in both, the simulations and the measurements, at the cost of tunability due to decreased amount of tunable material BST and other material and structural damages. According to the amount of composition, 10% MBO inclusion demonstrates effective suppression in simulations, and hence, is selected for experiments. Upon comparison, the acoustic resonance frequencies accurately match in the simulations and measurements. However, the suppression in amplitude is present in both but cannot be compared quantitatively due to the exclusion of dielectric loss in simulations. In a nutshell, the reduction of ESR from more than 60 Ω to around 10 Ω in the simulations, whereas in the measurements, minimum Q_ε increases from about 5 to 300 at around 10 MHz, depicts the strong suppression of acoustic resonances. On the contrary, tunability falls from 32% to around 10%, and a better material quality factor η for bias voltages up to 1.1 kV has further strengthened the use of BST-MBO varactors. The trade-off between the Q_ε and the tunability benefits low-loss varactors, where the tunability remains acceptable. Overall, the acoustic resonances are entirely suppressed, making the operation of the BST-MBO varactor possible for a wide range of frequencies and independent of the spectral shift of acoustic resonances. The spectral shift of acoustic resonances happens due to differences in thickness and material density of the varactor during fabrication, which hinders a reliable operation.

Further, according to the material quality factor η from both models, the 50 or 60 vol-% BST varactor stands out in the overall performance comparison. Although, a better acoustic suppression in the 10 vol-% BST varactor with better tunability makes them more valuable for the intended plasma applications. Using these sophisticated models, tunable impedance matching networks with extremely low overall losses and decent tunability is achieved, which find their applicability in plasma systems. Moreover, these models are powerful tools to engineer novel tailored composite materials, promote accurate design of functional material-based circuits and

systems. Hence, other application fields in RF communication such as sensors, tunable filters, phase shifters, or antenna matching networks of base stations, where ferroelectric composites are used, could significantly be improved with this work. Since most of these devices employ a planar approach in the form of thick and thin films, implementing the above models would be desirable. Another interesting outlook for expanding this work would include a tertiary phase apart from BST and MBO. This tertiary phase can be another dielectric or conducting additive. The dielectric additive may reduce the effects of Ti^{4+} leakage, whereas conducting additives, such as metal dopants (Ag^{+}) and indium tin oxide (ITO), are expected to interconnect the ferroelectric grains better (see Appendix A.3). Both solutions are expected to increase tunability by keeping the Q_{ε} still similarly low.

A. Appendix

A.1. Graphical Abstract - Electromagnetic Tunability Model

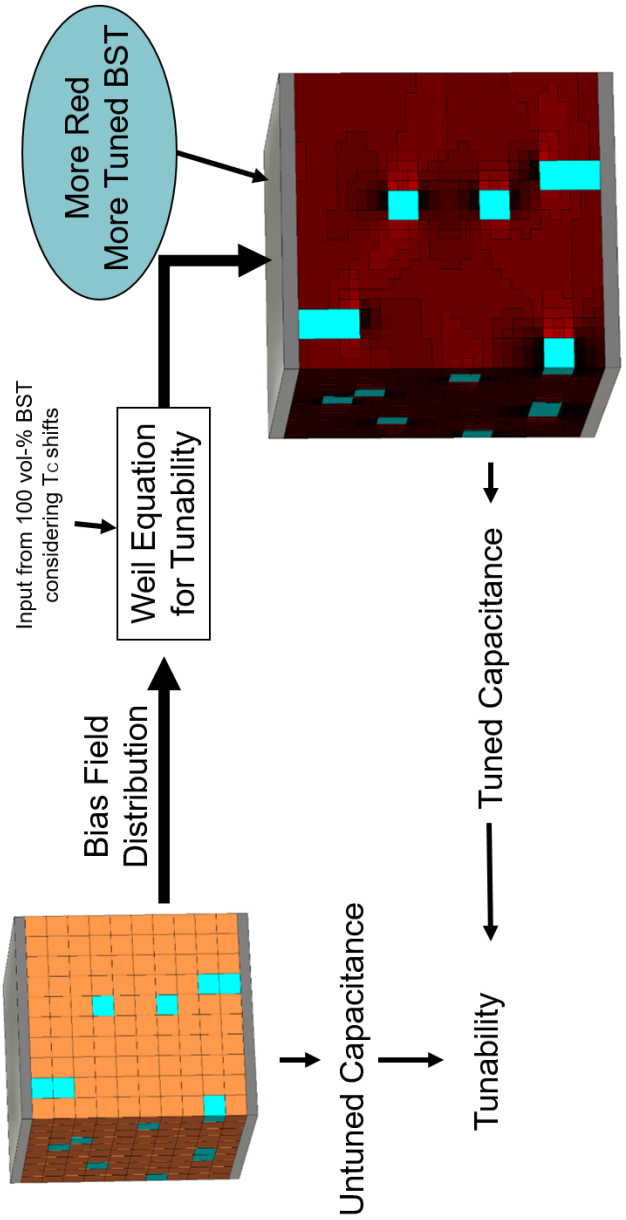

A.2. Graphical Abstract - Modeling of Acoustic Resonances

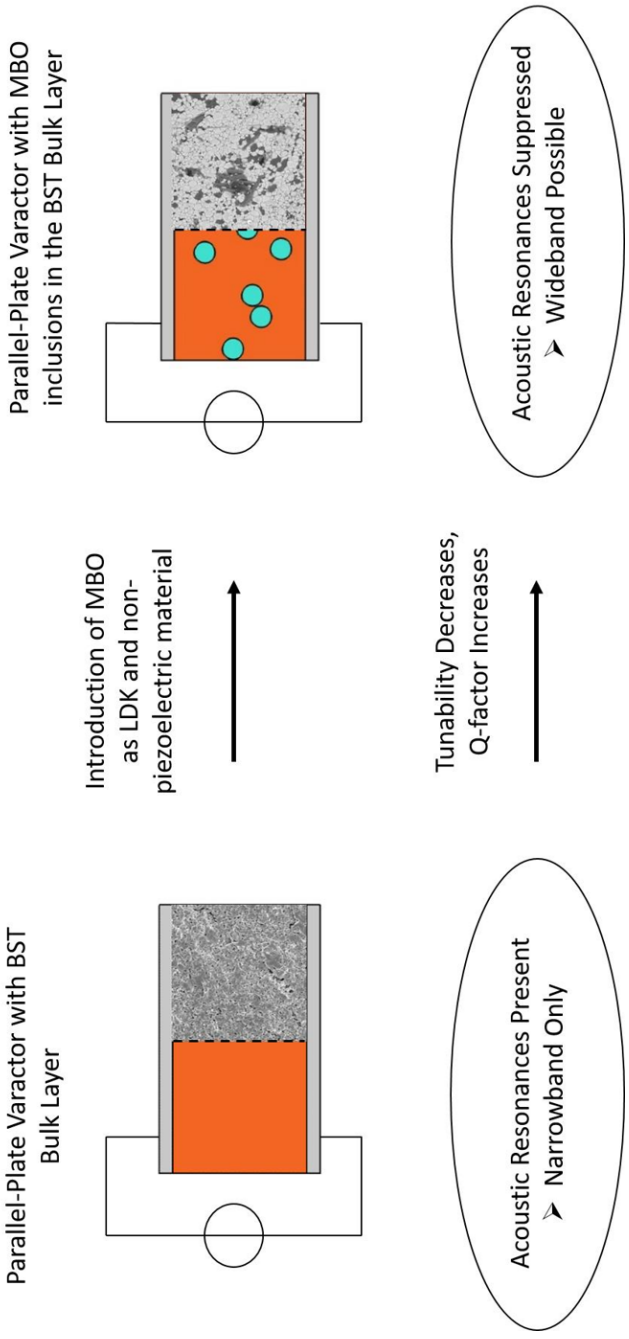

A.3. Tertiary Modelling with MBO and Metallic Additives

A substantial reduction in tunability is witnessed in the BST-MBO composites. A third material, such as metallic inclusion (Ag^+) or conducting oxides (ITO) addition, is proposed to counter this reduction. Figure A.1 depicts a symbolic representation of such composites. The main idea is to increase the electric field inside the BST material to extract more tunability without compromising the composite's excellent dielectric loss properties.

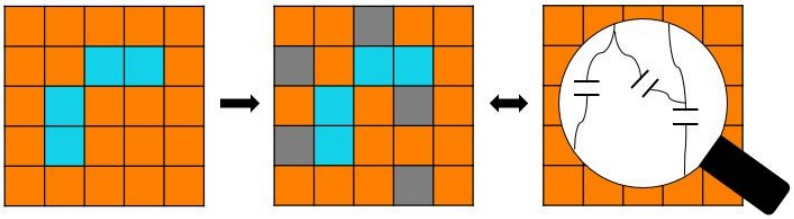

Figure A.1.: Representation of addition of third material (gray) apart from BST (orange) and MBO (blue). This inclusion can be metallic (Ag^+) or conducting oxides (ITO).

This work presents a preliminary solution in this direction, which includes the addition of Ag^+ inclusions in BST bulk material in doping compositions of 1, 2, 5 vol-%. Due to short problems at electric field strengths above 700 V/mm, only 1 vol-% alternative demonstrates an acceptable performance in this regard. However, decreased tunability in Figure A.2 does not illustrate expected increased tunable behavior, and more efforts will be made to make a reliable operation possible.

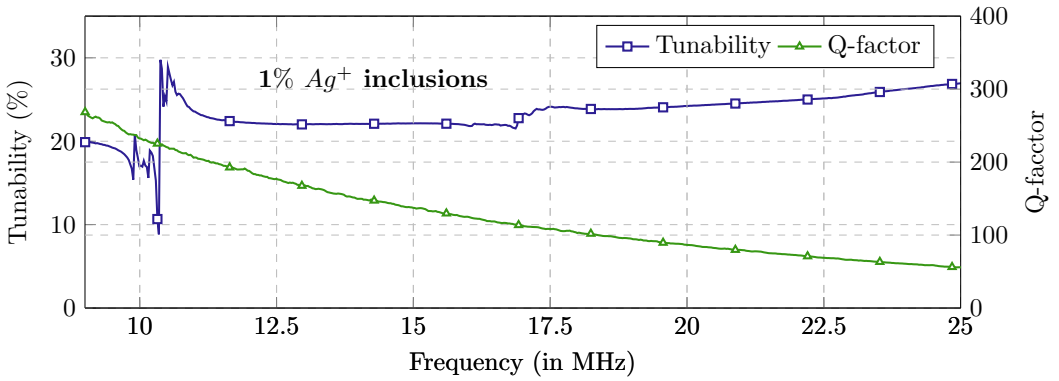

Figure A.2.: Extracted measured parameters for 1 vol-% of Ag^+ inclusion into BST material.

Another attempt in this direction includes the addition of Indium Titanium Oxide (ITO) in the BST-MBO composites. Figure A.3 illustrates the extracted capacitances for various BST-MBO-ITO compositions. However, these exhibits practically negligible tunability. The Curie temperature T_C is less than -30°C and could not be measured due to the limited temperature achieved by the thermal characterization setup. To counter this substantial decrease in T_C, a higher $BaTiO_3$ content BST stoichiometries will be employed to enable a desirable room temperature operation.

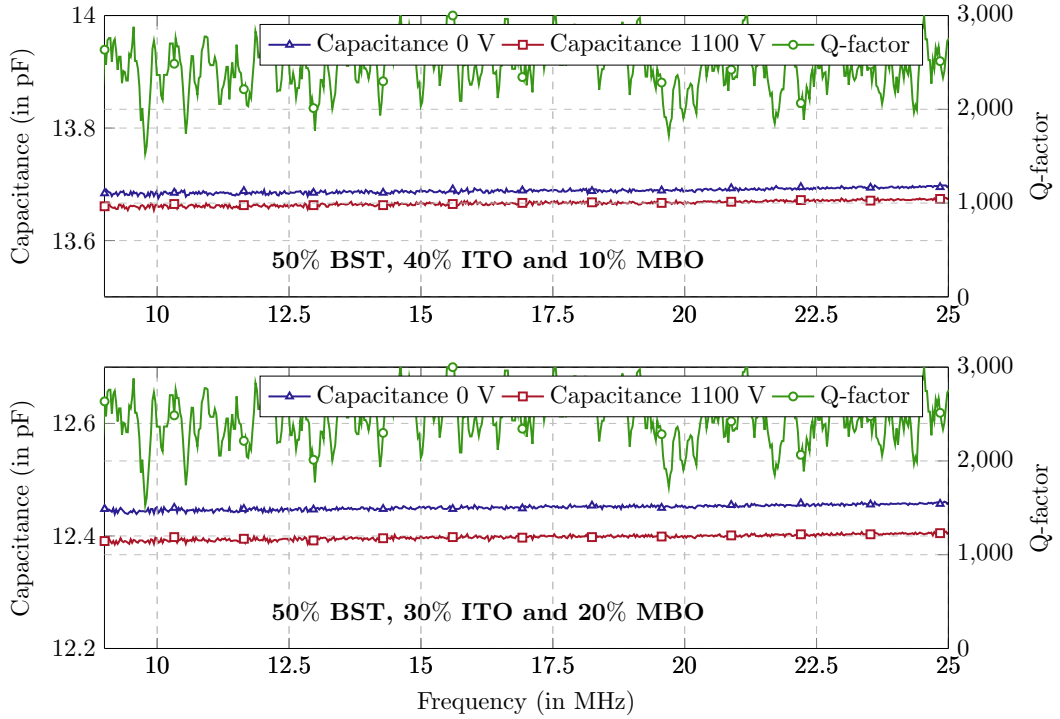

Figure A.3.: Extracted measured parameters for 30 and 40 vol-% of indium titanium oxide (ITO) inclusion into BST-MBO composite material.

B. Symbols and Abbreviations

ε_0	Permittivity of Vacuum
ε_r	Relative Permittivity
f	Frequency
f_r	Resonance frequency
τ_ε	Permittivity Tunability of the material
τ_C	Capacitance Tunability of the material
χ_e	Susceptiblity
$\vec{q}$	Charge
$\vec{p}$, $\vec{P}$, P	Polarization
P_R	Remnant Polarization
P_S	Spontaneous Polarization
Γ	Damping Coefficient
$\vec{D}$	Electric Flux Density
$\vec{E}$, E	Electric Field
Γ	Damping Coefficient
$\tan\delta$	Loss Tangent
η	Material Quality Factor
d, D	Piezoelectric Coefficient
g, G	Electrostrictive Coefficient
T_C	Curie temperature
Q_ε	Q-factor
$c^{(m)}$	Young's Modulus

ν_p	Phase Velocity
n_d	Defect Concentration
σ_R	Rayleigh Parameter

AI	Artificial Intelligence
IOT	Internet of Things
5G	Fifth Generation
RFICs	Radio Frequency Integrated Circuits
BST	Barium Strontium Titanate
MBO	Magnesium Borate
ITO	Indium Titanium Oxide
ADAS	Advanced Driver Assistance Systems
LiDAR	Light Detection And Ranging
EM	Electromagnetic
CCP	Capacitively Coupled Plasma
ICP	Inductively Coupled Plasma
ALE	Atomic Layer Etching
MEMS	MicroElectroMechanical Systems
ICs	Integrated Circuits
RF	Radio Frequency
SAW	Surface Acoustic Wave
BAW	Bulk Acoustic Wave
VNA	Vector Network Analyzer
ESR	Equivalent Series Resistance

Bibliography

[AE18] H. Abomostafa and M. Ellamey. "Studying the mechanical properties of barium strontium titanate ceramics by an ultrasonic pulse echo technique". In: *Journal of Ovonic Research* (2018).

[AGK15] A. Ahmed, I. A. Goldthorpe, and A. K. Khandani. "Electrically tunable materials for microwave applications". In: *Applied Physics Reviews* (2015). DOI: 10.1063/1.4906255.

[AM11] R. Arora and W. Mosch. *High Voltage and Electrical Insulation Engineering*. John Wiley Sons, Inc., 2011. DOI: 10.1002/9780470947906.

[And+11] C. M. Andersson, N. Ejebjork, A. Henry, S. Andersson, E. Janzen, H. Zirath, and N. Rorsman. "A SiC Varactor With Large Effective Tuning Range for Microwave Power Applications". In: *IEEE Electron Device Letters* (2011). DOI: 10.1109/LED.2011.2131117.

[Ann+19] K. Annam, D. Spatz, E. Shin, and G. Subramanyam. "Experimental Verification of Microwave Phase Shifters Using Barium Strontium Titanate (BST) Varactors". In: *2019 IEEE National Aerospace and Electronics Conference (NAECON)*. 2019. DOI: 10.1109/NAECON46414.2019.9058107.

[BA21] D. Burg and J. H. Ausubel. "Moore's Law revisited through Intel chip density". In: *PLOS ONE* (2021). DOI: 10.1371/journal.pone.0256245.

[Ber78] D. J. Bergman. "The dielectric constant of a composite material—A problem in classical physics". In: *Physics Reports* (1978). DOI: 10.1016/0370-1573(78)90009-1.

[Bru35] D. A. G. Bruggeman. "Berechnung verschiedener physikalischer Konstanten von heterogenen Substanzen. I. Dielektrizitätskonstanten und Leitfähigkeiten der Mischkörper aus isotropen Substanzen". In: *Annalen der Physik* (1935). DOI: 10.1002/andp.19354160705.

[Cav20] R. H. Caverly. "PIN Diode Switching Speed for MRI Applications". In: *2020 IEEE MTT-S International Microwave Biomedical Conference (IMBioC)*. 2020. DOI: 10.1109/IMBIoC47321.2020.9385053.

[Cha+19] V. Chauhan, C. Huck, A. Frank, W. Akstaller, R. Weigel, and A. Hagelauer. "Enhancing RF Bulk Acoustic Wave Devices: Multiphysical Modeling and Performance". In: *IEEE Microwave Magazine* (2019). DOI: 10.1109/MMM.2019.2928677.

[Che17] Y. Chen. "Tunable Decoupling and Matching Concepts for Compact Mobile Terminal Antennas". PhD thesis. Gottfried Wilhelm Leibniz Universität Hannover, 2017.

[CLY05] D. R. Chase, C. Lee-Yin, and R. A. York. "Modeling the capacitive nonlinearity in thin-film BST varactors". In: *IEEE Transactions on Microwave Theory and Techniques* (2005). DOI: 10.1109/TMTT.2005.855141.

[Com] The Rubber Company. "Electrically tunable materials for microwave applications". In: *Data Sheet* (). URL: https://therubbercompany.com/wp-content/uploads/2019/11/RC02109-Nitirle-Sponge-Material-Data-Sheet.pdf.

[CZY07] X. Chou, J. Zhai, and X. Yao. "Dielectric tunable properties of low dielectric constant Ba0.5Sr0.5TiO3–Mg2TiO4 microwave composite ceramics". In: *Applied Physics Letters* (2007). DOI: 10.1063/1.2784202.

[Dub99] D. C. Dube. "Dielectric films in the microwave region". In: *Ferroelectrics* (1999). DOI: 10.1080/00150199908009121.

[Gar04] J. C. Maxwell Garnett. "Colours in Metal Glasses and in Metallic Films". In: *Philosophical Transactions of the Royal Society of London Series A* (1904).

[GC17] A. Goodyear and M. Cooke. "Atomic layer etching in close-to-conventional plasma etch tools". In: *Journal of Vacuum Science & Technology A* (2017). DOI: 10.1116/1.4972393.

[Gev09] S. Gevorgian. *Ferroelectrics in Microwave Devices, Circuits and Systems*. SpringerLink, 2009. DOI: 10.1007/978-1-84882-507-9.

[Gha+16] A. Ghalem, L. Huitema, A. Crunteanu, M. Rammal, L. Trupina, L. Nedelcu, M. G. Banciu, P. Dutheil, C. Constantinescu, P. Marchet, F. Dumas-Bouchiat, and C. Champeaux. "Electrical transport properties and modelling of electrostrictive resonance phenomena in Ba2/3Sr1/3TiO3 thin films". In: *Journal of Applied Physics* (2016). DOI: 10.1063/1.4966942.

[Gie+08] A. Giere, R. Schafranek, Y. Zheng, H. Maune, M. Sazegar, R. Jakoby, and A. Klein. "Characterization of Acoustic Effects in Ferroelectric Thin-Films for Microwave Components". In: *Frequenz* (2008). DOI: 10.1515/FREQ.2008.62.3-4.52.

[Gie09] A. Giere. "Passiv steuerbare Mikrowellenphasenschieber auf der Basis nichtlinearer Dielektrika". PhD thesis. Technical University of Darmstadt, 2009.

[GVL06] S. Gevorgian, A. Vorobiev, and T. Lewin. "dc field and temperature dependent acoustic resonances in parallel-plate capacitors based on SrTiO3 and Ba0.25Sr0.75TiO3 films: Experiment and modeling". In: *Journal of Applied Physics* (2006). DOI: 10.1063/1.2209727.

[HC60] B.W. Hakki and P.D. Coleman. "A Dielectric Resonator Method of Measuring Inductive Capacities in the Millimeter Range". In: *IRE Transactions on Microwave Theory and Techniques* (1960). DOI: 10.1109/TMTT.1960.1124749.

[HJB10] J. Ho, T. R. Jow, and S. Boggs. "Historical introduction to capacitor technology". In: *IEEE Electrical Insulation Magazine* (2010). DOI: 10.1109/mei.2010.5383924.

[Hua+15] Y. H. Huang, Y. J. Wu, W. J. Qiu, J. Li, and X. M. Chen. "Enhanced energy storage density of Ba0.4Sr0.6TiO3–MgO composite prepared by spark plasma sintering". In: *Journal of the European Ceramic Society* (2015). DOI: https://doi.org/10.1016/j.jeurceramsoc.2014.11.022.

[Jaf58] H. Jaffe. "Piezoelectric Ceramics". In: *Journal of the American Ceramic Society* (1958). DOI: 10.1111/j.1151-2916.1958.tb12903.x.

[Jeo04] J.-H. Jeon. "Effect of SrTiO3 concentration and sintering temperature on microstructure and dielectric constant of Ba1-xSrxTiO3". In: *Journal of the European Ceramic Society* (2004). DOI: 10.1016/S0955-2219(03)00385-6.

[JS04] A. F. Júnior and D. J. Shanafield. "Thermal conductivity of polycrystalline aluminum nitride (AlN) ceramics". In: *Cerâmica* (2004). DOI: 10.1590/s0366-69132004000300012.

[JS08a] J. W. Jewett and R. A. Serway. *Physics for Scientists and Engineers with Modern Physics*. thomson brooks/cole, 2008.

[JS08b] L. Jylha and A. Sihvola. "Tunability of Granular Ferroelectric Dielectric Composites". In: *Progress In Electromagnetic Research* (2008). DOI: 10.2528/PIER07081502.

[Jyl08] L. Jylha. "Modeling of electrical properties of composites". PhD thesis. Aalto University, 2008.

[Kan+15] K. J. Kanarik, T. Lill, E. A. Hudson, S. Sriraman, S. Tan, Jeffrey Marks, Vahid Vahedi, and Richard A. Gottscho. "Overview of atomic layer etching in the semiconductor industry". In: *Journal of Vacuum Science & Technology A* (2015). DOI: 10.1116/1.4913379.

[Kie+17] D. Kienemund, T. Fink, M. Abrecht, W. Bigler, J. R. Binder, R. Jakoby, and H. Maune. "A fully-printed, BST MIM varactor for low ISM-band matching networks up to 1000 W". In: *2017 47th European Microwave Conference (EuMC)*. 2017. DOI: 10.23919/EuMC.2017.8231015.

[Kie+18a] D. Kienemund, N. Bohn, T. Fink, M. Abrecht, W. Bigler, J. R. Binder, R. Jakoby, and H. Maune. "Acoustical Behavior of Fully-Printed, BST MIM Varactor Modules in High Power Matching Circuits". In: *2018 IEEE/MTT-S International Microwave Symposium - IMS*. 2018. DOI: 10.1109/MWSYM.2018.8439171.

[Kie+18b] D. Kienemund, D. Walk, N. Bohn, J. R. Binder, R. Jakoby, and H. Maune. "Proceedings of the 48th European Microwave Conference Suppression of Acoustic Resonances in Fully-Printed, BST Thick Film Varactors Utilizing Double MIM Structures". In: *2018 48th European Microwave Conference (EuMC)*. 2018. DOI: 10.23919/EuMC.2018.8541497.

[Kie19] D. M. Kienemund. "High-Power Varactors for Fast Adaptive Impedance Matching at 13.56 MHz". PhD thesis. Technical University of Darmstadt, 2019.

[Kim+13] S.W. Kim, H.I. Choi, M.H. Lee, J.S. Park, D.J. Kim, T.K. Song D. Do M.H. Kim, and W.J. Kim. "Electrical properties and phase of BaTiO3–SrTiO3 solid solution". In: *Ceramics International* (2013). DOI: 10.1016/j.ceramint.2012.10.119.

[Koh+13] C. Kohler, A. Friederich, M. Sazegar, M. Nikfalazar, F. Stemme, D. Wang, C. Kuebel, R. Jakoby, and J. R. Binder. "Effects of ZnO-B2O3 Addition on the Microstructure and Microwave Properties of Low-Temperature Sintered Barium Strontium Titanate (BST) Thick Films". In: *International Journal of Applied Ceramic Technology* (2013). DOI: 10.1111/ijac.12116.

[Koh+15] C. Kohler, M. Nikfalazar, A. Friederich, A. Wiens, M. Sazegar, R. Jakoby, and J. R. Binder. "Fully Screen-Printed Tunable Microwave Components Based on Optimized Barium Strontium Titanate Thick Films". In: *International Journal of Applied Ceramic Technology* (2015). DOI: 10.1111/ijac.12276.

[Koz+95] A.B. Kozyrev, V.N. Keis, G. Koepf, R. Yandrofski, O.I. Soldatenkov, K.A. Dudin, and D.P. Dovgan. "Procedure of microwave investigations of ferroelectric films and tunable microwave devices based on ferroelectric films". In: *Microelectronic Engineering* (1995). DOI: 10.1016/0167-9317(95)00156-5.

[KP59] W. Kwestroo and H. A. M. Paping. "The Systems BaO-SrO-TiO2, BaOCaO-TiO2, and SrO-CaO-TiO2". In: *Journal of the American Ceramic Society* (1959). DOI: 10.1111/j.1151-2916.1959.tb12957.x.

[KSK98] S. H. Kim, H. W. Seon, and Y. Kim. "Effect of MnO on the Electrical Properties of Nb-Doped SrTiO3 Varistor". In: *MRS Proceedings* (1998). DOI: 10.1557/PROC-547-121.

[KTG18] K. J. Kanarik, S. Tan, and R. A. Gottscho. "Atomic Layer Etching: Rethinking the Art of Etch". In: *The Journal of Physical Chemistry Letters* (2018). DOI: 10.1021/acs.jpclett.8b00997.

[Lau+05] V. Laur, A. Rousseau, G. Tanne, P. Laurent, F. Huret, M. Guilloux-Viry, and B. Della. "Tunable microwave components based on KTaxNb1-xO3 ferroelectric material". In: *Proceedings European Microwave Conference* (2005). DOI: 10.1109/EUMC.2005.1608938.

[Lei15] M. Lei. "The Impact of Composite Effect on Dielectric Constant and Tunability in Ferroelectric–Dielectric System". In: *Journal of the American Ceramic Society* (2015). DOI: 10.1111/jace.13768.

[Li+14] F. Li, L. Jin, Z. Xu, and S. Zhang. "Electrostrictive effect in ferroelectrics: An alternative approach to improve piezoelectricity". In: *Applied Physics Reviews* (2014). DOI: 10.1063/1.4861260.

[Li+19] W. Li, D. Zhou, R. Xu, D. Wang, J. Su, L. Pang, W. Liu, and G. Chen. "BaTiO3-Based Multilayers with Outstanding Energy Storage Performance for High Temperature Capacitor Applications". In: *ACS Applied Energy Materials* (2019). DOI: 10.1021/acsaem.9b00664.

[LL05] M. A. Lieberman and A. J. Lichtenberg. *Principles of Plasma Discharges and Materials Processing, 2nd Edition*. John Wiley Sons, 2005.

[LLC14] CalRamic Technologies LLC. *The effect of temperature and voltage changes on high voltage ceramic capacitors.* Technical report. CalRamic Technologies LLC, 2014.

[LLP22] Mordor Intelligence LLP. "Global Semiconductor Device Market - Growth, Trends, COVID-19 Impact, and Forecasts (2022 - 2027)". In: *ReportLinker* (2022). URL: https://www.reportlinker.com/p06321515/?utm_source=GNW.

[Mar13] J. Martinez-Vega. *Dielectric Materials for Electrical Engineering*. Wiley, 2013.

[Mau+10] Holger Maune, Mohsen Sazegar, Yuliang Zheng, Andre Giere, and Rolf Jakoby. "Design of planar varactors based on ferroelectric thick-films". In: *German Microwave Conference Digest of Papers*. 2010.

[Mau11] H. Maune. "Design und Optimierung hochlinearer ferroelektrischer Varaktoren für steuerbare Hochfrequenz-Leistungsverstärker". PhD thesis. Technical University of Darmstadt, 2011.

[Men+11] W. Menesklou, F. Paul, X. Zhou, H. Elsenheimer, J. R. Binder, and E. Ivers-Tiffée. "Nonlinear ceramics for tunable microwave devices part I: materials properties and processing". In: *Microsystem Technologies* (2011). DOI: 10.1007/s00542-011-1277-z.

[Mer+17] D. Mercier, A. Niembro-Martin, H. Sibuet, C. Baret, J. Chautagnat, C. Dieppedale, C. Bonnard, J. Guillaume, G. Le Rhun, C. Billard, P. Gardes, and P. Poveda. "X band distributed phase shifter based on Sol-Gel BCTZ varactors". In: *2017 European Radar Conference (EURAD)*. 2017. DOI: 10.23919/EURAD.2017.8249227.

[Nad+15] K. Nadaud, C. Borderon, R. Renoud, and H. W. Gundel. "Effect of manganese doping of BaSrTiO3 on diffusion and domain wall pinning". In: *Journal of Applied Physics* (2015). DOI: 10.1063/1.4913694.

[New05] R. E. Newnham. *Properties of Materials: Anisotropy, Symmetry, Structure*. Oxford University Press, 2005.

[NSS17] Z. Nazarchuk, V. Skalskyi, and O. Serhiyenko. *Acoustic Emission, Methodology and Application*. Springer, 2017.

[Pan08] Panasonic. *Dry Etching System - Panasonic Dry Etching Device Suited for The Next Generation Bonding of 3D Lamination, MEMS, High Aspect and Micro Fabrication, and Device Processing of Difficult Etching Materials*. Technical report. Panasonic, 2008.

[Pau06] F. Paul. "Dotierte Ba0,6Sr0,4TiO3 -Dickschichten als steuerbare Dielektrika". PhD thesis. Albert-Ludwigs-Universität Freiburg im Breisgau, 2006.

[Poz04] D.M. Pozar. *Microwave Engineering*. Wiley, 2004.

[SB01] B. Su and T. W. Button. "Interactions between barium strontium titanate (BST) thick films and alumina substrates". In: *Journal of the European Ceramic Society* (2001). DOI: 10.1016/s0955-2219(01)00362-4.

[SB04] B. Su and T. W. Button. "Microstructure and dielectric properties of Mg-doped barium strontium titanate ceramics". In: *Journal of Applied Physics* (2004). DOI: 10.1063/1.1636263.

[Sch07] M. Schmidt. "Abstimmbare Anpassnetzwerke auf Basis ferroelektrischer Varaktoren für Mobilfunkanwendungen". PhD thesis. Friedrich-Alexander-Universität Erlangen-Nürnberg, 2007.

[SFW63] M. Sucher, J. Fox, and M. Wind. *Handbook of microwave measurements (3rd Edition)*. Interscience Publishers, 1963.

[She+06] V. O. Sherman, A. K. Tagantsev, N. Setter, D. Iddles, and T. Price. "Ferroelectric-dielectric tunable composites". In: *Journal of Applied Physics* (2006). DOI: 10.1063/1.2186004.

[She+20] S. Shen, L. Xin, L. Ren, W. Wang, J. Jin, J. Zhai, and M. Zhang. "Effects of non-stoichiometric defects on the dielectric properties of (Ba0.5Sr0.5)xTiO3-ZnGa2O4 composite ceramics". In: *Ceramics International* (2020). DOI: 10.1016/j.ceramint.2020.05.321.

[Sla07] P. G. Slade. *High Voltage and Electrical Insulation Engineering*. CRC Press, 2007.

[SN66] J. C. Sethares and S. J. Naumann. "Design of Microwave Dielectric Resonators". In: *IEEE Transactions on Microwave Theory and Techniques* (1966). DOI: 10.1109/TMTT.1966.1126144.

[Sta+18] A. Stanoiu, R. M. Piticescu, C. E. Simion, C. F. Rusti-Ciobota, O. G. Florea, V. S. Teodorescu, P. Osiceanu, A. Sobetkii, and V. Badilita. "H2S selective sensitivity of Cu doped BaSrTiO3 under operando conditions and the associated sensing mechanism". In: *Sensors and Actuators B: Chemical* (2018). DOI: https://doi.org/10.1016/j.snb.2018.03.013.

[Su03] B. Su. "Dielectric and microwave properties of barium strontium titanate (BST) thick films on alumina substrates". In: *Journal of the European Ceramic Society* (2003). DOI: 10.1016/s0955-2219(03)00171-7.

[Sza+21] B. Szafraniak, L. Fusnik, J. Xu, F. Gao, A. Brudnik, and A. Rydosz. "Semiconducting Metal Oxides: SrTiO3, BaTiO3 and BaSrTiO3 in Gas-Sensing Applications". In: *Coatings* (2021). DOI: 10.3390/coatings11020185.

[Tag+03] A. K. Tagantsev, V. O. Sherman, K. F. Astafiev, J. Venkatesh, and N. Setter. "Ferroelectric materials for microwave tunable applications". In: *Journal of Electroceramics* (2003). DOI: 10.1023/B:JECR.0000015661.81386.e6.

[Tag05] A. K. Tagantsev. "Susceptibility anomaly in films with bilinear coupling between order parameter and strain". In: *Physical Review Letters* (2005). DOI: 10.1103/PhysRevLett.94.247603.

[Tan+14] L. Tang, Y. Bian, J. Zhai, and H. Zhang. "Ferroelectric–Dielectric Composites Model of Ba0.5Sr0.5TiO3/Mg2AO4(A = Ti, Si) for Tunable Application". In: *Journal of the American Ceramic Society* (2014). DOI: 10.1111/jace.12718.

[Tic+08] T. Tick, J. Peräntie, H. Jantunen, and A. Uusimäki. "Screen printed low-sintering-temperature barium strontium titanate (BST) thick films". In: *Journal of the European Ceramic Society* (2008). DOI: 10.1016/j.jeurceramsoc.2007.08.008.

[TM12] P. A. Tipler and G. Mosca. *Physik für Wissenschaftler und Ingenieure*. Spektrum Akademischer Verlag, Heidelberg, 2012.

[Ven+08] I. B. Vendik, P. Turalchuk, O. G. Vendik, and J. Berge. "Modeling Tunable Bulk Acoustic Resonators Based on Induced Piezoelectric Effect in BaTiO3 and Ba0.25Sr0.75TiO3 Films". In: *Journal of Applied Physics* (2008). DOI: 10.1063/1.2830866.

[Vis15] Vishay. *Ceramic Disk, RFI and Safety Capacitors*. Technical report. Vishay, 2015.

[VTZ98] O. G. Vendik, L. T. Ter-Martirosyan, and S. P. Zubko. "Microwave losses in incipient ferroelectrics as functions of the temperature and the biasing field". In: *Journal of Applied Physics* (1998). DOI: 10.1063/1.368166.

[VVK00] I.B. Vendik, O.G. Vendik, and E.L. Kollberg. "Commutation quality factor of two-state switchable devices". In: *IEEE Transactions on Microwave Theory and Techniques* (2000). DOI: 10.1109/22.841874.

[Wal21] D. Walk. "All-Oxide Thin-Film Varactors: RF Characterization - Modeling - Integration." PhD thesis. Technical University of Darmstadt, 2021.

[Wan+15] X. Wang, F. Xia, N. Li, J. Wang, C. Li, X. Zhang, Y. Bian, G. Li, Y. Wu, H. Li, L. Sun, and Y. He. "A YBCO/BST/MgO interdigital varactor and an L-band tunable HTS bandpass filter". In: *2015 IEEE MTT-S International Microwave Workshop Series on Advanced Materials and Processes for RF and THz Applications (IMWS-AMP)*. 2015. DOI: 10.1109/IMWS-AMP.2015.7324962.

[WBT04] R. Waser, U. Böttger, and S. Tiedke. *Polar Oxides*. Wiley, 2004. DOI: 10.1002/3527604650.

[Wei03] C. Weil. "Passiv steuerbare Mikrowellenphasenschieber auf der Basis nichtlinearer Dielektrika". PhD thesis. Technical University of Darmstadt, 2003.

[Wie+17] A. Wiens, C. Kohler, M. Hansli, M. Schuessler, M. Jost, H. Maune, J. R. Binder, and R. Jakoby. "CAD-assisted modeling of high dielectric contrast composite materials". In: *Journal of the European Ceramic Society* (2017). DOI: 10.1016/j.jeurceramsoc.2016.10.032.

[Zen+12] Y. Zeng, C. Gao, G. Zhang, and S. Jiang. "Effects of B2O3-Li2O additions on the dielectric properties of screen printing Ba0.6Sr0.4TiO3 thick films". In: *physica status solidi (a)* (2012). DOI: 10.1002/pssa.201127276.

[Zha+09] M. Zhang, H. Wang, F. Xiang, and X. Yao. "Low-Temperature Sintering (Ba0.6Sr0.4)TiO3Thick Film Prepared by Screen Printing". In: *: International Journal of Applied Ceramic Technology* (2009). DOI: 10.1111/j.1744-7402.2008.02265.x.

[Zha+10] Qingmeng Zhang, Lei Wang, Jun Luo, Qun Tang, and Jun Du. "Ba0.4Sr0.6TiO3/MgO Composites with Enhanced Energy Storage Density and Low Dielectric Loss for Solid-State Pulse-Forming Line". In: *International Journal of Applied Ceramic Technology* (2010). DOI: 10.1111/j.1744-7402.2009.02456.x.

[Zho+12] X. Zhou, M. Sazegar, F. Stemme, J. Haußelt, R. Jakoby, and J.R. Binder. "Correlation of the microstructure and microwave properties of Ba0.6Sr0.4TiO3 thick-films". In: *Journal of the European Ceramic Society* (2012). DOI: 10.1016/j.jeurceramsoc.2012.06.021.

[Zho12] X. Zhou. "Prozess- und Dotierungseinflüsse auf Ba0,6Sr0,4TiO3-Dickschichten für steuerbare Mikrowellenkomponenten". PhD thesis. Technical University of Darmstadt, 2012.

[ZZY11] Q. Zhang, J. Zhai, and X. Yao. "Dielectric and Percolative Properties of Ba0.5Sr0.5TiO3–Mg3B2O6 Composite Ceramics". In: *Journal of the American Ceramic Society* (2011). DOI: 10.1111/j.1551-2916.2010.04165.x.

Own Publications

[Agr+21] P. Agrawal, D. Kienemund, D. Walk, S. Matic, N. Bohn, K. Häuser, T. Fink, M. Abrecht, W. Bigler, J. R. Binder, R. Jakoby, and H. Maune. "Suppression of Acoustic Resonances in BST-Based Bulk-Ceramic Varactors by Addition of Magnesium Borate". In: *Crystals* (2021). DOI: 10.3390/cryst11070786.

[Agr+23] P. Agrawal, S. Matic, K. Häuser, J. R. Binder, H. Maune, E. Polat, and R. Jakoby. "Electromagnetic modeling of tunability of Barium Strontium Titanate and Magnesium Borate composites". In: *Ceramics International* (2023). DOI: 10.1016/j.ceramint.2022.09.202.

Co-author Publications

[Häu+20a] K. B. Häuser, P. Agrawal, J. R. Binder, and R. Jakoby. "(ICACC-S8-023-2020) NDK and HDK composite networks for optimization of dielectric behavior". In: *44th International Conference Exposition on Advanced Ceramics Composites*. 2020. URL: https://ceramics.org/event/44th-international-conference-and-expo-on-advanced-ceramics-and-composites-icacc-2020-archive.

[Häu+20b] K. B. Häuser, P. Agrawal, J. R. Binder, and R. Jakoby. "NDK and HDK composite networks for optimization of dielectric behavior." In: *Electroceramics XVII*. 2020.

[Häu+21] K. Häuser, R. Azmi, P. Agrawal, R. Jakoby, H. Maune, M.J. Hoffmann, and J.R. Binder. "Sintering behavior and electrical properties of the paraelectric/dielectric composite system BST/MBO". In: *Journal of the European Ceramic Society* (2021). DOI: 10.1016/j.jeurceramsoc.2021.07.008.

[Häu+23] K. Häuser, Z. Zhou, P. Agrawal, R. Jakoby, H. Maune, and J.R. Binder. "Network-Structured BST/MBO Composites Made from Core-Shell-Structured Granulates". In: *Materials* (2023). DOI: 10.3390/ma16020710. URL: https://www.mdpi.com/1996-1944/16/2/710.

[Nic+20] M. Nickel, A. Jiménez-Sáez, P. Agrawal, A. Gadallah, A. Malignaggi, C. Schuster, R. Reese, H. Tesmer, E. Polat, D. Wang, P. Schumacher, R. Jakoby, D. Kissinger, and H. Maune. "Ridge Gap Waveguide Based Liquid Crystal Phase Shifter". In: *IEEE Access* (2020). DOI: 10.1109/ACCESS.2020.2989547.

[Wal+20] D. Walk, D. Kienemund, P. Agrawal, P. Salg, L. Zeinar, P. Komissinskiy, L. Alff, R. Jakoby, and H. Maune. "Suppression of Acoustic Resonances in All-Oxide Varactors". In: *2020 IEEE/MTT-S International Microwave Symposium (IMS)*. 2020. DOI: 10.1109/IMS30576.2020.9224035.

[Wal+21] D. Walk, P. Agrawal, L. Zeinar, P. Salg, A. Arzumanov, P. Komissinskiy, L. Alff, R. Jakoby, S.J. Rupitsch, and H. Maune. "All-Oxide Varactor Electromechanical Properties Extracted by Highly Accurate Modeling Over a Broad Frequency and Electric Bias Range". In: *IEEE Transactions on Ultrasonics, Ferroelectrics, and Frequency Control* (2021). DOI: 10.1109/TUFFC.2021.3070749.

Patent Contribution

[Bin+21] J. R. Binder, H. Maune, K. Häuser, R. Jakoby, and P. Agrawal. “Superkomposie - Strukturierte keramische Komposite zur Verbesserung der dielektrischen Eigenschaften”. In: *Deutsche Patent DE 10 2021 069 990.8* (2021).

Supervised Student Theses

- **Dakyung Lee:** *Capacitance Modeling of Ternary Composites with BST added with MBO and metallic inclusions* , Project Seminar, September 2019
- **Zeyu Xiang:** *Single Layer Reconfigurable Antenna based on Thick-Film BST Technology*, Master Thesis, July 2021

Curriculum Vitae

Personal Details

Name:	Prannoy Agrawal
Date of birth:	07. Januar 1991
Place of birth:	New Delhi, India

Education

Since 2018	Technical University of Darmstadt Research Associate at the Institute of Microwave Engineering and Photonics
2015 – 2018	Technical University of Darmstadt Master of Science
2008 – 2012	Guru Gobind Singh Indraprastha University Bachelor of Technology

Employment

2012 – 2015	Infosys Pvt. Ltd. Senior System Engineer